

Syracuse University

**SURFACE**

---

Dissertations - ALL

SURFACE

---

6-1-2015

## Investigating the unique occurrence of polytypism and the role of available shell precursors in the growth of giant shell quantum dots

Somak Majumder  
*Syracuse University*

Follow this and additional works at: <https://surface.syr.edu/etd>



Part of the [Physical Sciences and Mathematics Commons](#)

---

### Recommended Citation

Majumder, Somak, "Investigating the unique occurrence of polytypism and the role of available shell precursors in the growth of giant shell quantum dots" (2015). *Dissertations - ALL*. 257.  
<https://surface.syr.edu/etd/257>

This Dissertation is brought to you for free and open access by the SURFACE at SURFACE. It has been accepted for inclusion in Dissertations - ALL by an authorized administrator of SURFACE. For more information, please contact [surface@syr.edu](mailto:surface@syr.edu).

## Abstract

Researchers have epitaxially grown thick inorganic shells on the surface of quantum dots (QDs) cores to improve quantum yields, increase photostability and suppress fluorescence intermittency (blinking) in ‘giant quantum dots’ (gQDs). These unique properties make gQDs excellent candidates for applications in lasers, single molecular probes and solid state LEDs. Although a growing wealth of knowledge exists for the photophysical properties of the gQDs, limited research has been directed towards understanding the synthetic intricacies and crystal growth. In this dissertation work I present a detailed study of the growth of CdSe/CdZnS multishell gQDs and focus on crystallographic and morphological evolution. I studied the effect of core crystal structure and shell growth was performed on crystallographically disparate (*W*, wurtzite and *ZB*, zinc blende) CdSe cores under identical synthetic conditions. My work revealed that while shell growth transitioned to *W* type growth in both cases, occurrence of unique *W-ZB* mixed crystallinity (polytypism) was significant and might result in the final gQDs as a consequence of the ligands and reaction conditions involved in the traditional synthesis. Next, I investigated the influence of the shell anion precursor concentrations on gQD growth employing identical *W* cores, by altering the mode of addition and three different sources of sulfur. Experimental results indicated that delicate interplay of crystal structure preference and ligands involved in the synthesis resulted in varied morphologies (rod, tripodal, trigonal and polyhedral) and crystal structures (*W*, *ZB*, *W-ZB* and *ZB* respectively) of gQDs in each of the syntheses.



**Investigating the unique occurrence of polytypism and the  
role of available shell precursors in the growth of giant shell  
quantum dots**

By  
Somak Majumder  
Department of Chemistry

**Dissertation**

Submitted in partial fulfillment of the requirements for the  
Degree of Doctor of Philosophy in Chemistry  
in the Graduate School of Syracuse University

Syracuse University  
June 2015

Copyright 2015 Somak Majumder

All Rights Reserved

## **Acknowledgements**

Foremost, I would like to express my sincere gratitude to my advisor Professor Mathew Maye for his patience, motivation, enthusiasm and support throughout my graduate school career. His guidance helped me at every step of my PhD research and writing of this thesis. I could not have imagined having a better advisor and mentor for my PhD study.

Besides my advisor, I would like to thank the members of my PhD committee: Prof. Shikha Nangia, Prof. Yan-Yeung Luk, Prof. Robert P. Doyle, Prof. Arindam Chakraborty and Prof. Michael B. Sponsler, for their support, encouragement and insightful comments during the process of dissertation and defense. Special thanks to Prof. Jon Zubieta for his guidance during my time at Syracuse University.

I would like to express my sincerest thanks to Dr. Tennyson Doane for the insightful discussions and help during my research and thesis writing. I thank my fellow lab mates Davon, Patrick, Kaitlin Alisha, Lili, Kaitlin, Laxmikant and Jay, for their support and help throughout the last five years and for making the lab experience an enjoyable one.

I would like to thank the love of my life and wife Amrita, for bearing with me during the journey. Without her love, enthusiasm and help during thesis writing this work would not have been possible.

I would like to thank my family: my parents and my younger sister Mohor, without whose constant love, encouragement and support I would not have been able to steer through the difficult times of my life or be the person I am today.

I thank my friends and colleagues at Syracuse University, for making the Syracuse chapter of my life a memorable one. Specifically I would like to thank Flaviiyan Jerome, Abhinanden Sambasivam, Raghuvaran Iyer, and Arijit Adhikari for their help and support.

Lastly, I would like to thank God, for everything I have or yet to come in my life.

## Table of Contents

<b>List of Figures</b>	viii
<b>List of Tables</b>	xv
<b>List of Abbreviations</b>	xvi

### Chapter 1 - Introduction

1.1 Quantum dots	1
1.1.1 Definition, history and applications	1
1.1.2 Quantum confinement effect and optoelectronic properties	2
1.1.3 Crystal structure of quantum dots	6
1.1.4 Synthesis of quantum dots	7
1.1.4.1 Background	7
1.1.4.2 Hot injection/Thermal decomposition method	8
1.1.4.3 Core- shell quantum dots	11
1.1.4.3.1 Seeded growth	12
1.1.4.3.2 SILAR (Successive Ion layer adsorption reaction)	13
1.1.4.3.3 Types of core shell systems	15
1.1.4.3.4 Core/shell/shell and graded alloy shell QDs	16
1.1.4.3.5 Blinking in QDs	16
1.1.4.3.6 Giant Quantum Dots (gQDs)	18

1.1.5	QD shapes	19
1.1.5.1	Crystal structure	20
1.1.5.2	Effect of ligands	21
1.1.5.3	Kinetic and thermodynamic effects	22
1.1.6	Polytypism in QDs	23
1.1.7	Research consideration	24
1.1.8	References	25
 <b>Chapter 2 - Investigating the Role of Polytypism in the Growth of Multi-Shell CdSe/CdZnS Quantum Dots</b>		
2.1	Introduction	36
2.2	Experimental	38
2.2.1	Chemicals & Materials	38
2.2.2	Synthesis	39
2.2.2.1	Synthesis of <i>Zinc blende (ZB)</i> Cores	39
2.2.2.2	Synthesis of <i>Wurtzite (W)</i> CdSe Cores	39
2.2.2.3	Synthesis of Multishelled Giant Quantum Dots (gQD)	40
2.2.2.4	Control experiments	41
2.3	Instrumentation	42
2.4	Calculations	43
2.5	Results & Discussion	44
2.6	Conclusion	62
2.7	References	63
 <b>Chapter 3 - Investigating the role of mode of addition and source of ‘S’ shell</b>		

## **precursors during growth of CdSe/CdZnS giant quantum dots**

3.1 Introduction	69
3.2 Experimental	70
3.2.1 Chemicals & Materials	70
3.2.2 Synthesis	71
3.2.2.1 Synthesis of Wurtzite (W) CdSe Cores	71
3.2.2.2 Synthesis of Multishelled Giant Quantum Dots (gQDs)	72
3.2.2.2.1 Synthesis of SILAR process gQDs	72
3.2.2.2.2 Synthesis of Seeded growth gQDs	73
3.2.2.2.3 Control experiments employing Se=TOP as the shell precursor	76
3.3 Instrumentation	76
3.4 Calculations	78
3.4.1 Concentration of QDs	78
3.4.2 Quantum yield (QY) calculations	78
3.4.3 Strain calculations along <110> for SILAR gQDs	79
3.5 Results	80
3.6 Discussion	99
3.7 Conclusion	103
3.8 References	104
<b>Chapter 4 - Conclusions and outlook</b>	<b>110</b>
<b>Curriculum Vitae</b>	<b>113</b>

## List of Figures

- Figure 1.1:** Schematic representation illustrating the quantum size effect in CdSe QDs.
- Figure 1.2:** Jablonski diagram: schematic representation of the involved absorption and emission processes amongst the exciton states of QD.
- Figure 1.3:** Illustration showing idealized density of electronic states diagram for bulk material (3D), quantum wells (2D), quantum wires and rods (1-D) and QDs (0D).
- Figure 1.4:** Ball and stick model of CdSe ZB unit cell (a), CdSe W unit cell (b) and rock salt unit cell for CdSe (c). Cd atoms denoted by copper colored balls and Se denoted by white balls.
- Figure 1.5:** Schematic showing CdSe core synthesis by hot injection synthesis. TOPO and octadecylphosphonate ligands constitute the capping layer of the synthesized cores.
- Figure 1.6:** Schematic showing seeded growth employed to grow CdS shell on CdSe cores.
- Figure 1.7:** Schematic showing layer by layer SILAR process employed to grow ZnS shell on CdSe cores.
- Figure 1.8:** Scheme showing the three limiting charge carrier localization regime in core/shell QDs.
- Figure 1.9:** Schematic showing a typical synthesis of CdSe/CdZnS gQD. Dioctylamine and oleate ligands are shown as the capping agents.
- Figure 1.10:** (a) A typical *W*-CdSe unit cell, with lattice parameters  $a$ ,  $c$  and differing number of dangling bonds along  $\langle 002 \rangle$  axis shown, (b) A pictorial

representation of the 3D structure of a typical *W* CdSe crystal with the facets, as observed in HRTEM.  $\langle 00\bar{1} \rangle$  and  $\langle 001 \rangle$  are the polar facets, which exhibits higher reactivity than nonpolar  $\langle 100 \rangle$ ,  $\langle 110 \rangle$  and  $\langle 10\bar{1} \rangle$  facets. Adapted from Ref 102.

**Figure 1.11:** Showing the interfacial coherence of  $\langle 002 \rangle$  facet of CdS arms and  $\langle 111 \rangle$  facet of CdSe core in CdSe/ CdS tetrapods, Adapted with permission from Ref.45

**Figure 2.1:** Representative UV-vis absorption (a) and the normalized PL emission spectra (b) for QD cores with Zinc Blende (*ZB*) (i) and Wurtzite (*W*) (ii) crystallinity.

**Figure 2.2:** Representative XRD spectra for *ZB*- (i) and *W*-QD (ii) cores. The CdSe *ZB* and *W* standards are shown as reference. XRD offset vertically for clarity.

**Figure 2.3:** UV-vis (a) and PL emission (b) results characterizing the gQD growth at *ZB*-core at  $n = 0$  (i) 4 (ii), 8 (iii), 12 (iv) and 18 (v). PL excitation carried out at 400 nm.

**Figure 2.4:** Representative TEM micrographs and size distribution of the *ZB*-core ( $d = 3.8 \pm 0.4$  nm) (a), and gQD at shell growth layers of  $n = 4$  ( $d = 10.9 \pm 1.6$  nm) (b), 8 ( $d = 13 \pm 1.9$  nm) (c), 12 ( $d = 17.7 \pm 4.9$  nm) (d) and 18 ( $d = 25.7 \pm 5.3$  nm).

**Figure 2.5:** (a) Plot of TEM determined diameter of gQDs starting from *ZB* (ii) and *W* (i) core with the shell layers ( $n$ ). (b) Position of  $\langle 110 \rangle$  reflection with increasing  $n$  using *ZB* (ii) and *W* (i) cores.

**Figure 2.6:** HRTEM micrographs (a-d) of the gQD products at  $n = 18$  using *ZB*-cores.



Inserted arrows highlight crystalline protrusions.

**Figure 2.7:** Additional HRTEM micrographs (a-b) of the gQD products at  $n = 18$  using ZB-cores. Inserted arrows highlight crystalline protrusions.

**Figure 2.8:** The powder XRD results for shell growth at ZB-cores at shell layers ( $n$ ) of 4 (i), 8 (ii), 12 (iii), and 18 (iv). The CdS ( $W$ , ZB) and ZnS ( $W$ , ZB) standards are provided for reference. XRD offset vertically for clarity.

**Figure 2.9:** Representative UV-vis (a) and PL emission (b) results characterizing the gQD growth at  $W$ -core at  $n = 0$  (i) 4 (ii), 8 (iii), 12 (iv) and 18 (v). PL excitation carried out at 400 nm.

**Figure 2.10:** Representative TEM micrographs and size distribution of the  $W$ -core ( $d = 4.4 \pm 0.9$  nm) (a), and gQD at shell growth layers of  $n = 4$  ( $d = 8.6 \pm 1.2$  nm) (b), 8 ( $d = 11.3 \pm 1.4$  nm) (c), 12 ( $d = 11.8 \pm 1.8$  nm) (d) and 18 ( $d = 13.1 \pm 2.5$  nm) (e).

**Figure 2.11:** HRTEM micrographs (a-d) of the gQD products at  $n = 18$  using  $W$ -cores. Inserted arrows highlight crystalline protrusions.

**Figure 2.12:** Additional HRTEM micrographs (a-b) of the gQD products at  $n = 18$  using  $W$ -cores. Inserted arrows highlight crystalline protrusions.

**Figure 2.13:** The powder XRD results for shell growth at  $W$ -cores at shell layers ( $n$ ) of 4 (i), 8 (ii), 12 (iii), and 18 (iv). The CdS ( $W$ , ZB) and ZnS ( $W$ , ZB) standards are provided for reference. XRD offset vertically for clarity.

**Figure 2.14:** Powder XRD simulations for a spherical 10 nm CdSe QD with either ZB or  $W$  crystallinity, compared with a 10 nm CdSe QD with equal mixtures of ZB +  $W$ . The reflections corresponding to the sum or  $\langle 110 \rangle + \langle 220 \rangle$ , and

$\langle 311 \rangle + \langle 112 \rangle$  correspond closely with the results shown in Fig. 5 and 7, whereas the sum of  $\langle 111 \rangle + \langle 002 \rangle$  is not observed in the experimental results, suggesting considerable stacking faults along those planes. XRD offset vertically for clarity.

**Figure 2.15:** (a-b) UV-vis spectra monitoring of *W*-CdSe cores during annealing in excess OAc (a) or DOA (b) from room temperatures (i), to 110°C for 1h (ii), to 190°C for 1hr (iii), to 240°C for 0.5h (iv) and 1.5 hr (v). (c-d) Similar UV-vis monitoring for annealing of *ZB*-CdSe core in excess OAc (c) and DOA (d) for similar temperatures and annealing times.

**Figure 2.16:** Powder XRD results characterizing the *W*- (a) and *ZB*- (b) CdSe cores (i) after completing the annealing cycle described in Fig. S7 with excess OAc (ii) and excess DOA (iii). CdSe (*W*, *ZB*) standards are provided for reference. XRD offset vertically for clarity.

**Figure 3.1:** Representative UV-Vis absorption (a) and the normalized PL emission spectra (b), XRD pattern (c), and TEM micrographs (e) and (f) shown for *W* core-A (i) and core-B (ii) respectively. Corresponding size distribution histograms provided as insets. The CdSe *W* standards are shown as reference.

**Figure 3.2:** (a) showing the UV-Vis absorption for *W* core (i),  $n = 4$  (ii), 8 (iii), 12 (iv) and 18 (v) (b) showing the PL emission for core (i),  $n = 4$  (ii), 8 (iii), 12 (iv), 18 (v) and 22 (vi) during shell growth. PL excitation wavelength is 400 nm.

**Figure 3.3:** (a) showing the redshift in PL emission peak  $\lambda_{PL}$  and (b) the variation in

QY% with increasing in shell layers ( $n$ ) starting from the core (i) ( $\lambda_{PL} = 532$  nm; QY% =  $2.7 \pm 0.9\%$ ), to  $n = 4$  (ii) ( $\lambda_{PL} = 592$  nm; QY% =  $30.3 \pm 1.3\%$ ), 8 (iii) ( $\lambda_{PL} = 605$  nm; QY% =  $22.5 \pm 1.8\%$ ), 12 (iv) ( $\lambda_{PL} = 615$  nm; QY% =  $18.3 \pm 2.3\%$ ), 18 (v) ( $\lambda_{PL} = 624$  nm; QY% =  $11.8 \pm 2.2\%$ ) and 22 (vi) ( $\lambda_{PL} = 614$  nm; QY% =  $14.7 \pm 1.5\%$ ) during growth of gQDs. PL excitation wavelength is 400 nm.

**Figure 3.4:** (a) The powder XRD patterns for shell growth at  $W$ -cores at shell layers ( $n$ ) of 4 (ii), 8 (iii), 12 (iv), 18 (v) and 22 (vi), (b)  $\langle 110 \rangle$  and  $\langle 002 \rangle$  peak shift during gQD growth, (c) FWHM variation of  $\langle 110 \rangle$  peak and (d) increasing lattice strain ( $\epsilon$ ) calculated along  $\langle 110 \rangle$  with increasing shell layers are shown. The XRD pattern for CdS ( $W$ ) and ZnS ( $W$ ) standards are provided for reference.

**Figure 3.5:** showing the trend in variation of  $\beta_{hkl}$ ,  $\beta_{Sch}$  and  $\beta_{Str}$  with increasing size of gQDs.

**Figure 3.6:** Representative TEM micrographs of the  $W$ -core ( $d = 2.9 \pm 0.4$  nm) (a), and gQD at shell growth layers of  $n = 4$  ( $d = 6.4 \pm 0.6$  nm) (b), 8 ( $l = 10.1 \pm 1.1$  nm,  $w = 6.7 \pm 0.8$  nm,  $l/w = 1.5 \pm 1.4$ ) (c), 12 ( $l = 14.6 \pm 1.1$  nm,  $w = 6.7 \pm 0.9$  nm,  $l/w = 2.2 \pm 1.2$ ) (d), 18 ( $l = 19.2 \pm 2.1$  nm,  $w = 6.9 \pm 0.9$  nm,  $l/w = 2.8 \pm 1.3$ ) (e) and 22 ( $l = 23.8 \pm 2.8$  nm,  $w = 9.3 \pm 1.4$  nm,  $l/w = 2.59$ ) (f). Corresponding size distribution histograms are provided.

**Figure 3.7:** HRTEM micrograph of SILAR gQDs at  $n = 22$  (a) The corresponding ED pattern is provided (b). The diffraction spots resulting from lattice planes typical of a  $W$  crystal are shown.

**Figure 3.8:** UV-vis and PL spectra shown for S<sub>8</sub>/ODE (a, b) S-TOP (c, d) and DDT (e, f) gQDs at core (i),  $T_1$  (ii),  $T_2$  (iii) and  $T_3$  (iv).

**Figure 3.9:** Figure showing temporal evolution of  $\lambda_{PL}$  shift (a), QY% variation (b), and diameter change (c) at  $T_1$ ,  $T_2$ , and  $T_3$  for gQD growth at  $W$ -core ( $T_0$ ), employing S<sub>8</sub>/ODE, S=TOP and DDT shell precursors. PL excitation carried out at 500 nm.

**Figure 3.10:** Representative TEM micrographs and size distribution of the  $W$ -core  $T_0$  ( $d = 2.9 \pm 0.4$  nm) (a), and S<sub>8</sub>/ODE gQD at  $T_1$  ( $d = 10.2 \pm 0.9$  nm) (b),  $T_2$  ( $d = 11 \pm 0.9$  nm) (c), and  $T_3$  ( $d = 11.2 \pm 0.9$  nm) (d). Corresponding size distribution histograms are provided.

**Figure 3.11:** Representative TEM micrographs and size distribution of the  $W$ -core  $T_0$  ( $d = 2.9 \pm 0.4$  nm) (i), and S=TOP gQD at  $T_1$  ( $d = 8.6 \pm 0.9$  nm) (ii),  $T_2$  ( $d = 10.3 \pm 1.2$  nm) (iii), and  $T_3$  ( $d = 11.6 \pm 1.3$  nm) (iv). Corresponding size distribution histograms are provided.

**Figure 3.12:** Representative TEM micrographs and size distribution of the  $W$ -core  $T_0$  ( $d = 3.0 \pm 0.5$  nm) (a), and DDT gQDs at  $T_1$  ( $d = 6.0 \pm 0.7$  nm) (b),  $T_2$  ( $d = 8.0 \pm 0.8$  nm) (c), and  $T_3$  ( $d = 10.9 \pm 1.2$  nm) (d). Corresponding size distribution histograms are provided.

**Figure 3.13:** The powder XRD results for shell growth at  $W$ -cores at  $T_1$  (ii),  $T_2$  (iii), and  $T_3$  (iv). The XRD pattern for the  $W$  CdSe core  $T_0$  (i), CdS ( $W$ ) and ZnS ( $W$ ) standards are provided for reference.

**Figure 3.14:** (a) HRTEM micrograph of S<sub>8</sub>/ODE gQDs at  $T_3$  (9 hr) stage and (b) The corresponding ED pattern is provided. Diffraction spots resulting from

lattice planes typical to *ZB* crystal structure are observed.

**Figure 3.15:** (a) HRTEM micrograph of S=TOP gQDs at  $T_3$  (9 hr) stage. (b) The corresponding ED pattern is provided. Diffraction spots resulting from lattice planes typical to both *W* and *ZB* crystal structure are observed.

**Figure 3.16:** (a) HRTEM micrograph of DDT gQDs at  $T_3$  (9 hr) stage, (b) the corresponding ED pattern is provided. Debye rings due to diffraction spots from identical lattice planes typical to *ZB* crystal structure are observed.

**Figure 3.17:** shows the XRD pattern for CdSe/CdZnSe gQDs starting from the core (i), at  $T_1$  (ii),  $T_2$  (iii) and  $T_3$  (iv). The CdSe *W* standards are shown as reference.

**Figure 3.18:** Schematic outline summarizing the disparate growth morphology of gQDs starting from *W*–CdSe core, under diverse synthetic conditions.

### List of Tables

**Table 3.1:** Molar concentrations of the CdSe core and shell precursors employed in the seeded growth syntheses

**Table 3.2:** showing the calculation of  $\beta_{\text{Sch}}$ ,  $\beta_{\text{hkl}}$ ,  $\beta_{\text{Str}}$  and strain for the gQDs along  $\langle 110 \rangle$  facet

### **List of Abbreviations**

Ar	Argon
AR	Auger recombination
CdO	Cadmium oxide
CdS	Cadmium sulphide
CdSe	Cadmium selenide
CdSO <sub>4</sub>	Cadmium sulfate
CdZnS	Cadmium zinc sulphide
Cl	Chloroform
CuCl	Cuprous chloride
DDA	Dodecylamine
DOA	Dioctylamine
EtOH	Ethanol
FWHM	Full width half maxima
gQDs	Giant quantum dots
HDA	Hexadecylamine
HPA	Hexadecylphosphonic acid
HRTEM	High resolution TEM
LEDs	Light-emitting diodes

$(\text{NH}_4)_2\text{S}$	Ammonium sulfide
OAc	Oleic acid
ODE	1-octadecene
ODPA	Octadecylphosphonic acid
PL	Photoluminescence Spectroscopy
QDs	Quantum dots
QRs	Quantum rods
QY	Quantum Yield
R6G	Rhodamine 6G
SA	Stearic acid
Se	Selenium powder
SILAR	Successive ionic layer adsorption and reaction
TBP	Tributylphosphine
TEM	Transmission Electron Microscopy
TI	Toluene
TOP	Trioctylphosphine
TOPO	Trioctylphosphine oxide
UV-vis	UV-visible Spectrophotometry



W	Wurtzite
XRD	Powder X-ray diffraction
ZB	Zinc Blende

# Chapter 1

## Introduction

### 1.1 Quantum dots

#### 1.1.1 Definition, history and applications

Quantum dot (QDs) are semiconductive nanocrystals that have unique optoelectronic properties that stem from quantum confinement in at least one spatial dimension.<sup>1-3</sup> These properties can be manipulated by changing composition and morphology, which can lead to a wide variety of applications ranging from photovoltaics and lasers to biosensors.<sup>4-6</sup> QDs were first synthesized in the 1980s by independent pioneering work by Ekimov<sup>7,8</sup> and Brus,<sup>9</sup> that elucidated the unique size – optical property interdependency. This work was followed by organometallic and inverse micelle synthetic route of Steigerwald.<sup>10</sup> QD synthesis has seen rapid advancement in the last couple of years. The unique solution based thermal decomposition techniques employed by Bawendi, Alivisatos, Guyot-Sionnest and Peng<sup>11-14</sup> in the 1990s had yielded high quality crystalline QDs with considerable photoluminescence yield and variety of shapes and sizes. This progression had led to extensive research directed towards the synthesis,<sup>4,15-22</sup> functionalization,<sup>6,23-26</sup> and characterization<sup>27-38</sup> of QDs for applications in biomimetic energy transfer,<sup>39-41</sup> solar cells and lasers,<sup>42-45</sup> light emitting diodes (LEDs)<sup>46,47</sup> as well as in biolabeling and biotechnology.<sup>24,48-50</sup> Despite these advances, a number of unknown exist as are challenges that need to be overcome.

### **1.1.2 Quantum confinement effect and optoelectronic properties**

Molecules are composed of only a few atoms where the linear combination of the atomic orbitals can explain the formation of the bonding and antibonding molecular orbitals separated by an energy gap. In case of a bulk material, an enormous number ( $6.023 \times 10^{23}$  for each mole of the substance) of such atomic orbitals overlap to form continuous bands. In case of a bulk semiconductor, the continuous bands are separated by a distinct band gap ( $E_g$ ) between a valence band and conduction band. Quantum dots (QDs) have electronic properties, which are intermediate to discrete molecules and a bulk semiconductor. In QDs, atoms numbering from a few hundreds to a few thousands are present, in which the atomic orbitals form quantized level of bands separated by a band gap. Thus starting from a bulk semiconductor where we have continuous bands (valence, conduction band) separated by a band gap, in QDs, with the smaller number of overlapping orbitals, the continuous bands themselves split into discrete quantized energy levels, in addition to the band gap residing at the band edge as shown in Fig 1.1.

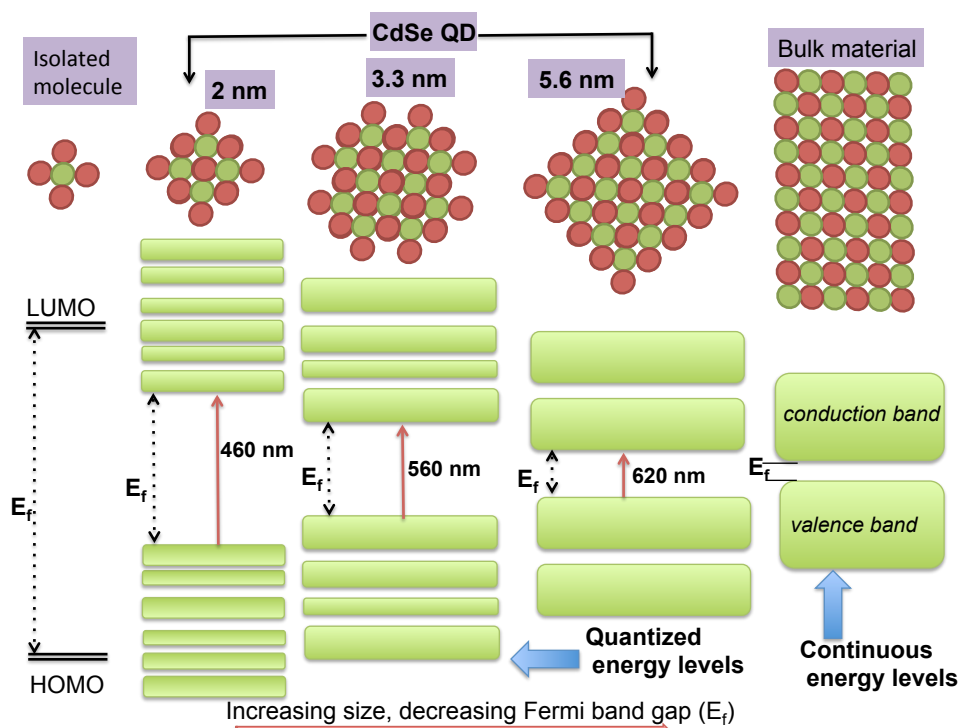


**Figure.1.1:** Schematic representation illustrating the quantum size effect in CdSe QDs

Excitation of an  $e^-$  from the valence band to the conduction band can be achieved by the absorption of electromagnetic radiation of energy compatible with the band gap. This excitation of  $e^-$  from the valence band to the conduction band results in the formation of a hole ( $h^+$ ) in the valence band. The  $e^-$  and  $h^+$ , do not move independent of each other. Rather, due their opposing charge, they experience Coulombic attractions, and form a pair termed as exciton, possessing lowest energy state residing slightly below the lowest level of conduction band.<sup>51</sup> Owing to the small effective mass of the charge carriers and high dielectric constant of the surrounding, exciton radius becomes quite large, or in other words the excitonic wavefunction regime extends over several lattice spacings. This Bohr excitonic radius has fixed values in bulk semiconducting materials such as  $\sim 5.6$  nm in CdSe.<sup>3</sup> When the radius of the particle is comparable to the Bohr radius of the exciton in the bulk material, quantum mechanical effects are exhibited.<sup>2,3,52</sup> In such a situation,

the exciton are referred to as being ‘confined’ in crystal dimensions (or quantum mechanically confined in space) in which the carriers seems to possess enhanced kinetic energy to make up for the size constriction. This confinement of the exciton in QD dimensions resembles a classical case of a particle in a three-dimensional box, resulting in quantization of energy levels and energy gaps residing amongst them, the latter strongly depending on the size of the box. Analogous to the particle in a box situation, decreasing the size (or the volume) of the QD, energy separation between the quantized levels increases. This is termed as the quantum confinement effect.<sup>2,3</sup> Size manipulation in a QD thus provides a high control over its photophysical properties. The band gap is found to increase, with the decreasing size of the nanocrystal, and consequently the energy associated with the electronic transition shifts to a higher energy (Fig. 1.1). The confinement of the exciton plays an important role in QD photophysics. The Bohr exciton radius ( $a_0$ ) describes the spatial extension of the exciton in solids, is a characteristic of the material in consideration and can be evaluated by the equation ,

$$a_0 = \epsilon_0 \epsilon_{nc} \hbar / \mu e^2$$

where  $\epsilon_0$  is the permittivity of vacuum,  $\hbar$  is the reduced Planck’s constant,  $\epsilon_{nc}$  is the dielectric constant of semiconductor material,  $\mu$  the reduced mass of exciton and  $e$  is the charge of an  $e^-$ .<sup>53</sup>  $a_0$  is found to vary from 1-50 nm depending on the material under consideration, for CdSe it 5.6 nm.<sup>3,4,8</sup> As mentioned earlier, the quantum confinement starts affecting the electronic wavefunction when QD dimensions approach  $a_0$ , leading to the formation of discrete energy levels instead of quantized bands. Three different regimes are defined taking the  $r/a_0$  ratio value:  $r/a_0 < 1$  (strong confinement regime);  $r/a_0 = 1$  intermediate confinement regime and  $r/a_0 > 1$  weak confinement regime. These

energy levels lead to unique photophysics that can be explained with the help of a Jablonski diagram as showed in Fig 1.2.

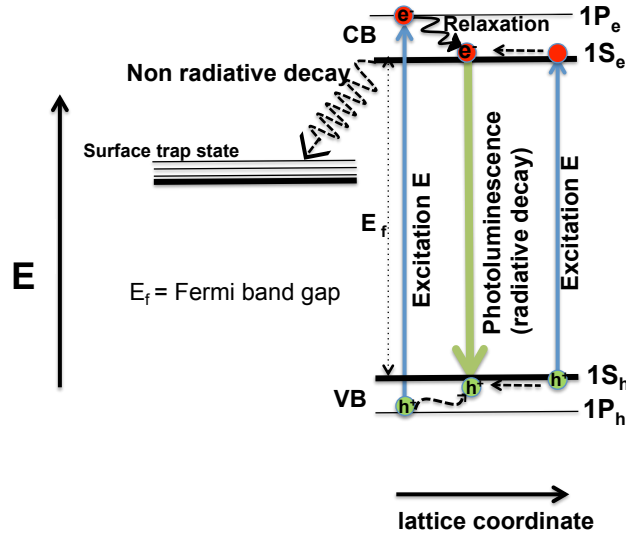


**Figure 1.2:** Jablonski diagram: schematic representation of the involved absorption and emission processes amongst the exciton states of QD

Excitation of an  $e^-$  from the valence band to the conduction band can be achieved by the absorption of electromagnetic radiation of energy compatible with the band gap or higher excited state energy difference. When the electron is promoted however, the energy of absorption is quantized in the sense that selection rule allows only those optical transitions where coupling between electron and hole states having identical quantum number is probable. Once excited to the conduction band, the electron leaves behind a hole in the valence band. If the electron has been excited to higher excited level in conduction band, it relaxes to the lowest energy state via phonon relaxation (internal conversion) (Fig 1.2). The duration of stay of the electron in the conduction band is measured as the excited state lifetime. After reaching  $1S_e$  state the electron can descend to the valence band to recombine with the hole, releasing energy in the form of photon

emission (radiative decay) or it can get trapped in the surface trap states located close to conduction band and undergo non-radiative decay.<sup>54</sup>

Depending on the number of quantum mechanically confined spatial dimensions; nanomaterials can be classified as quantum wells, (1D confinement of exciton, free on the other two dimensions), quantum wires (2D confinement of exciton, free on the third dimension) or QDs (confinement of the exciton in all three dimensions) (Fig. 1.3).

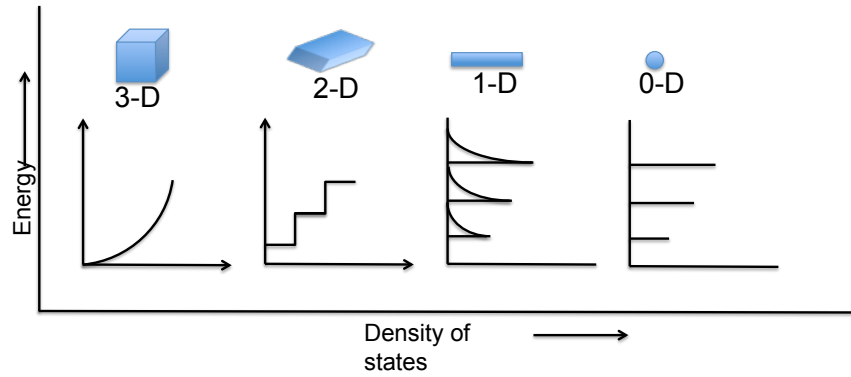


**Figure. 1.3:** Illustration showing idealized density of electronic states diagram for bulk material (3D), quantum wells (2D), quantum wires and rods (1-D) and QDs (0D)

### 1.1.3 Crystal structure of quantum dots

Binary II-VI semiconductors such as CdSe, CdS, CdTe, ZnS, ZnS etc. are found to crystallize in zinc blende (*ZB*) and hexagonal wurtzite (*W*) crystallographic forms in nature.<sup>51</sup> These two crystallographic forms, essentially differ in the spatial arrangement of cations and anions in their respective unit cells, while maintaining the stoichiometric ratio of 1:1(cation : anion). More specifically, *ZB* involves ABCABC close packing sequence of the ions resulting from cubic close packing (ccp).<sup>55</sup> In the *ZB* unit cell, the cation (or anion) occupies only one type (either  $T^+$  or  $T^-$ ) of tetrahedral hole and is coordinated to four neighbors of opposite charge. On the other hand, hexagonal *W* involves an ABAB close packing array of the ions, resulting from hexagonal close packing (hcp).<sup>55</sup> Further, in a hexagonal *W* unit cell the ions occupy only one type of tetrahedral site, and

coordinates to four neighbors of opposite charge. Figure 1.4 shows a typical unit cell for *ZB* CdSe (a) and *W* CdSe (b).

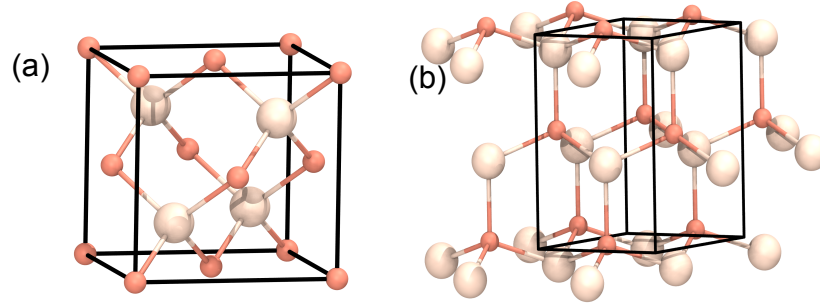


**Figure 1.4:** Ball and stick model of CdSe *ZB* unit cell (a), and CdSe *W* unit cell (b). Cd atoms denoted by copper colored balls and Se denoted by white balls.

## 1.1.4 Synthesis of quantum dots

### 1.1.4.1 Background

In the 1980s Ekimov and co workers were amongst the first to be credited with the synthesis and coining of ‘quantum dot’ in their remarkable study on quantum confinement effects in CuCl (a I-VII semiconductor<sup>56</sup>) prepared in silica glass matrix.<sup>7</sup> At almost the same time Brus and co workers had notably studied the band edge luminescence properties of CdS nanoparticles<sup>9</sup>. The synthesis of CdS nanoparticles involved the reaction between CdSO<sub>4</sub> and (NH<sub>4</sub>)<sub>2</sub>S in water, in presence of maleic anhydride or styrene as a capping agent,<sup>52</sup> exploiting classical wet colloidal chemistry precipitation reactions in which metal cations would directly react with inorganic chalcogenide sources, in the form,  $M^{+x} + S^{2-} \rightarrow M_{x/2}S$ .



In an alternate method, CdSe nanoparticles had been synthesized via inverse micelles pathway by Steigerwald<sup>10</sup> and Alivisatos.<sup>57</sup> In this synthesis, a microemulsion of dioctylsodium sulfosuccinate, water and heptane was prepared, into which, aqueous cadmium perchlorate  $[\text{Cd}(\text{ClO}_4)_2]$  was added, followed by addition of a heptane solution of trimethylsilyl selenide  $[\text{Se}(\text{SiCH}_3)_2]$ . Room temperature reaction of Cd stock solution with Se precursor yielded phenyl passivated CdSe clusters for the first time, which were dried to avoid flocculation. Most of these early syntheses, broadly classified as ‘precipitation reaction’ methods,<sup>58</sup> were able to synthesize nanometer sized semiconductors from fast precipitation of the synthesized products at room temperature. Thus, the products resulting from these reactions had poor crystallinity and photophysical properties along with vastly non-uniform size distributions, which made improved synthetic protocols a necessity.

#### **1.1.4.2 Hot injection/Thermal decomposition method**

An alternate organometallic route was first published by Bawendi and coworkers in 1993.<sup>11</sup> The method employed the high temperature thermal decomposition of organometallic precursors like  $\text{Cd}(\text{CH}_3)_2$  (dimethyl cadmium) and  $\text{TOP}=\text{Se}$  (trioctylphosphine Se) in a high boiling non-polar coordinating solvent trioctylphosphine oxide (TOPO). The synthesis essentially was carried out in an inert atmosphere, employing precursors and high temperature reaction facilitating coordinating solvent. The key goal to achieve monodisperse QDs with high uniformity was achieved in the hot injection synthesis by employing synthetic temperature of 300 °C and segregating the nucleation and growth stage of the nanocrystals during synthesis. The rapid injection and mixing of highly pyrophoric precursors  $\text{Cd}(\text{CH}_3)_2$  and  $\text{TOP}=\text{Se}$  in TOPO at elevated

temperatures results in high concentration of monomers (sudden supersaturation) in solution inducing an initial burst of quantum dot nuclei formation almost instantaneously. Following nucleation, the concentration of monomers in the solution are depleted to a great extent thus formation of new nuclei are constrained; a period of slow controlled growth (due to coordination by TOPO) of the formed nuclei from the residual monomers ensues. The swift nucleation and comparatively slower growth steps had been described by Lamer<sup>59</sup> ensuring the narrow size distribution in the final product. The highly reactive, pyrophoric dimethyl cadmium  $[\text{Cd}(\text{CH}_3)_2]$  has been substituted with an alternative safer Cd source, CdO in the later years.<sup>16</sup>

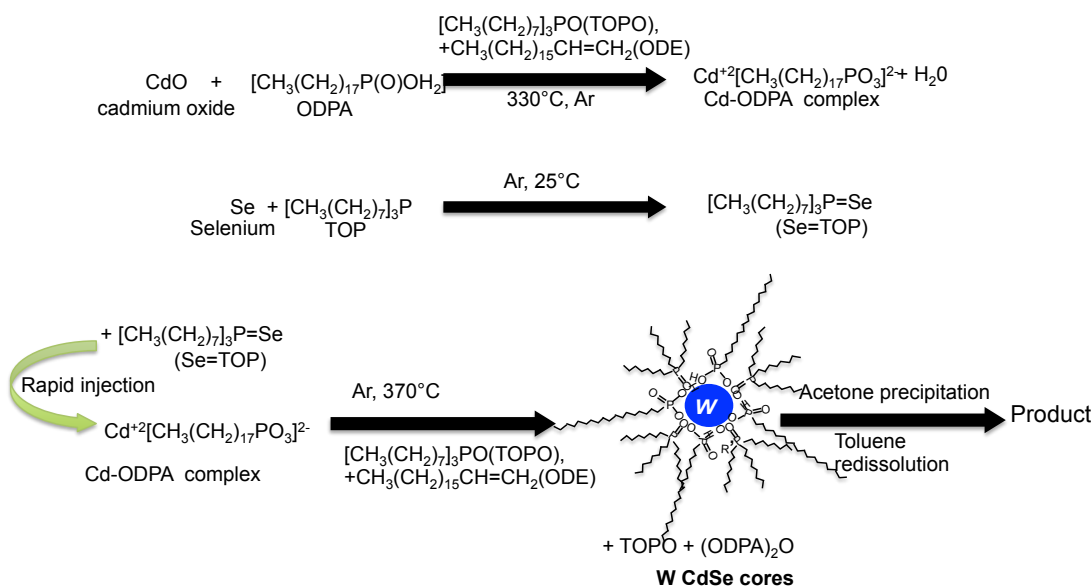


**Figure 1.5:** Schematic showing CdSe core synthesis by hot injection synthesis. TOPO and octadecylphosphonate ligands constitute the capping layer of the synthesized cores

Fig. 1.5 shows a schematic for the synthesis of CdSe nanocrystals via a typical hot injection technique. For the synthesis,  $\text{Cd}^{+2}$  precursors such CdO is dissolved in a mixture of trioctylphosphine oxide (TOPO, also the coordinating solvent) and ODE (inert solvent), both of which possess high boiling points ( $>300^\circ\text{C}$ ) and octadecylphosphonic

acid (ODPA) under Ar atmosphere at 330 °C. The Se precursor (Se=TOP) is prepared in the glovebox (inert atmosphere) by dissolving Se powder in trioctylphosphine (TOP). Following the dissolution of CdO, forming the cadmium octadecylphosphonate complex [Cd-ODPA] the temperature of the reaction medium is increased to 370°C. After the stabilization of the temperature, Se=TOP is rapidly injected into the hot reaction mixture, to induce CdSe nucleation and almost instantaneous growth. Further, unique control over the final sizes of the synthesized nanocrystals can be achieved just by altering the annealing time during growth. The QD nanocrystal suspensions in organic solvent resulting from Bawendi's work exhibited excellent crystallinity and discrete, resolved optical transitions. The narrow size dispersions (<10%) and considerably high band edge luminescence enabled optical studies to be performed on the synthesized nanocrystal ensembles. The high degree of reproducibility of the hot injection synthetic methodology had resulted in a wide variety of semiconductive nanocrystals syntheses such as CdS, CdTe,<sup>11</sup> ZnSe,<sup>60–63</sup> ZnS,<sup>61</sup> PbS,<sup>64</sup> PbTe,<sup>65,66</sup>, PbSe,<sup>67,68</sup> InAs,<sup>69,70</sup> InP<sup>69,71</sup> etc.

Hot injection synthesis has been further exploited to alter the growth morphology of QDs by two approaches; (a) employing facet-selective ligands during synthesis altering the surface energy and promoting anisotropic growth as showed by the work of Alivisatos and coworkers<sup>72</sup> and (b) altering monomer chemical potential in the solution by controlling the concentration of precursors as illustrated by the work of Peng.<sup>16,73</sup> Further research in the later years showed that modified hot injection techniques employing greener precursors like CdO instead of Cd(CH<sub>3</sub>)<sub>2</sub>, non-coordinating solvents like octadecene, in presence of alkylamines (octadecylamine, dodecylamine, etc.) and oleic acid, stearic acid (in place of phosphonic acids) could be carried out at lower

temperatures(200-250°C), yielding good quality nanocrystals in less hazardous reaction conditions.<sup>25,74–76</sup>

#### **1.1.4.3 Core- shell quantum dots**

QD properties are highly susceptible to the surrounding environment. Passivating the surface with organic ligands is an established option but not the best one as often it is observed due to the dynamic nature of QD-ligand bonding, and the vulnerability of organic ligands to photobleaching and degradation, incomplete passivation results in poor QYs.<sup>77,78</sup> To address this, researchers deposit a second semiconductor layer on the surface of QD core. This shell had shown excellent passivation of the surface defect sites leading to the formation of a core shell nanoparticle. Epitaxial growth of the shell on the core requires the choice of material be made not only the basis of appropriate band alignment as the sole criterion, but also ensuring the core and shell are coherent crystallographically. This means, that the core and shell material should ideally crystallize in the same structure and exhibit small lattice mismatch amongst them. During initial stages of epitaxial growth, shell attains the lattice parameters of the core crystal (which differs from its own set of lattice parameters). Thus, in case of thick shells grown on the core with a view of enhancing PL QY by isolating the core exciton completely from the shell interface, often result in strained core shell interface if the lattice parameter mismatch is too high. This strain at the core shell interface gives rise to trap states, which adversely affects the PL QY. Thus there exists an optimum shell thickness to ensure complete passivation of the core at the same time not inducing strain at the core shell interface.

Such epitaxial growth of shell is traditionally carried out by two methodologies (a) seeded growth and (b) SILAR (successive ion layer adsorption reaction).

#### 1.1.4.3.1 Seeded growth

In seeded growth firstly CdO is heated with a mixture of ODPA (octadecylphosphonic acid) and HPA (hexadecylphosphonic acid) in TOPO and ODE solvent under Ar flow, under Ar flow, when CdO dissolves, to form the corresponding Cd-octadecyl/hexadecylphosphonate complex (cationic shell precursor) (~330°C). The temperature of the reaction is further elevated to ~ 370°C. At this point, an injection containing CdSe core (seed) and S=TOP (S<sub>8</sub> in TOP, sulfur shell precursor, separately prepared in the glovebox) is rapidly injected into the reaction medium. This results in rapid growth of the CdS shell on the CdSe core. Fig 1.6 shows the schematic for a typical seeded growth resulting in the formation of CdSe/CdS quantum rods.

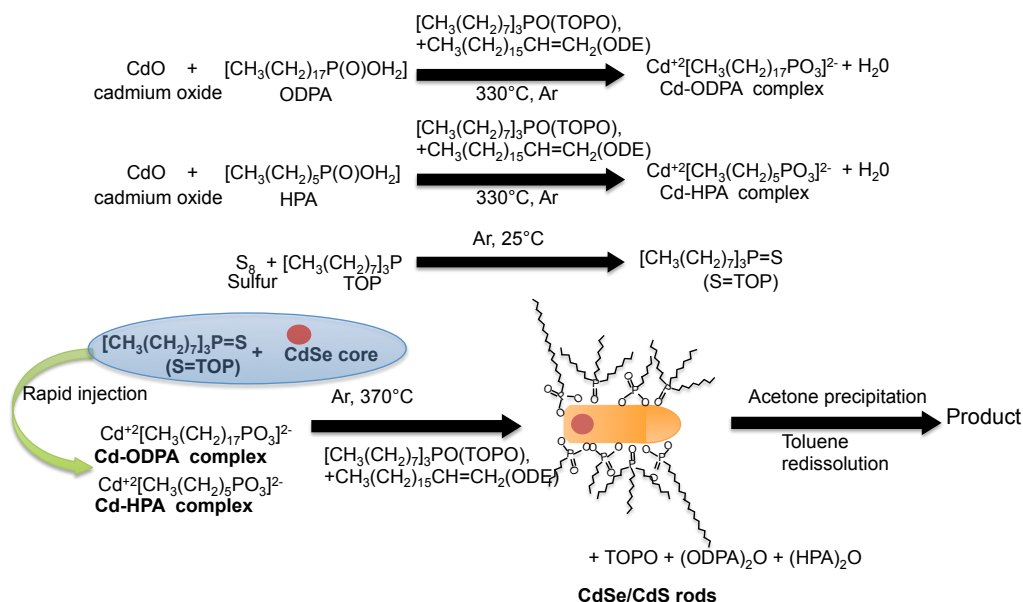


**Figure 1.6:** Schematic showing seeded growth employed to grow CdS shell on CdSe cores.

Seeded growth often results in the formation of anisotropic nanocrystals like nanorods, nanowires, tetrapods as pioneered by the work of Peng<sup>73,79</sup> and Alivisatos<sup>15,80</sup> and in the later years by Talapin,<sup>20,81</sup> Banin and Manna<sup>19,82,83</sup>, owing to the high temperature of the synthesis facet selectivity of the phosphonic acid ligands and high concentration of shell precursors present during the reaction. I have employed seeded growth for my gQD synthesis (Chapter 3), employing oleic acid in place of phosphonic acids.

#### **1.1.4.3.2 SILAR (Successive Ion layer adsorption reaction)**

SILAR (Successive Ion Layer Adsorption and Reaction)<sup>75</sup> is one of the most extensively used synthetic routes techniques for shell deposition on QD cores. The process involves alternate deposition of anion and cation layers on the QD surface. The SILAR process is heavily inspired by the chemical bath deposition technique used for epitaxial growth of conformal thin films on solid substrates in solutions, having the fundamental concept of atomic layer epitaxy (ALE) observed in Molecular Beam Epitaxy (MBE) literature.<sup>84</sup> In SILAR alternate layers of cationic and anionic species are deposited on the surface of the QD core, with two basic goals (1) uniform monolayer growth on each QD core of the ensemble (i.e. each core present in solution) and (2) restricting the simultaneous presence of both ionic precursors in solution so as to avoid homogenous nucleation of shell material. To achieve both goals, calculated amount of each precursor is added in order to saturate the available surface sites for all the QDs (so that uniform conformal shell growth of the entire ensemble results in structural homogeneity) and also to ensure no excess precursor is left free in solution (thereby avoiding homogenous nucleation, when the subsequent addition of opposite charged shell precursor is performed for further growth of the shell).

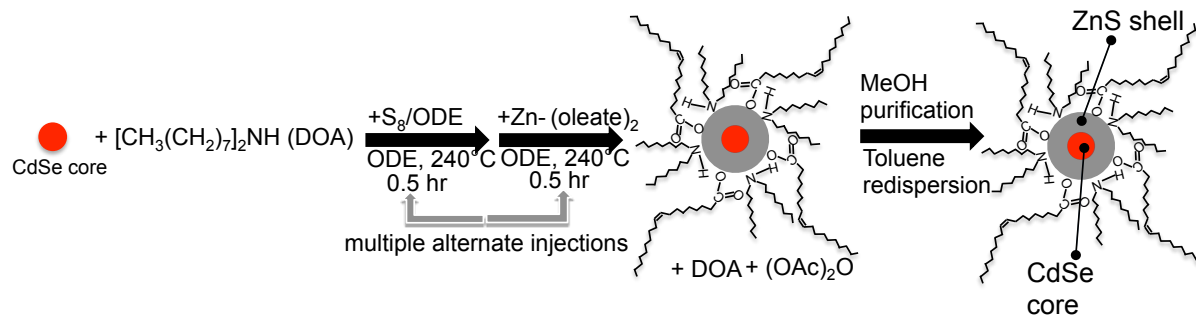


**Figure 1.7:** Schematic showing layer by layer SILAR process employed to grow ZnS shell on CdSe cores

Fig. 1.7 shows a schematic for the growth of ZnS shell on a CdSe core involving typical SILAR process of shell addition. Briefly, firstly the cationic shell precursor  $Zn^{+2}$  precursor is prepared separately by dissolving ZnO is dissolved in oleic acid (OA) at  $\sim 200^\circ C$  under Ar flow to formation  $Zn-(oleate)_2$  complex. Then the anionic shell precursor ( $S^{2-}$ ) is separately prepared by dissolving elemental  $S_8$  in TOP (forming  $S=TOP$ ), or by dissolving elemental  $S_8$  in octadecene (ODE). Once both shell precursors have been synthesized, CdSe core is dispersed in alkylamines like oleylamine, dioctylamine or octylamine and ODE (solvent) in a four necked reaction flask and the mixture is heated to shell growth temperature ( $\sim 200-240^\circ C$ ) under Ar flow. At this point calculated amounts of sulfur and  $Zn^{+2}$  shell precursors are alternately injected into the reaction medium, allowing annealing time in between the injections. In this manner, ZnS shell is grown in a slow layer-by-layer fashion on the CdSe core till the desired shell thickness is achieved. The slow addition of shell precursors in this process, and annealing time between the injections ensures the formation of almost defect free, high crystalline core - shell nanocrystals with high QY%. SILAR process has been successfully employed in the synthesis of a wide variety of core- shell nanocrystals including CdSe/ZnS, CdSe/CdS, CdSe/CdS/ZnS.<sup>43,78,85-88</sup> In my research I have employed the SILAR process extensively for the synthesis of multishell CdSe/CdZnS giant quantum dots.

### 1.1.4.3.3 Types of core shell systems

Depending on the energy levels and band gaps involved, the generated core shell structure may be of the following types; (a) Type – I, where the shell bandgap is higher than the core bandgap, resulting in the confinement of the exciton ( $e^-$  and  $h^+$ ) onto the core itself (e.g. CdSe/ZnS), (b) Type – II, where either the conduction or the valence band of the shell lies in close proximity to the band gap of the core, resulting in the confinement of the  $h^+$  to the core while  $e^-$  is localized in the shell or vice-versa depending on the location of the shell bandgap (e.g. CdSe/ZnTe, CdTe/CdSe) and (c) quasi Type – II where the energy offset of the shell conduction band (with respect to that of the core) is too small to keep the  $e^-$  localized to the core. As a result,  $h^+$  remains confined to the core, while  $e^-$  is delocalized over the core and the shell. e.g. CdSe/CdS rods and dots. If the case be such that the valence band offset is too small amongst the core and the shell, the  $e^-$  remains confined to core, while the hole is delocalized over the core and shell (e.g. CdS/ZnSe). (Fig.1.8) shows the three types of band alignment discussed.

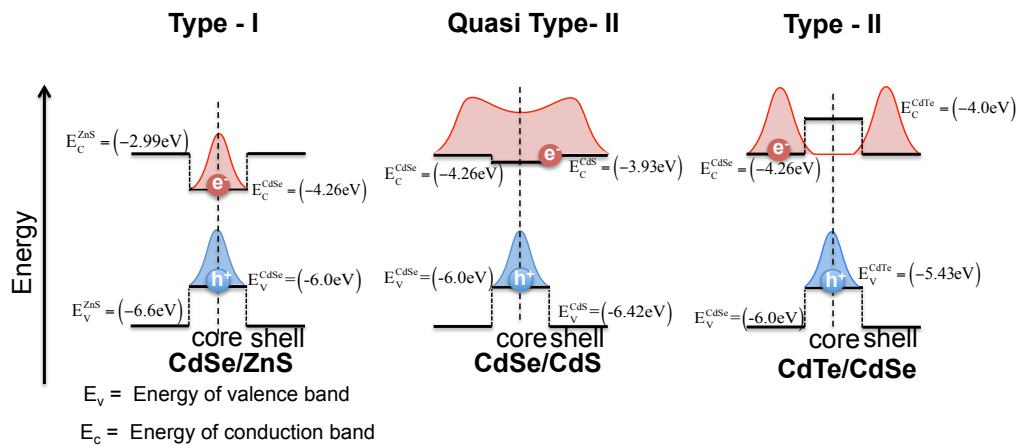


**Figure 1.8:** Scheme showing the three limiting charge carrier localization regime in core/shell QDs.



#### **1.1.4.3.4 Core/shell/shell and graded alloy shell QDs**

As discussed earlier, the lattice mismatch of the core and shell seriously limits the possibility growing a shell of considerable thickness without adversely affecting the QY. To circumvent this problem, the growth of intermediate “wetting layer” sandwiched between the core and outer shell has been proposed to either yield core/shell/ shell system like CdSe/ZnSe/ZnS or a core/graded alloy shell like CdSe/Cd<sub>x</sub>Zn<sub>1-x</sub>S has been fabricated. In both of the structures, intermediate layer reduces the lattice mismatch, while outer ZnS shell imparts complete passivation and exciton confinement yielding impressive QYs.<sup>89,90</sup>

#### **1.1.4.3.5 Blinking in QDs**

Surface defects resulting from atom dislocations, dangling bonds, strains developing due lattice mismatch between the core and the shell, are often found to act as electron trap states, thus facilitating non-radiative recombination processes, resulting in decreased ensemble QY%. In addition, the blinking phenomenon or ‘fluorescence intermittency’ observed in case of single QD fluorescence studies, are also found to be closely associated with occurrence of surface trap states/ defects.<sup>3</sup> Trap states for the hole might reside at the core shell interface due to defects during shell growth. Blinking is large fluctuations in the photoluminescence intensity observed during single QD studies, where their photoluminescence is observed to turn ‘off’ and ‘on’ intermittently even under constant photoexcitation. The blinking phenomenon is well understood; the ‘on’ state (where normal radiative recombination of the exciton is occurring) and ‘off’ states (where the fluorescence is quenched) of the QD are understood to result from two

causes.<sup>91–93</sup> First, due to the generation of multiple excitons in a QD during photon irradiation, the strong interaction amongst them might result in the ejection of an  $e^-$  or  $h^+$  to the surrounding matrix, resulting in a charged nanocrystal. Any additional exciton generated at this point, is found to decay through fast non-radiative processes, commonly called Auger recombination (AR). Thus the QD stays ‘off’ till the time it is neutralized by the surrounding matrix or neighboring QD. This is termed as A-type blinking and is characterized by a decreased QD lifetime. The other type of blinking, termed as B-type blinking is found to occur due to the trapping of ‘hot’ (energetic) electrons in interband surface trap states, instead of relaxing to lowest excited level and then radiatively recombining with the hole. Those trapped electrons recombine with the hole in a non-radiative manner, resulting in fluorescence quenching. Thus this type of blinking does not involve QD charging and nor does it require AR processes to reduce QD PL emission. Rather, fluctuations in the occupancy of the surface trap states leads to fluctuating PL intensity or blinking and thus B-type blinking is found to be independent of QD lifetime.

The blinking phenomenon presents some serious disadvantages for the application of QDs in some specialized applications, which necessitate stable emission at single quantum dot level like long duration single particle tracking, single photon sources, fabrication of emitting layers in solid state LEDs etc. To synthetically address these challenges, ligands (surface associated electron donating species) such as  $\beta$ -mercaptoethanol, propyl gallate, oligo (phenylene vinylene) to prevent surface electron trapping have been employed,<sup>77,94–96</sup> but have been found to be significantly influenced by local chemical environment, time and ligand coverage.<sup>77,96</sup> Alternative approach

involving heterostructuring by using alloyed CdZnSe (core)/ZnSe (shell) have been employed,<sup>97</sup> but exhibits serious limitations.<sup>92</sup>

#### **1.1.4.3.6 Giant Quantum Dots (gQDs)**

One way researchers try to overcome blinking is to deposit an ultrathick shell (>19 monolayers) of CdS on the surface of the CdSe core, which seems to have addressed the QD blinking problem to a good extent.<sup>78</sup> The thick inorganic shell in these QDs (termed as giant quantum dots (gQDs)) has been observed to serve as an effective barrier to surface carrier trapping, also reducing photoionization of the gQDs, by effectively isolating the core exciton from the surface interface, thereby suppressing AR processes.<sup>43,98</sup> Though research is still underway for the optimized synthetic condition for the gQDs, the results look promising. The gQDs have exhibited significant ‘on’ time fractions compared conventional core shell quantum dots.<sup>92</sup> Further, the QY% for these gQDs have been found to be high and extremely stable to multiple precipitation – redissolution cycles, underlining the effective isolation of core exciton from the surface chemical environment.<sup>78</sup> The gQDs are found to be exhibit considerable stable to photobleaching, as compared to conventional QDs. Further, the large Stokes shift associated with the thick epitaxial shell have been reported to demonstrate improved performance as down conversion material for lighting applications.<sup>43,99,100</sup> The degree of blinking suppression has also been hypothesized to be strongly influenced by the thickness of the shell, where a nanoparticle volume of  $\sim 750 \text{ nm}^3$  has been stated as the optimum size for most efficient blinking suppression.<sup>92,93,101</sup> These gQDs are synthesized

by a SILAR shell deposition on the CdSe. A schematic showing a typical gQD synthesis involving a graded alloy shell epitaxially grown on a CdSe core (Fig. 1.9)

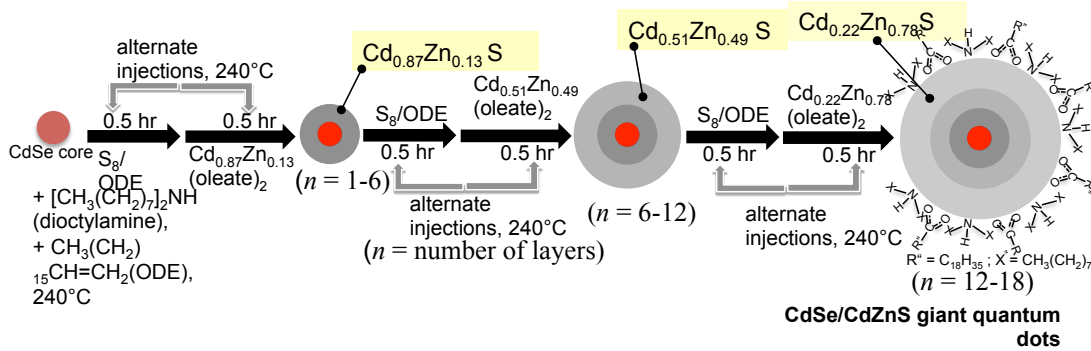


**Figure 1.9:** Schematic showing a typical synthesis of CdSe/CdZnS gQD. Dioctylamine and oleate ligands are shown as the capping agents

### 1.1.5 QD shapes

As observed in the case of crystals occurring in the macroscopic world, e.g. diamonds, amethyst, jade, ice etc., the surfaces of QDs are found to be highly faceted. In general, facet can be regarded as the flat surfaces occurring at the periphery of a 3D geometrical shape. In the case of a QD, they are essentially the exposed faces of unit cells, occurring at the surface of the nanocrystal, which marks the termination of the crystal structure. The occurrence of facets in a quantum dot results from a disparity in growth pattern/ growth rate of the various crystal faces of a unit cell. Syntheses carried out with quantum dot crystals with high symmetry, e.g. *ZB* etc. result in isotropic growth into faceted morphologies. In the case of quantum dots with lower symmetry e.g. *W* however, anisotropic growth pattern with unique growth directions are often arrived at during synthesis. For this particular study, we confine the discussions within the realm of growth patterns of various faces of a hexagonal *W* crystal, which results from the highly ordered periodic arrangement of *W* unit cell (Fig. 1.10a) in three dimensions.

### 1.1.5.1 Crystal structure

As seen from Figure 1.10 b, the faces of a hexagonal crystal are quite different in their chemical behavior, depending on the nature of atoms constituting that particular face. For example the horizontal basal planes  $\langle 001 \rangle$  and  $\langle 00\bar{1} \rangle$  planes lying on the  $\langle 002 \rangle$  direction expose either cations or anions and are referred to as polar faces, while the vertical lateral faces  $\langle 100 \rangle$ ,  $\langle 101 \rangle$  planes exhibit both cations and anions and are referred to as nonpolar, prismatic faces.<sup>29</sup> Owing to the differences in polarity, the polar faces, exhibit a higher reactivity to precursors (which are mostly ionic in nature) added for further growth of the QD, than the low index apolar faces. Thus, a hexagonal crystal (as also a  $W$  unit cell, Fig. 1.10a) possesses an inherent tendency to promote growth along the  $\langle 002 \rangle$  direction, also referred to as the unique ‘c’ axis. Further, it has been observed, that  $\langle 00\bar{1} \rangle$  and  $\langle 001 \rangle$  differ in the reactivity amongst themselves, based on (a) the nature of ion exposed at the surface (b) number of dangling bonds occurring at the surface. The  $\langle 00\bar{1} \rangle$  face either exposes Se atoms with one dangling bond or Cd atom with three dangling bonds and the  $\langle 001 \rangle$  exposes Se atom with three dangling bonds or Cd atom with one dangling bond.<sup>102,103</sup> Thus, the former is referred to be anion rich face and exhibits higher reactivity than the later, referred to be cation rich in nature. The lateral facets expose both Cd and Se atoms and are thus nonpolar. Further, surface reconstruction in the lateral facets to reduce the number of dangling bonds, minimization of electronic energy and reduction of electrostatic energy by rearranging the charged atoms on the surface results in surface Cd atoms to gain +2 charge and surface Se atoms to gain -2 charge fully, which also makes the lateral facets to be electrically neutral.<sup>4,104,105</sup> Thus in general kinetic growth rates of the planes vary in the order,

$k_{\langle 00\bar{1} \rangle} > k_{\langle 001 \rangle} \gg k_{\langle 101 \rangle} \geq k_{\langle 110 \rangle} \approx k_{\langle 100 \rangle}$ .<sup>106</sup> Figure 1.10 shows the pictorial representation of the 3D structure of a typical *W* CdSe crystal, with the facets shown is actually observed in HRTEM.<sup>102</sup>

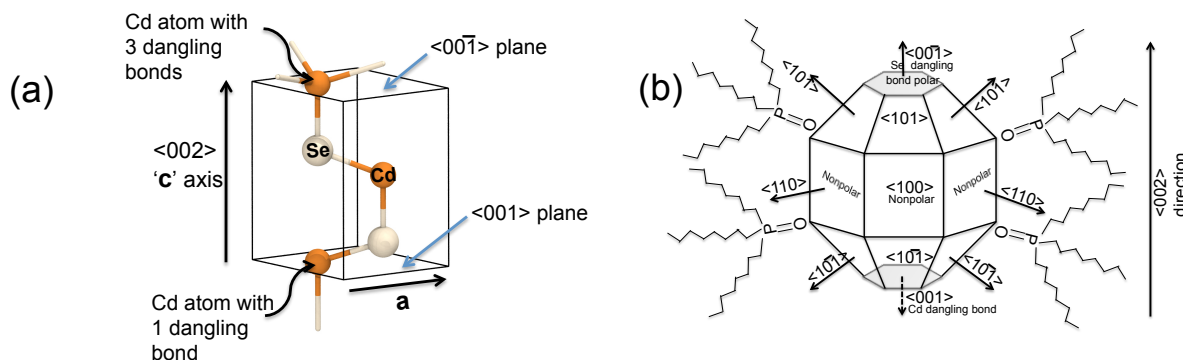


**Figure 1.10:** (a) A typical *W*-CdSe unit cell, with lattice parameters *a*, *c* and differing number of dangling bonds along  $\langle 002 \rangle$  axis shown, (b) A pictorial representation of the 3D structure of a typical *W* CdSe crystal with the facets, as observed in HRTEM.  $\langle 00\bar{1} \rangle$  and  $\langle 001 \rangle$  are the polar facets, which exhibits higher reactivity than the nonpolar  $\langle 100 \rangle$ ,  $\langle 110 \rangle$ , and  $\langle 10\bar{1} \rangle$  facets. Adapted from Ref 102.

### 1.1.5.2 Effect of ligands

The inherent anisotropy of a *W* crystal is further exploited during synthetic procedure, by the use of ligands, which coordinate with the surface atoms in a selective fashion. Ideally in a ligand passivated QD crystal, desorption of the ligand from a particular site is necessary, for the addition of monomer to that site during crystal growth.<sup>107,108</sup> Thus, when the ligands are tightly bound to a particular facet, it impedes growth in that region. It has been observed that ligands like primary amines,<sup>101,109,110</sup> phosphonic acids,<sup>32,103,111</sup> carboxylic acids,<sup>32,101</sup> thiols<sup>24,112,113</sup> essentially coordinate to surface cations, being Lewis bases. In such cases of preferential coordination, the cation rich (cation constituted) facets, (cation constituted) in nature (Figure 1.10b), tend to be passivated more than the anion rich faces, which are left bare. Hence during synthesis,

monomer addition occurs in the unpassivated surfaces more readily, resulting in preferential growth in those directions as observed in the case of syntheses resulting in anisotropic growth patterns, e.g. nanorods,<sup>16,19,20,73,79,108,114,115</sup> arrow, tear drop and tree shaped,<sup>15,116</sup> platelet shaped,<sup>108,110</sup> cube shaped,<sup>108,117</sup> octapod<sup>83</sup> and tetrapod<sup>20,109,118,119</sup> shaped nanocrystals. Bulkier capping agents like TOPO, TOP are unable to passivate the surface as effectively, and result in aspherical and elongated quantum dots with low aspect ratio.<sup>120</sup>

### **1.1.5.3 Kinetic and thermodynamic effects**

Shape evolution in a quantum dot essentially depends on both kinetic and thermodynamic parameters. A thermodynamic regime dictates a nanocrystal shape where the total surface energy is minimized, which results in the formation of spheroidal nanocrystals (least surface area). The thermodynamic equilibrium morphology of a nanocrystal can be determined from by from Wulff construction,<sup>121</sup> which takes into account the surface energy of the growing facets. It is reasonable to assume that during quantum dot growth process, the high-energy facets disappear rapidly while the lower energy stabler facets become progressively more prominent.<sup>29,108</sup> In an ideal world, crystals growing in perfectly isotropic conditions, in absence of any impurity, should have shapes based on relative surface energy of facets. However, in synthetic reactions, conditions are far from being ideal, and with the presence of selectively adhering ligands, surface energy of facets can be radically altered,<sup>122</sup> and thus non-equilibrium kinetic effects play a pivotal role in morphological evolution of a quantum dot. This kinetic regime, induced by using ligands or high monomer concentrations during a synthetic procedure, often results in formation of anisotropic shapes of nanocrystals.<sup>16,79</sup> Further,

the ligands employed during synthesis are found exhibit disparate crystal structure preferences: syntheses involving phosphonic acids, TOPO, TOP, results in the formation primarily anisotropic *W* structures like nanorods, octapods, tetrapods, arrow shapes,<sup>20,116,119</sup> syntheses involving oleic acid results in primarily *ZB* crystal structure<sup>87,88,123,124</sup>, primary amine like oleylamine are observed to promote *W* growth in nanoparticles,<sup>88</sup> while alkyl thiols are observed to promote *ZB* crystal structure<sup>62,125</sup>. The shape of the nanoparticle is expected to be strongly affected by the crystal structure preferences of the ligands involved in the synthesis. Size variation broadly affects the bandgap structure in a QD, but shape variation is expected to affect subtle changes, like polarization, modification of fine structures, and overall shape and symmetry of orbitals.<sup>3,81,126</sup> The growth habit of the semiconductor crystal structure e.g. wurtzite and zinc blende for binary semiconductors like CdSe, CdS has also been found to vastly affect the shape (isotropic or anisotropic growth), exciton structure and hence the band edge luminescence in qdots.<sup>127–131</sup>

### 1.1.6 Polytypism in QDs

As described in Section 1.1.3, II-VI semiconductors like CdSe, CdS, ZnS, CdTe etc, and are known to crystalize in either cubic zinc blende (*ZB*) or metastable hexagonal wurtzite (*W*) forms.<sup>51</sup> The *ZB* and *W* structures are very similar, and vary only in layer stacking along the  $\langle 111 \rangle$  direction (ABC sequence) in *ZB*, and  $\langle 002 \rangle$  direction (ABAB sequence) in *W*. Because of this similarity, interconversion between *ZB* and *W* structures is probable, owing in large part to a low internal energy barrier ( $\leq 20$  meV/atom;  $7.7 \times 10^{-5}$  cal/atom<sup>22</sup>).<sup>88,132</sup> This phenomenon, in which coexistence of both *W* and *ZB* domains are observed in the same crystal, is termed as polytypism.<sup>55</sup> This effect is even more



prominent for QDs where varied synthetic temperatures and ligand environments and high surface energies further facilitate interconversion of the two forms. This effect may have profound effects in terms of the qdots photophysical properties, like quantum yields, lifetimes, blinking, and charge transfer rates.

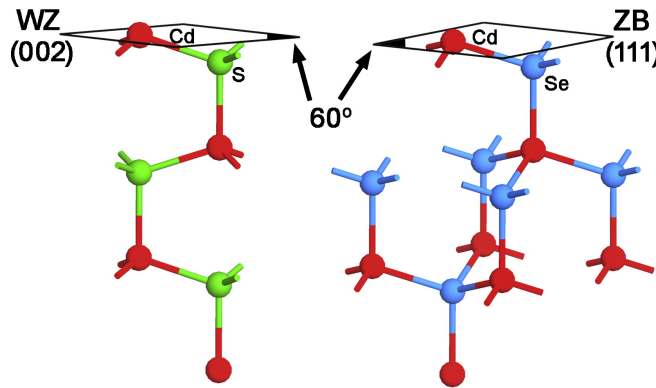


**Figure 1.11:** Showing the interfacial coherence of  $\langle 002 \rangle$  facet of CdS arms and  $\langle 111 \rangle$  facet of CdSe core in CdSe/ CdS tetrapods, Adapted from Ref.132

Polytypism has been observed in the growth of CdSe/CdS tetrapods; where each CdS arm of *W* type are found to grow out of the  $\langle 111 \rangle$  planes of a *ZB* CdSe core.<sup>20,51,123,133,134</sup> In addition, since the ABC stacking direction of  $\langle 111 \rangle$  in *ZB* coincides with the AB stacking direction of  $\langle 002 \rangle$  in *W*, certain complex defects in the stacking sequence (ABABCACA, ABABCBC) may result, due to such overlap, reported in case of CdSe nanorods.<sup>133</sup>

### 1.1.7 Research consideration

The different aspects of QDs like crystal structure, morphology, synthetic methodologies, shape evolution etc. that I have discussed in the previous sections are deeply relevant to the work I present in the next chapters. I have synthesized QDs using the different synthetic procedures mentioned in the previous sections. In chapter 2, I

discuss the synthesis of giant quantum dots starting from *W* and *ZB* core, each of which was prepared by the ‘hot injection’ technique. The purpose of the study was to investigate the role of core crystallinity on the shell growth process of gQDs. Further for the growth of gQDs I have extensively used the layer-by-layer SILAR process to grow multishell on the CdSe cores. I had characterized the photophysical properties of the gQDs by UV-vis and PL spectroscopy, the crystallographic nature employing X-Ray diffraction and the morphological evolution by TEM and HRTEM technique. The study revealed for both (*W* and *ZB*) CdSe core, the reaction proceeds via *W*- crystal structure. Further, the unique occurrence of polytypism was observed during shell growth on both of the cores, which affected the photophysical property of the gQDs to a great extent. In chapter 3, I investigate the role of shell precursor monomer concentration and the source of sulfur precursors in affecting the photophysical, morphological and crystallographic evolution of gQDs starting from identical *W* cores. The study shows that for slow precursor infusion of shell precursors, novel rod shaped gQDs were formed, while for high precursor infusion the innate crystal structure preference of CdZnS and the delicate interplay of the ligands involved result in a varied morphology and crystal structure of gQDs in each syntheses.

### 1.1.8 References

- (1) Alivisatos, A. P. *Science* **1996**, *271* (5251), 933–937.
- (2) Weller, H. *Angew. Chem. Int. Ed. Engl.* **1993**, *32* (1), 41–53.
- (3) Nirmal, M.; Brus, L. *Acc. Chem. Res.* **1999**, *32* (5), 407–414.
- (4) Donegá, C. de M. *Chem. Soc. Rev.* **2011**, *40* (3), 1512–1546.

- (5) Burda, C.; Chen, X.; Narayanan, R.; El-Sayed, M. A. *Chem. Rev.* **2005**, *105* (4), 1025–1102.
- (6) Katz, E.; Willner, I. *Angew. Chem. Int. Ed.* **2004**, *43* (45), 6042–6108.
- (7) Ekimov, A. I.; Efros, A. L.; Onushchenko, A. A. *Solid State Commun.* **1985**, *56* (11), 921–924.
- (8) Green, M. In *RSC Nanoscience & Nanotechnology*; Royal Society of Chemistry: Cambridge, 2014; pp 1–52.
- (9) Rossetti, R.; Brus, L. *J. Phys. Chem.* **1982**, *86* (23), 4470–4472.
- (10) Steigerwald, M. L.; Alivisatos, A. P.; Gibson, J. M.; Harris, T. D.; Kortan, R.; Muller, A. J.; Thayer, A. M.; Duncan, T. M.; Douglass, D. C.; Brus, L. E. *J. Am. Chem. Soc.* **1988**, *110* (10), 3046–3050.
- (11) Murray, C. B.; Norris, D. J.; Bawendi, M. G. *J. Am. Chem. Soc.* **1993**, *115* (19), 8706–8715.
- (12) Dabbousi, B. O.; Rodriguez-Viejo, J.; Mikulec, F. V.; Heine, J. R.; Mattoussi, H.; Ober, R.; Jensen, K. F.; Bawendi, M. G. *J. Phys. Chem. B* **1997**, *101* (46), 9463–9475.
- (13) Hines, M. A.; Guyot-Sionnest, P. *J. Phys. Chem.* **1996**, *100* (2), 468–471.
- (14) Peng, X.; Schlamp, M. C.; Kadavanich, A. V.; Alivisatos, A. P. *J. Am. Chem. Soc.* **1997**, *119* (30), 7019–7029.
- (15) Manna, L.; Scher, E. C.; Alivisatos, A. P. *J. Am. Chem. Soc.* **2000**, *122* (51), 12700–12706.
- (16) Peng, Z. A.; Peng, X. *J. Am. Chem. Soc.* **2001**, *123* (7), 1389–1395.

- (17) Talapin, D. V.; Rogach, A. L.; Kornowski, A.; Haase, M.; Weller, H. *Nano Lett.* **2001**, *1* (4), 207–211.
- (18) Jasieniak, J.; Bullen, C.; van Embden, J.; Mulvaney, P. *J. Phys. Chem. B* **2005**, *109* (44), 20665–20668.
- (19) Carbone, L.; Nobile, C.; De Giorgi, M.; Sala, F. D.; Morello, G.; Pompa, P.; Hytch, M.; Snoeck, E.; Fiore, A.; Franchini, I. R.; Nadasan, M.; Silvestre, A. F.; Chiodo, L.; Kudera, S.; Cingolani, R.; Krahne, R.; Manna, L. *Nano Lett.* **2007**, *7* (10), 2942–2950.
- (20) Talapin, D. V.; Nelson, J. H.; Shevchenko, E. V.; Aloni, S.; Sadtler, B.; Alivisatos, A. P. *Nano Lett.* **2007**, *7* (10), 2951–2959.
- (21) Chen, O.; Zhao, J.; Chauhan, V. P.; Cui, J.; Wong, C.; Harris, D. K.; Wei, H.; Han, H.-S.; Fukumura, D.; Jain, R. K.; Bawendi, M. G. *Nat. Mater.* **2013**, *12* (5), 445–451.
- (22) Steckel, J. S.; Zimmer, J. P.; Coe-Sullivan, S.; Stott, N. E.; Bulović, V.; Bawendi, M. G. *Angew. Chem. Int. Ed.* **2004**, *43* (16), 2154–2158.
- (23) Green, M. *J. Mater. Chem.* **2010**, *20* (28), 5797–5809.
- (24) Medintz, I. L.; Uyeda, H. T.; Goldman, E. R.; Mattoussi, H. *Nat. Mater.* **2005**, *4* (6), 435–446.
- (25) Han, H.; Zylstra, J.; Maye, M. M. *Chem. Mater.* **2011**, *23* (22), 4975–4981.
- (26) Zylstra, J.; Amey, J.; Miska, N. J.; Pang, L.; Hine, C. R.; Langer, J.; Doyle, R. P.; Maye, M. M. *Langmuir* **2011**, *27* (8), 4371–4379.
- (27) Cooper, J. K.; Franco, A. M.; Gul, S.; Corrado, C.; Zhang, J. Z. *Langmuir* **2011**, *27* (13), 8486–8493.

- (28) Yu, W. W.; Qu, L.; Guo, W.; Peng, X. *Chem. Mater.* **2003**, *15* (14), 2854–2860.
- (29) Bertoni, G.; Grillo, V.; Brescia, R.; Ke, X.; Bals, S.; Catellani, A.; Li, H.; Manna, L. *ACS Nano* **2012**, *6* (7), 6453–6461.
- (30) Liu, H.; Owen, J. S.; Alivisatos, A. P. *J. Am. Chem. Soc.* **2007**, *129* (2), 305–312.
- (31) Kunneman, L. T.; Zanella, M.; Manna, L.; Siebbeles, L. D. A.; Schins, J. M. *J. Phys. Chem. C* **2013**, *117* (6), 3146–3151.
- (32) Gomes, R.; Hassinen, A.; Szczygiel, A.; Zhao, Q.; Vantomme, A.; Martins, J. C.; Hens, Z. *J. Phys. Chem. Lett.* **2011**, *2* (3), 145–152.
- (33) Ebenstein, Y.; Nahum, E.; Banin, U. *Nano Lett.* **2002**, *2* (9), 945–950.
- (34) Steiner, D.; Dorfs, D.; Banin, U.; Della Sala, F.; Manna, L.; Millo, O. *Nano Lett.* **2008**, *8* (9), 2954–2958.
- (35) Sitt, A.; Sala, F. D.; Menagen, G.; Banin, U. *Nano Lett.* **2009**, *9* (10), 3470–3476.
- (36) Choi, C. L.; Li, H.; Olson, A. C. K.; Jain, P. K.; Sivasankar, S.; Alivisatos, A. P. *Nano Lett.* **2011**, *11* (6), 2358–2362.
- (37) Rainò, G.; Stöferle, T.; Moreels, I.; Gomes, R.; Hens, Z.; Mahrt, R. F. *ACS Nano* **2012**, *6* (3), 1979–1987.
- (38) Hadar, I.; Hitin, G. B.; Sitt, A.; Faust, A.; Banin, U. *J. Phys. Chem. Lett.* **2013**, *4* (3), 502–507.
- (39) Alam, R.; Fontaine, D. M.; Branchini, B. R.; Maye, M. M. *Nano Lett.* **2012**, *12* (6), 3251–3256.
- (40) Alam, R.; Zylstra, J.; Fontaine, D. M.; Branchini, B. R.; Maye, M. M. *Nanoscale* **2013**, *5* (12), 5303–5306.

- (41) Alam, R.; Karam, L. M.; Doane, T. L.; Zylstra, J.; Fontaine, D. M.; Branchini, B. R.; Maye, M. M. *Nanotechnology* **2014**, 25 (49), 495606.
- (42) Klimov, V. I.; Ivanov, S. A.; Nanda, J.; Achermann, M.; Bezel, I.; McGuire, J. A.; Piryatinski, A. *Nature* **2007**, 447 (7143), 441–446.
- (43) García-Santamaría, F.; Chen, Y.; Vela, J.; Schaller, R. D.; Hollingsworth, J. A.; Klimov, V. I. *Nano Lett.* **2009**, 9 (10), 3482–3488.
- (44) Zavelani-Rossi, M.; Lupo, M. G.; Krahne, R.; Manna, L.; Lanzani, G. *Nanoscale* **2010**, 2 (6), 931–935.
- (45) Kazes, M.; Lewis, D. y.; Ebenstein, Y.; Mokari, T.; Banin, U. *Adv. Mater.* **2002**, 14 (4), 317–321.
- (46) Anikeeva, P. O.; Halpert, J. E.; Bawendi, M. G.; Bulović, V. *Nano Lett.* **2009**, 9 (7), 2532–2536.
- (47) Zhao, J.; Bardecker, J. A.; Munro, A. M.; Liu, M. S.; Niu, Y.; Ding, I.-K.; Luo, J.; Chen, B.; Jen, A. K.-Y.; Ginger, D. S. *Nano Lett.* **2006**, 6 (3), 463–467.
- (48) Alivisatos, P. *Nat. Biotechnol.* **2004**, 22 (1), 47–52.
- (49) Hahn, M. A.; Tabb, J. S.; Krauss, T. D. *Anal. Chem.* **2005**, 77 (15), 4861–4869.
- (50) Ruan, G.; Agrawal, A.; Marcus, A. I.; Nie, S. *J. Am. Chem. Soc.* **2007**, 129 (47), 14759–14766.
- (51) Rogach, A. L. *Semiconductor nanocrystal quantum dots: synthesis, assembly, spectroscopy and applications*; Springer: Wien; New York; [London], 2008.
- (52) Rossetti, R.; Ellison, J. L.; Gibson, J. M.; Brus, L. E. *J. Chem. Phys.* **1984**, 80 (9), 4464–4469.
- (53) Roduner, E. In *Electronic Structure*; 2006.

- (54) Lakowicz, J. R. *Principles of fluorescence spectroscopy*, 3rd ed.; Springer: New York, 2006.
- (55) West, A. R. *Basic solid state chemistry*, 2nd ed.; John Wiley & Sons: New York, 1999.
- (56) Gaponenko, S. V. *Optical properties of semiconductor nanocrystals*, Digitally printed 1st pbk. version.; Cambridge studies in modern optics; Cambridge University Press: Cambridge ; New York, 2005.
- (57) Colvin, V. L.; Goldstein, A. N.; Alivisatos, A. P. *J. Am. Chem. Soc.* **1992**, *114* (13), 5221–5230.
- (58) Zhuang, Z.; Peng, Q.; Li, Y. *Chem. Soc. Rev.* **2011**, *40* (11), 5492–5513.
- (59) LaMer, V. K.; Dinegar, R. H. *J. Am. Chem. Soc.* **1950**, *72* (11), 4847–4854.
- (60) Hines, M. A.; Guyot-Sionnest, P. *J. Phys. Chem. B* **1998**, *102* (19), 3655–3657.
- (61) Li, L. S.; Pradhan, N.; Wang, Y.; Peng, X. *Nano Lett.* **2004**, *4* (11), 2261–2264.
- (62) Bose, R.; Manna, G.; Pradhan, N. *J. Phys. Chem. C* **2013**, *117* (36), 18762–18767.
- (63) Norris, D. J.; Yao, N.; Charnock, F. T.; Kennedy, T. A. *Nano Lett.* **2001**, *1* (1), 3–7.
- (64) Hines, M. a.; Scholes, G. d. *Adv. Mater.* **2003**, *15* (21), 1844–1849.
- (65) Lu, W.; Fang, J.; Stokes, K. L.; Lin, J. *J. Am. Chem. Soc.* **2004**, *126* (38), 11798–11799.
- (66) Urban, J. J.; Talapin, D. V.; Shevchenko, E. V.; Murray, C. B. *J. Am. Chem. Soc.* **2006**, *128* (10), 3248–3255.
- (67) Pietryga, J. M.; Schaller, R. D.; Werder, D.; Stewart, M. H.; Klimov, V. I.; Hollingsworth, J. A. *J. Am. Chem. Soc.* **2004**, *126* (38), 11752–11753.

- (68) Lipovskii, A.; Kolobkova, E.; Petrikov, V.; Kang, I.; Olkhovets, A.; Krauss, T.; Thomas, M.; Silcox, J.; Wise, F.; Shen, Q.; Kycia, S. *Appl. Phys. Lett.* **1997**, *71* (23), 3406–3408.
- (69) Battaglia, D.; Peng, X. *Nano Lett.* **2002**, *2* (9), 1027–1030.
- (70) Cao, Y.-W.; Banin, U. *Angew. Chem. Int. Ed.* **1999**, *38* (24), 3692–3694.
- (71) Micic, O. I.; Curtis, C. J.; Jones, K. M.; Sprague, J. R.; Nozik, A. J. *J. Phys. Chem.* **1994**, *98* (19), 4966–4969.
- (72) Peng, X.; Manna, L.; Yang, W.; Wickham, J.; Scher, E.; Kadavanich, A.; Alivisatos, A. P. *Nature* **2000**, *404* (6773), 59–61.
- (73) Peng, Z. A.; Peng, X. *J. Am. Chem. Soc.* **2002**, *124* (13), 3343–3353.
- (74) Qu, L.; Peng, X. *J. Am. Chem. Soc.* **2002**, *124* (9), 2049–2055.
- (75) Li, J. J.; Wang, Y. A.; Guo, W.; Keay, J. C.; Mishima, T. D.; Johnson, M. B.; Peng, X. *J. Am. Chem. Soc.* **2003**, *125* (41), 12567–12575.
- (76) Yu, W. W.; Peng, X. *Angew. Chem. Int. Ed.* **2002**, *41* (13), 2368–2371.
- (77) Jeong, S.; Achermann, M.; Nanda, J.; Ivanov, S.; Klimov, V. I.; Hollingsworth, J. A. *J. Am. Chem. Soc.* **2005**, *127* (29), 10126–10127.
- (78) Chen, Y.; Vela, J.; Htoon, H.; Casson, J. L.; Werder, D. J.; Bussian, D. A.; Klimov, V. I.; Hollingsworth, J. A. *J. Am. Chem. Soc.* **2008**, *130* (15), 5026–5027.
- (79) Peng, X. *Adv. Mater.* **2003**, *15* (5), 459–463.
- (80) Manna, L.; Scher, E. C.; Li, L.-S.; Alivisatos, A. P. *J. Am. Chem. Soc.* **2002**, *124* (24), 7136–7145.
- (81) Borys, N. J.; Walter, M. J.; Huang, J.; Talapin, D. V.; Lupton, J. M. *Science* **2010**, *330* (6009), 1371–1374.



- (82) Fiore, A.; Mastria, R.; Lupo, M. G.; Lanzani, G.; Giannini, C.; Carlino, E.; Morello, G.; De Giorgi, M.; Li, Y.; Cingolani, R.; Manna, L. *J. Am. Chem. Soc.* **2009**, *131* (6), 2274–2282.
- (83) Deka, S.; Miszta, K.; Dorfs, D.; Genovese, A.; Bertoni, G.; Manna, L. *Nano Lett.* **2010**, *10* (9), 3770–3776.
- (84) Herman, M. A.; Sitter, H. *Molecular Beam Epitaxy Fundamentals and Current Status*; Springer Berlin Heidelberg: Berlin, Heidelberg, 1996.
- (85) Xu, Z.; Hine, C. R.; Maye, M. M.; Meng, Q.; Cotlet, M. *ACS Nano* **2012**, *6* (6), 4984–4992.
- (86) Guo, Y.; Marchuk, K.; Sampat, S.; Abraham, R.; Fang, N.; Malko, A. V.; Vela, J. *J. Phys. Chem. C* **2012**, *116* (4), 2791–2800.
- (87) Majumder, S.; Bae, I.-T.; Maye, M. M. *J. Mater. Chem. C* **2014**, *2* (23), 4659–4666.
- (88) Mahler, B.; Lequeux, N.; Dubertret, B. *J. Am. Chem. Soc.* **2010**, *132* (3), 953–959.
- (89) Bleuse, J.; Carayon, S.; Reiss, P. *Phys. E Low-Dimens. Syst. Nanostructures* **2004**, *21* (2–4), 331–335.
- (90) Reiss, P.; Carayon, S.; Bleuse, J.; Pron, A. *Synth. Met.* **2003**, *139* (3), 649–652.
- (91) Krauss, T. D.; Peterson, J. J. *Nat. Mater.* **2012**, *11* (1), 14–16.
- (92) Hollingsworth, J. A. *Chem. Mater.* **2013**, *25* (8), 1318–1331.
- (93) Mahler, B.; Spinicelli, P.; Buil, S.; Quelin, X.; Hermier, J.-P.; Dubertret, B. *Nat. Mater.* **2008**, *7* (8), 659–664.
- (94) Hohng, S.; Ha, T. *J. Am. Chem. Soc.* **2004**, *126* (5), 1324–1325.
- (95) Fomenko, V.; Nesbitt, D. J. *Nano Lett.* **2008**, *8* (1), 287–293.

- (96) Hammer, N. I.; Early, K. T.; Sill, K.; Odoi, M. Y.; Emrick, T.; Barnes, M. D. *J. Phys. Chem. B* **2006**, *110* (29), 14167–14171.
- (97) Wang, X.; Ren, X.; Kahen, K.; Hahn, M. A.; Rajeswaran, M.; Maccagnano-Zacher, S.; Silcox, J.; Cragg, G. E.; Efros, A. L.; Krauss, T. D. *Nature* **2009**, *459* (7247), 686–689.
- (98) Htoon, H.; Malko, A. V.; Bussian, D.; Vela, J.; Chen, Y.; Hollingsworth, J. A.; Klimov, V. I. *Nano Lett.* **2010**, *10* (7), 2401–2407.
- (99) Kundu, J.; Ghosh, Y.; Dennis, A. M.; Htoon, H.; Hollingsworth, J. A. *Nano Lett.* **2012**, *12* (6), 3031–3037.
- (100) Park, Y.-S.; Malko, A. V.; Vela, J.; Chen, Y.; Ghosh, Y.; García-Santamaría, F.; Hollingsworth, J. A.; Klimov, V. I.; Htoon, H. *Phys. Rev. Lett.* **2011**, *106* (18), 187401.
- (101) Ghosh, Y.; Mangum, B. D.; Casson, J. L.; Williams, D. J.; Htoon, H.; Hollingsworth, J. A. *J. Am. Chem. Soc.* **2012**, *134* (23), 9634–9643.
- (102) Rosenthal, S. J.; McBride, J.; Pennycook, S. J.; Feldman, L. C. *Surf. Sci. Rep.* **2007**, *62* (4), 111–157.
- (103) Manna, L.; Wang; Cingolani, R.; Alivisatos, A. P. *J. Phys. Chem. B* **2005**, *109* (13), 6183–6192.
- (104) Rempel, J. Y.; Trout, B. L.; Bawendi, M. G.; Jensen, K. F. *J. Phys. Chem. B* **2005**, *109* (41), 19320–19328.
- (105) Rempel, J. Y.; Trout, B. L.; Bawendi, M. G.; Jensen, K. F. *J. Phys. Chem. B* **2006**, *110* (36), 18007–18016.
- (106) Li, W.; Shi, E.; Chen, Z.; Yin, Z. *Chin. Sci. Bull.* **2000**, *45* (18), 1662–1666.

- (107) Nair, P. S.; Fritz, K. P.; Scholes, G. D. *Small* **2007**, 3 (3), 481–487.
- (108) Rice, K. P.; Saunders, A. E.; Stoykovich, M. P. *J. Am. Chem. Soc.* **2013**, 135 (17), 6669–6676.
- (109) Yong, K.-T.; Sahoo, Y.; Swihart, M. T.; Prasad, P. N. *J. Phys. Chem. C* **2007**, 111 (6), 2447–2458.
- (110) Chauhan, H.; Kumar, Y.; Deka, S. *Nanoscale* **2014**, 6 (17), 10347–10354.
- (111) Puzder, A.; Williamson, A. J.; Zaitseva, N.; Galli, G.; Manna, L.; Alivisatos, A. P. *Nano Lett.* **2004**, 4 (12), 2361–2365.
- (112) Pong, B.-K.; Trout, B. L.; Lee, J.-Y. *Langmuir* **2008**, 24 (10), 5270–5276.
- (113) Billone, P. S.; Maretti, L.; Maurel, V.; Scaiano, J. C. *J. Am. Chem. Soc.* **2007**, 129 (46), 14150–14151.
- (114) Jun, Y.; Lee, S.-M.; Kang, N.-J.; Cheon, J. *J. Am. Chem. Soc.* **2001**, 123 (21), 5150–5151.
- (115) Li, N.; Zhang, X.; Chen, S.; Hou, X.; Liu, Y.; Zhai, X. *Mater. Sci. Eng. B* **2011**, 176 (8), 688–691.
- (116) Manna, L.; Scher, E. C.; Alivisatos, A. P. *J. Clust. Sci.* **2002**, 13 (4), 521–532.
- (117) Zhai, X.; Zhang, X.; Chen, S.; Yang, W.; Gong, Z. *Colloids Surf. Physicochem. Eng. Asp.* **2012**, 409, 126–129.
- (118) Manna, L.; Milliron, D. J.; Meisel, A.; Scher, E. C.; Alivisatos, A. P. *Nat. Mater.* **2003**, 2 (6), 382–385.
- (119) Milliron, D. J.; Hughes, S. M.; Cui, Y.; Manna, L.; Li, J.; Wang, L.-W.; Paul Alivisatos, A. *Nature* **2004**, 430 (6996), 190–195.
- (120) Wang, F.; Tang, R.; Buhro, W. E. *Nano Lett.* **2008**, 8 (10), 3521–3524.

- (121) Lacmann, R. *Chem. Ing. Tech.* **1998**, 70 (11), 1468–1468.
- (122) Jun, Y.; Casula, M. F.; Sim, J.-H.; Kim, S. Y.; Cheon, J.; Alivisatos, A. P. *J. Am. Chem. Soc.* **2003**, 125 (51), 15981–15985.
- (123) Mishra, N.; Lian, J.; Chakraborty, S.; Lin, M.; Chan, Y. *Chem. Mater.* **2012**, 24 (11), 2040–2046.
- (124) Bao, Y.; An, W.; Turner, C. H.; Krishnan, K. M. *Langmuir* **2010**, 26 (1), 478–483.
- (125) Jun, S.; Jang, E.; Chung, Y. *Nanotechnology* **2006**, 17 (19), 4806–4810.
- (126) Kim, J.; Nair, P. S.; Wong, C. Y.; Scholes, G. D. *Nano Lett.* **2007**, 7 (12), 3884–3890.
- (127) Li, J.; Wang. *Nano Lett.* **2003**, 3 (10), 1357–1363.
- (128) Murayama, M.; Nakayama, T. *Phys. Rev. B* **1994**, 49 (7), 4710–4724.
- (129) Brovelli, S.; Bae, W. K.; Meinardi, F.; Santiago González, B.; Lorenzon, M.; Galland, C.; Klimov, V. I. *Nano Lett.* **2014**, 14 (7), 3855–3863.
- (130) Lo, S. S.; Mirkovic, T.; Chuang, C.-H.; Burda, C.; Scholes, G. D. *Adv. Mater.* **2011**, 23 (2), 180–197.
- (131) Bandić, Z. Z.; Ikonić, Z. *Phys. Rev. B* **1995**, 51 (15), 9806–9812.
- (132) Xia, X.; Liu, Z.; Du, G.; Li, Y.; Ma, M. *J. Lumin.* **2010**, 130 (7), 1285–1291.
- (133) Hughes, S. M.; Alivisatos, A. P. *Nano Lett.* **2013**, 13 (1), 106–110.
- (134) Akiyama, T.; Nakamura, K.; Ito, T. *Phys. Rev. B* **2006**, 73 (23), 235308.

## Chapter 2

### ***Investigating the Role of Polytypism in the Growth of Multi-Shell CdSe/CdZnS Quantum Dots***

In this work I investigate the role that polytypism has on the growth of multi-shelled, giant quantum dots (gQDs). Multi-shell growth was initiated at CdSe cores with either Zinc blende or Wurtzite crystal structures. The shells consisted of a  $\text{Cd}_x\text{Zn}_{1-x}\text{S}$  gradient that was deposited in a slow layer-by-layer SILAR process. The final gQDs had sizes of  $>15\text{nm}$ , with shapes and symmetry that were influenced by core type, and polytypic growth conditions. A study of morphology and crystal structure change at each stage of shell growth was carried out by powder XRD, TEM, and HRTEM, and the photophysical properties were studied by UV-Vis and fluorescence spectroscopy. In both types of cores, shell growth was found to transition to Wurtzite, whereas the percentage of polytypism was shown to alter both morphology and optical properties. This work is reproduced with permission from *J. Mater. Chem. C*, **2014**, 2 (23), 4659–4666. Copyright Royal Society of Chemistry.

#### **2.1 Introduction**

Quantum dots (QDs) are semiconductive nanoparticles with diameters that range from 1–10 nm that also exhibit optoelectronic properties that derive from quantum confinement effects.<sup>1,2,3</sup> In addition to size, properties are tailored by composition, morphology, and microstructure changes. Such flexibility has led to applications in biolabeling and biotechnology,<sup>4–7</sup> biomimetic energy transfer,<sup>8,9</sup> light-emitting diodes (LEDs),<sup>10,11</sup> as well as solar cells and lasers.<sup>12–15</sup> The II-VI chalcogenides can crystallize in either cubic Zinc

Blende (*ZB*) or metastable hexagonal Wurtzite (*W*) forms.<sup>16</sup> The *ZB* and *W* structures are very similar, and vary only in layer stacking along the  $\langle 111 \rangle$  direction (ABC sequence) in *ZB*, and  $\langle 002 \rangle$  direction (ABAB sequence) in *W*. Because of this similarity, interconversion between *ZB* and *W* structures is possible, owing in large part to a low internal energy barrier  $\leq 20$  meV/atom.<sup>17,18</sup> This effect is even more prominent for the nanoscale QD, where varied synthetic temperatures and ligand environments, as well as high surface energies, may lead to an ease of interconversion as observed in some recent studies.<sup>19</sup>

This can lead to polytypism, where a single particle may possess both *W* and *ZB* domains. This effect would influence photophysical properties, like quantum yields, lifetimes, blinking, and charge transfer rates. In addition to CdSe core growth, another synthetic event that may lead to polytypism is that of shell growth with CdS or ZnS.<sup>20–22</sup> The lattice mismatch between the core (i.e. CdSe), and shell (i.e. CdS, ZnS), as well as the change in band gap energies, can also lead to defect rich domains. For instance, the internal energy difference between *ZB* and *W* phases for CdS is  $\sim 1.1$  meV/atom,<sup>23,24</sup> making polytypism in the shell even more probable. Examples of core-shell QDs with two entirely different crystal structures have been shown before in the growth of CdSe/ZnS tetrapods, where *W*-CdS legs are grown at highly faceted *ZB*-CdSe cores.<sup>25,26,27</sup> Such anisotropic growth is known to occur along the  $\langle 0001 \rangle$  the direction of the *W*-shell.<sup>28–30</sup> In addition, the observation of *W*-shells at *ZB*-cores has been investigated at the HRTEM and XRD level previously.<sup>17,18</sup>

Recently it has been shown that QDs that possess thick inorganic shells can better isolate the exciton from the surface interface, which decreases hole or electron trapping.<sup>34</sup> These

giant quantum dots (gQDs), or long asymmetric quantum rods (QRs) result in highly processable materials, with high quantum yields and resistance to photo bleaching, as well as reduced ‘blinking’ tendencies.<sup>15,31,32,34</sup> Recently it was shown that ligand choice can determine crystalline evolution of gQDs, and that polytypic growth can affect the dots band structure and photophysics.<sup>17,33</sup> While there is a growing wealth of knowledge about the photophysical characteristics of these multi-shelled gQDs,<sup>15,34</sup> less is known about the crystalline evolution of these materials during giant shell growth.

To address this, I investigate the crystalline changes during growth of  $\text{Cd}_x\text{Zn}_{1-x}\text{S}$  gradient shells on CdSe QD cores. Powder X-ray diffraction (XRD) was used to observe crystal structure change during shell growth, in which a significant polytypism was observed. The role of the core QD crystal type on shell growth and polytypism was also investigated.

## **2.2 Experimental**

### **2.2.1 Chemicals & Materials:**

Cadmium oxide ( $\text{CdO}$ ,  $\geq 99.99\%$ ), dioctylamine (DOA, 95%), dodecylamine (DDA, 98%), sulfur (reagent grade, 100 mesh), selenium powder (Se, reagent grade  $\geq 99.999\%$ ), oleic acid (OAc, 90%), 1-octadecene (ODE 90%), trioctylphosphine oxide (TOPO, 90%), hexadecylamine (HDA, 98%), trioctylphosphine (TOP, 97%) and tributylphosphine (TBP, 97%) were purchased from Aldrich and used without further purification. Zinc oxide ( $\text{ZnO}$ ,  $\geq 99.0\%$ ) and stearic acid (SA, 98%) were purchased from Fluka Analytical and Alfa Aesar respectively and used without purification. Ethanol ( $\text{EtOH}$ ,  $\geq 99.5\%$ ),

chloroform (Cl, 99.8%), Toluene (Tl, 99.8%) and Rhodamine 6G (R6G, 99%) were purchased from Sigma Aldrich.

## **2.2.2 Synthesis**

### **2.2.2.1 Synthesis of *Zinc blende (ZB)* Cores**

The CdSe QD cores with *ZB* crystal structure were synthesized by standard methods.<sup>35–39, 36,38</sup> In a typical synthesis, 0.103g (0.802 mmol) of CdO in 12 mL oleic acid (OAc) and 5.0 mL ODE was heated to 230°C forming a colourless solution of Cd-oleate. Next, 0.021 mol of dodecylamine (DDA) and 2.002g trioctylphosphine oxide (TOPO) was introduced and the mixture heated to 270°C until a colourless solution was obtained. Here, the TOPO was first recrystallized before use. Then, 0.472g (5.978 mmol) of Se dissolved in 1.5 mL of tributylphosphine (TBP) in an air free glovebox and then rapidly injected into the reaction mixture inducing nucleation and growth of CdSe QDs. After one minute, the vessel was removed from the heating mantle and allowed to cool naturally. The resulting *ZB*-CdSe QDs were then purified free of excess ligands by multiple methanol extractions, and finally by precipitation in acetone. The OAc-, TOPO-capped CdSe QDs were re-dispersed in chloroform.

### **2.2.2.2 Synthesis of *Wurtzite (W)* CdSe Cores**

The CdSe cores with *W* crystal structure were prepared by known literature procedure with minor alterations.<sup>39</sup> A typical synthesis involved loading 0.052 g (0.405 mmol) of CdO, 6.0 ml ODE and stearic acid (SA) 0.452 g (1.589 mmol) into a 50 mL flask and degassing the mixture for 1 h at 130°C. Next, the mixture was opened to Ar flow and



heated to 190°C until a colourless solution was formed by complete dissolution of CdO in SA, forming Cd-stearate. The solution was cooled to room temperature, then hexadecylamine (HDA) 3.502g (0.015 mol) and TOPO 3.584 g (0.009mol) were added. The reaction mixture was then heated to 330°C. Next, Se 0.322g (4.078 mmol) dissolved in 2 mL TOP prepared in the glove box was quickly injected into the solution at 330°C and allowed to stand for one minute to induce nucleation and growth of CdSe quantum dots. The temperature was then set at 280°C and let to anneal for 10 min, and then the vessel was removed from the heating mantle and allowed to cool. The resulting *W*-CdSe QDs were then purified, free of excess ligands by multiple methanol extractions, and finally by precipitation in acetone. CdSe core QDs were re-dispersed in chloroform.

### 2.2.2.3 Synthesis of *Multishelled Giant Quantum Dots (gQD)*

The syntheses of gQDs at both *ZB* and *W* CdSe cores were carried out following a modified version of the successive ionic layer adsorption and reaction (SILAR)<sup>40</sup> recently described by Hollingsworth and co-workers.<sup>34</sup> Briefly, a 0.2 M sulfur stock solution was prepared by dissolving sulfur in ODE. Next a 0.2 M Cd-oleate stock solution was prepared by dissolving CdO in OAc as described above, and similarly a 0.2 M Zn-oleate stock was prepared. These Zn-oleate and Cd-oleate solutions were then mixed at varied molar ratios to obtain Cd<sub>x</sub>Zn<sub>1-x</sub>-oleate solutions at three feed ratios, which was denoted as Cd<sub>0.87</sub>Zn<sub>0.13</sub>-oleate, Cd<sub>0.51</sub>Zn<sub>0.49</sub> -oleate and Cd<sub>0.22</sub> Zn<sub>0.78</sub>-oleate. These stock solutions were then used to deposit the cation at multiple shells. In this study, the first six layers of deposition (*n*) consisted of Cd<sub>0.87</sub>Zn<sub>0.13</sub>-oleate (*n* = 1-6), followed by six layers of Cd<sub>0.51</sub>Zn<sub>0.49</sub> -oleate (*n* = 6-12), and finally by six layers of Cd<sub>0.22</sub> Zn<sub>0.78</sub>-oleate (*n* = 12-18).

To prepare the gQDs from *ZB*-CdSe cores, first 0.050 moles of dioctylamine (DOA) and 0.048 moles of ODE were added to a 50 mL flask containing  $6.0 \times 10^{-7}$  mol of dried *ZB*-CdSe cores. The secondary DOA was chosen as a ligand in place of a primary amine as described recently, to prevent the reaction between the Cd-oleate and amine ligands, premature gQD precipitation and core crystal structure alteration.<sup>17,15,34,41,42</sup> The shell deposition temperature was 240°C. For each layer (*n*) of growth, firstly deposition was the anion from S in ODE solution, followed by a calculated amount of Cd<sub>x</sub>Zn<sub>1-x</sub>-oleate solution. The volume of precursors added at each *n* was determined by using the volume increment of each layer, considering both the changing QD size, and the residual QD concentration after sampling aliquots for analysis. Growth times were 0.5 h for anion and 0.5 h for the cation precursors. In this manner, 18 layers of Cd<sub>x</sub>Zn<sub>1-x</sub>S were grown using Cd<sub>0.87</sub>Zn<sub>0.13</sub>-oleate for the *n* = 1-6, Cd<sub>0.51</sub>Zn<sub>0.49</sub>-oleate for *n* = 6-12, and Cd<sub>0.22</sub>Zn<sub>0.78</sub>-oleate for *n* = 12-18. Thus Cd concentration in the alloy shell decreases from the core to the periphery. Following shell growth, these gQDs were precipitated from growth solution by methanol and acetone and dispersed in chloroform. For gQD growth using *W*-CdSe cores, 0.033 moles of DOA and 0.032 moles of ODE was added to a 50 mL flask containing  $3.98 \times 10^{-7}$  mol of the dried *W*-CdSe core QDs. The rest of the growth process was identical to that outlined above for *ZB* gQDs.

#### 2.2.2.4 Control experiments

Control experiments were performed by annealing *W*-CdSe cores (*d* = 3.5 nm) for 2.5 hr at 240 °C in presence of oleic acid (OAc) and dioctylamine (DOA) separately to investigate if the crystallographic preference of the two ligands affect the core structure prior to shell addition. Briefly,  $2.9 \times 10^{-8}$  moles of dried *W* CdSe were added to a 25 mL

four necked flask with ~4 mL OAc (OAc, 0.013 moles) and 5 mL octadecene (ODE). The mixture was degassed at 110 °C for 1 hr, followed by annealing at 240°C under Ar flow. The reaction was probed by sampling out aliquots at regular intervals during the annealing process and subjecting them to UV-vis characterization.

Similar experiments were performed using *ZB*-CdSe cores (diameter  $d = 3.7$  nm). Briefly,  $1.5 \times 10^{-7}$  moles of dried *ZB* CdSe were taken into a 25 ml four-necked flask with 5 mL OAc (0.016 moles) and 5 mL ODE. The mixture was degassed at 110 °C for 1 hr, followed by heating up and annealing at 240°C under Ar flow for 1.5 hr. The reaction progress was monitored in an identical manner mentioned above for *W*- CdSe cores by sampling out aliquots.

### 2.3 Instrumentation

*UV-Visible Spectrophotometry (UV-Vis)*: The UV-vis measurements were collected on a Varian Cary 100 Bio UV-vis spectrophotometer.

*Photoluminescence Spectroscopy (PL)*: The PL emission and excitation measurements were collected on a Fluoromax-4 photon counting spectrofluorometer (Horiba Jobin Yvon). The excitation wavelength was 400 nm.

*Powder X-ray diffraction (XRD)*: XRD was collected using a Bruker AXS D8 ADVANCE powder X-ray diffractometer. To optimize XRD quality and remove artifacts arising from ligand packing and excess ligands, the synthesized gQDs were first

precipitated from chloroform using a ligand exchange protocol that employs L-histidine.<sup>36</sup> The precipitated gQDs, with L-histidine capping in place of DOA and TOPO, were rinsed gently in ultrapure water, and then vacuum dried on a zero diffraction SiO<sub>2</sub> crystal (MTI Corp.).

*Transmission Electron Microscopy (TEM):* TEM measurements were performed on a JEOL 2000EX scope operated at 80 kV. The high resolution TEM (HRTEM) was collected on a JEOL JEM2100F field emission TEM operated at 200 kV at the Analytical and Diagnostics Laboratory at State University of New York at Binghamton.

## 2.4 Calculations

*Concentration:* The QD core concentration were calculated by first approximating QD diameter from the first absorption wavelength using the calibration provided by Peng and co-workers<sup>43</sup> and Mulvaney and co-workers.<sup>44</sup> This diameter was then used to approximate the QD extinction coefficient.<sup>43,44</sup>

## 2.5 Results & Discussion

In this section, I describe the characterization of giant quantum dots (gQDs) synthesized from *ZB*- and *W*-CdSe cores by means of Ultraviolet-visible absorption spectroscopy (UV-vis), emission spectroscopy (PL), powder X-ray diffraction (XRD), transmission electron microscopy (TEM), and high resolution TEM (HRTEM). These cores are then used to perform a systematic study to develop an understanding of the gQD shell growth mechanism. Figure 2.1 shows the UV-vis (a) and normalized PL emission spectra (b) for the *ZB* (i) and *W*-CdSe (ii) cores. As shown in Fig. 2.1a-i, the

*ZB*-CdSe QD core has a first absorption maximum ( $\lambda_{\text{Abs}}$ ) at 575 nm. The diameter ( $d$ ) of *ZB*-cores were estimated from  $\lambda_{\text{Abs}}$  to be  $\sim 3.6$  nm.<sup>41,42</sup> The PL emission is shown in Fig. 2.1b-i, and reveals a sharp PL maxima ( $\lambda_{\text{PL}}$ ) centred at 590 nm with a full width half maxima (FWHM) of 35 nm. The UV-vis spectra of the *W*-CdSe core is shown in Fig. 2.1a-ii, and has a  $\lambda_{\text{Abs}} = 586$  nm, which correlates with an estimated  $d \approx 4.0$  nm. The PL spectra, shows a narrow  $\lambda_{\text{PL}} = 596$  nm, FWHM = 23 nm (Fig. 1b-ii). The narrow PL, and the close proximity of the  $\lambda_{\text{Abs}}$  and  $\lambda_{\text{PL}}$  (narrow Stokes shift), indicates the formation of good quality crystalline QD.<sup>45</sup> In addition, the second absorption at  $\sim 550$  nm for the *W*-CdSe has been shown to be indicative of *W* crystal structure, further suggesting the successful synthesis of this crystal type.<sup>46,47</sup>

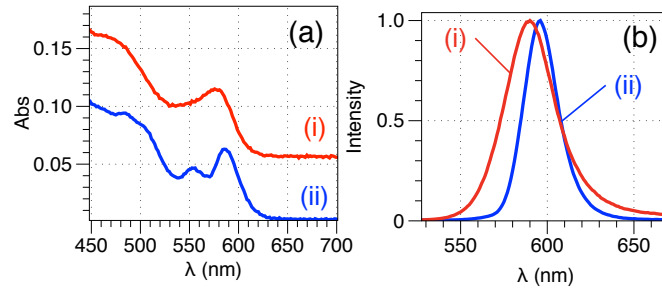


**Figure 2.1:** Representative UV-vis absorption (a) and the normalized PL emission spectra (b) for QD cores with Zinc Blende (*ZB*) (i) and Wurtzite (*W*) (ii) crystallinity.

Figure 2.2 shows the corresponding XRD results for the *ZB* (i) and *W*-CdSe cores (ii). As expected from the synthesis parameters (see methods) and UV-vis results, the CdSe synthesized to be *ZB* showed the correct diffraction pattern, with prominent reflections at  $2\theta = 25.5^\circ$ ,  $42.0^\circ$  and  $49.8^\circ$  owing to crystalline planes of  $\langle 111 \rangle$ ,  $\langle 220 \rangle$ , and  $\langle 311 \rangle$  respectively. Likewise, the CdSe synthesized to have the *W*-type showed the correct diffractions, with  $2\theta = 42.0^\circ$ ,  $45.9^\circ$ , and  $50.2^\circ$  arising from reflection from  $\langle 110 \rangle$ ,  $\langle 103 \rangle$ ,  $\langle 112 \rangle$ , respectively and a broad diffraction in the  $23.0^\circ$ - $27.0^\circ$  region.

Importantly, I observed a prominent diffraction at  $45.9^\circ$ , which is a reflection in  $W$  that is lacking in  $ZB$ . In general, these XRDs are broad, due in large part to small grain size of the qdots employed ( $d = 3.6 - 4.0$  nm). I next monitored the crystal structure change upon addition of multiple shells of  $\text{Cd}_x\text{Zn}_{1-x}\text{S}$ .

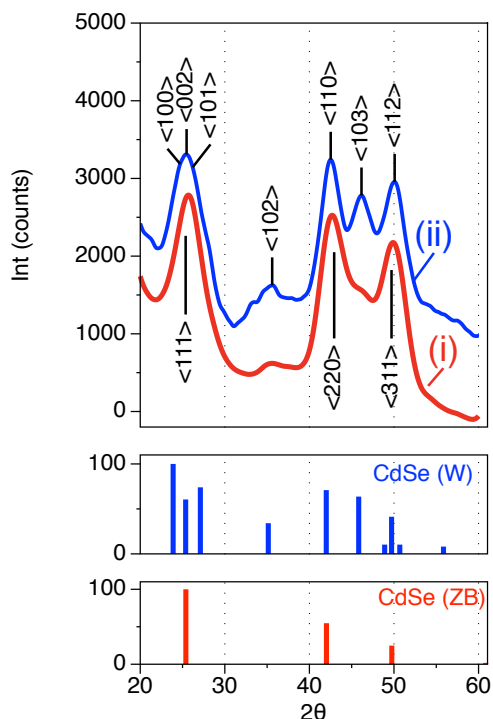


**Figure 2.2:** Representative XRD spectra for ZB- (i) and  $W$ -QD (ii) cores. The CdSe ZB and  $W$  standards are shown as reference. XRD offset vertically for clarity.

Multiple  $\text{Cd}_x\text{Zn}_{1-x}\text{S}$  shells were then deposited onto these cores to probe growth at the two CdSe QDs. To achieve this, I employed the SILAR technique,<sup>34,40</sup> in which aliquots of cation and anion precursors are injected sequentially to increase shell thickness (see methods). UV-Vis (Fig. 2.3a) and PL emission (Fig. 2.3b) monitored shell addition by sampling the synthesis solution after deposition of layers ( $n$ ) at  $n = 4, 8, 12$  and  $18$  starting from  $ZB$  -cores.

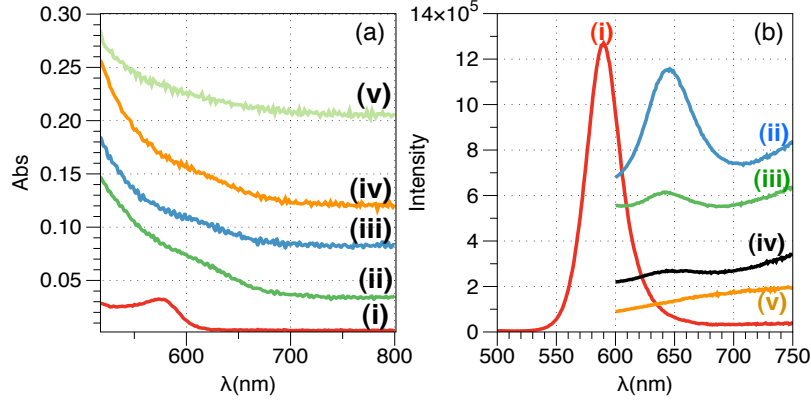


**Figure 2.3:** UV-vis (a) and PL emission (b) results characterizing the gQD growth at ZB-core at  $n = 0$  (i) 4 (ii), 8 (iii), 12 (iv) and 18 (v). PL excitation carried out at 400 nm.

In general, a distinct broad rise in the UV-vis spectra at a higher energy ( $<500$  nm), and a red-shift in  $\lambda_{PL}$  at increasing  $n$  indicated the deposition of the  $Cd_xZn_{1-x}S$  rich shells. The origin of the shift is two fold. First, due to the alloying of the shell, the system ideally would transition to a quasi type II system, in which each layer adds an energy step in the band gap.<sup>15,27</sup> The extent of this step would largely depend on the composition, symmetry and crystallinity of the SILAR layers. For example, asymmetry in a CdSe/CdS system has been shown to lead to a levelling out of the band gap transition<sup>48</sup>. Moreover, extended defects or defects in terms of alloy concentration variation may also lead to a lowering of band gap, which would lead to a red-shift emission especially. A closer inspection of Fig. 2.3b reveals that the PL quantum yield also decays rapidly between  $n = 8$ -18, suggesting a high defect concentration. In addition, any variation in crystal type within the gQD, such as  $W$ -Zb- $W$  layering, may also lead to local areas of confinement, which leads to PL changes.<sup>49</sup> Such crystalline changes or the presence of defects is investigated below.

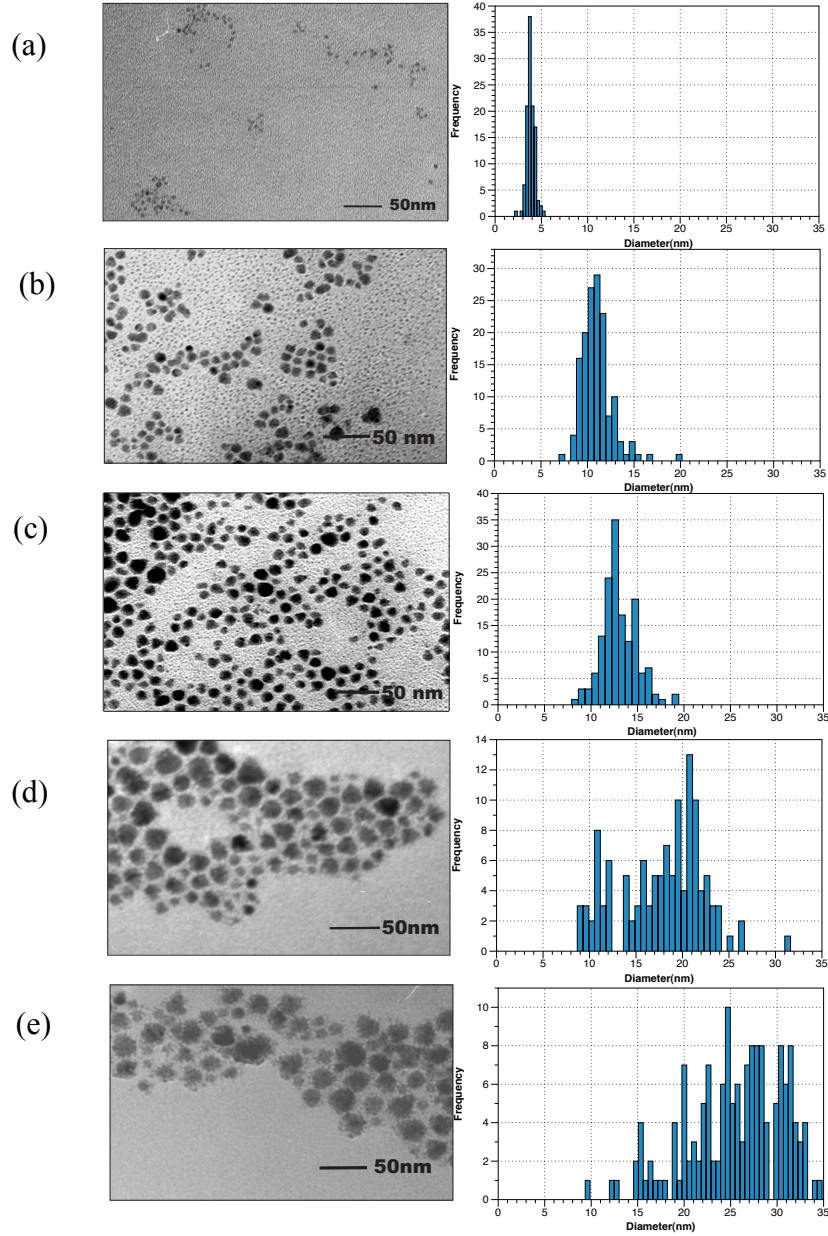


**Figure 2.4:** Representative TEM micrographs and size distribution of the ZB-core ( $d = 3.8 \pm 0.4$  nm) (a), and gQD at shell growth layers of  $n = 4$  ( $d = 10.9 \pm 1.6$  nm) (b), 8 ( $d = 13 \pm 1.9$  nm) (c), 12 ( $d = 17.7 \pm 4.9$  nm) (d) and 18 ( $d = 25.7 \pm 5.3$  nm).

The morphological evolution of the gQDs was monitored by TEM (Fig. 2.4). It was observed that  $d$  increased with  $n$ , and the final gQD were multifaceted with a  $d = 25.7 \pm 5.3$  nm. Interestingly, the polydispersity of the gQDs also increased, indicating some loss of size control over the course of shell growth and long annealing times. Figure 2.5a



shows the trend in gQD  $d$  increase with  $n$ , with the standard deviations ( $\sigma$ ) represented as error bars. The polydispersity increased at  $n > 12$ , and the size distribution histograms deviate from a simple Gaussian distribution, which is related to not only size change, but also shape variation.

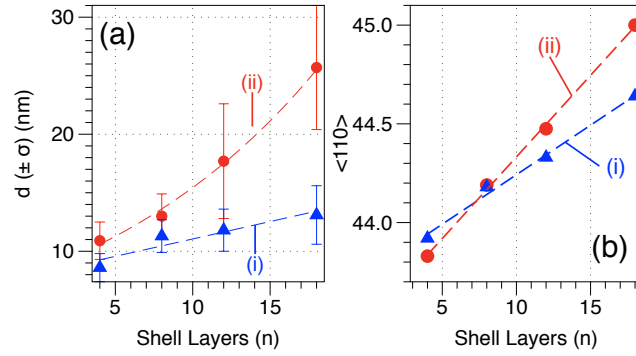


**Figure 2.5:** (a) Plot of TEM determined diameter of gQDs starting from ZB (ii) and W (i) core with the shell layers ( $n$ ). (b) Position of  $\langle 110 \rangle$  reflection with increasing  $n$  using ZB (ii) and W (i) cores.

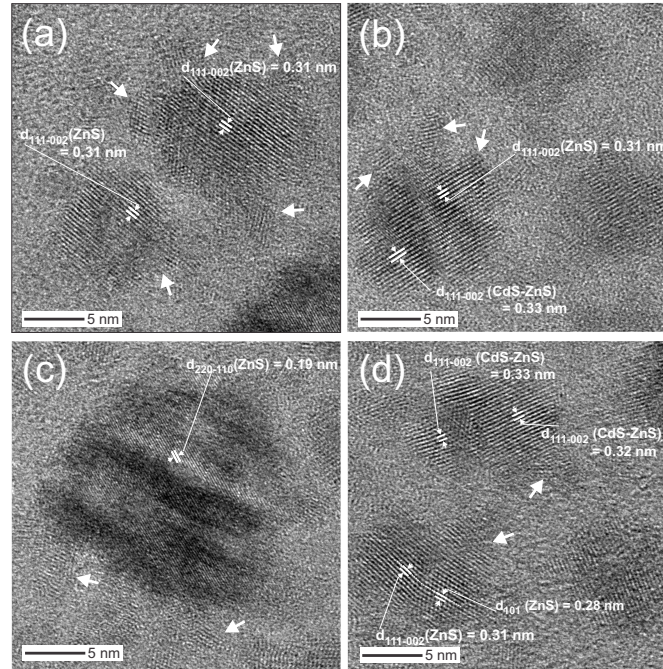


**Figure 2.6:** HRTEM micrographs (a-d) of the gQD products at  $n = 18$  using ZB-cores. Inserted arrows highlight crystalline protrusions.

HRTEM was used to investigate the morphology and crystallinity of the gQD products at  $n = 18$ . As shown in Figure 2.6, the gQDs possess some size disparity, but also considerable defects are observed, such as polycrystalline domains, stacking defects, as well as small crystalline protrusions at the interface. For example, the gQD show lattice spacing consistent with  $\langle 111 \rangle$  of  $ZB$ -ZnS and  $\langle 002 \rangle$  of  $W$ -ZnS. A challenge in this analysis is the identical spacing of these two planes, as described using XRD below. Nevertheless, some gQDs (Fig. 2.6d, Fig. 2.7a) show planes  $\langle 102 \rangle$  spacing consistent with  $W$  regions. These values suggest that the outermost interface is ZnS rich and that planes consistent with both  $ZB$  and  $W$  are present. Moreover, the small protrusions, likely the nucleation points during growth are observed, as highlighted by inserted arrows. The gQDs in Fig. 2.6d show similar defects and varied lattice spacing along a particular row of atoms, which suggest the composition gradient of shell growth may reside at the interface. In addition, considerable stacking faults, as observed in the gQD to the lower right of the micrograph. These results it is clear that the final gQD, while crystalline, possess a great deal of defects, which was attributed to its optical properties described above, namely, the loss in QY and red-shift in PL emission. Moreover, the presence of both  $ZB$  and  $W$  crystalline domains suggest some degree of polytypism in the gQD sample. Fig. 2.7 shows the HRTEM micrographs of some additional nanoparticles. Lattice spacings consistent with  $\langle 111 \rangle$  of  $ZB$ - CdS - ZnS and  $\langle 002 \rangle$  of  $W$ - CdS - ZnS

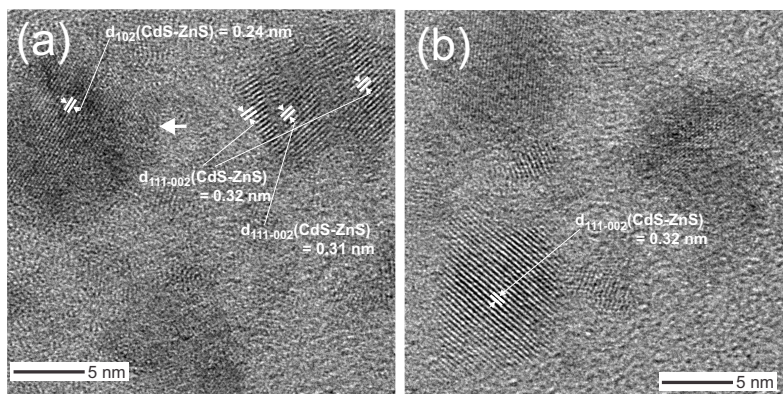


**Figure 2.7:** Additional HRTEM micrographs (a-b) of the gQD products at  $n = 18$  using ZB-cores. Inserted arrows highlight crystalline protrusions

are observed in Fig 2.7 (a, b), along with visible stacking faults along the periphery of a single gQD.

The nature and extent of crystallographic changes during gQD shell growth on the *ZB* core, was studied by XRD. Figure 2.8 shows the XRD patterns at  $n = 4$  (i), 8 (ii), 12 (iii), and 18 (iv). An interesting development during the shell growth was witnessed, where a diffraction pattern that suggests a transformation from a *ZB*-type to a *W*-type shell was observed, as indicated by the emergence of the  $\langle 103 \rangle$  reflection. Furthermore, by comparing to the bulk standards (see insets), this structure more closely resembles the *W*-CdS compared to *W*-ZnS structure, which can be explained considering the fact the shell growth occurred using the  $\text{Cd}_{0.87}\text{Zn}_{0.13}$  precursor feed ratio at the initial stages. Moreover, as this *ZB*-to-*W* transition continues, and a distinct  $\langle 102 \rangle$  plane becomes more prominent at  $n = 12 - 18$ , where the systematic shift to higher  $2\theta$  confirmed Zn-rich alloy deposition at later layers, which is illustrated in Fig. 2.5b by following the  $\langle 110 \rangle$  angle increase with  $n$ . A calculation performed considering the positions of  $\langle 110 \rangle$  peak, from  $n = 4 - 18$ , gives an estimate of the total QD composition of  $\text{Cd}_{98}\text{Zn}_2$  ( $n = 4$ ),  $\text{Cd}_{89}\text{Zn}_{11}$  ( $n = 8$ ),

$\text{Cd}_{81}\text{Zn}_{19}$  ( $n = 12$ ) and  $\text{Cd}_{67}\text{Zn}_{33}$  ( $n = 18$ ). These values are in agreement with the alloy feed ratios.

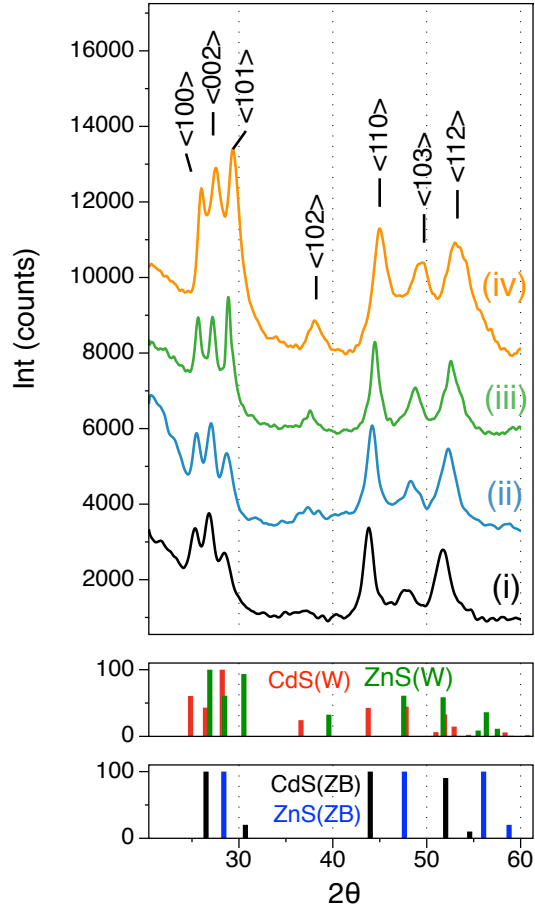


**Figure 2.8:** The powder XRD results for shell growth at ZB-cores at shell layers ( $n$ ) of 4 (i), 8 (ii), 12 (iii), and 18 (iv). The CdS ( $W$ , ZB) and ZnS ( $W$ , ZB) standards are provided for reference. XRD offset vertically for clarity.

I next studied gQD growth using  $W$ -CdSe cores. Figure 2.9 depicts the UV-vis absorption (a) and PL emission spectra (b) obtained at  $n = 4$  (ii), 8 (iii), 12 (iv) and 18 (v).

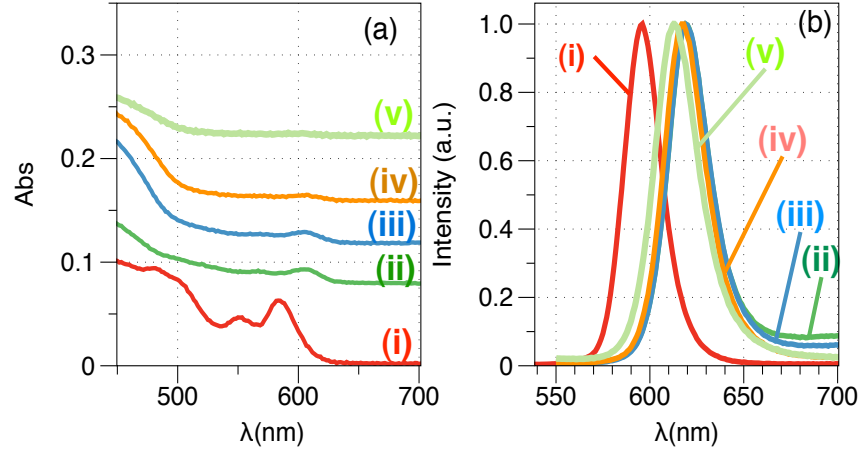


**Figure 2.9:** Representative UV-vis (a) and PL emission (b) results characterizing the gQD growth at  $W$ -core at  $n = 0$  (i) 4 (ii), 8 (iii), 12 (iv) and 18 (v). PL excitation carried out at 400 nm.

Similar to the  $ZB$ -core case (Fig. 2.3a), a broad rise at a higher energy is observed, indicating  $CdZnS$  rich shell growth. However, a unique characteristic is that the first absorption maximum after shell growth ( $\lambda_{Abs} \sim 606$  nm) closely resembles the core absorption (a-i). The intensity of this absorption maximum is however found to progressively diminish, with the increasing  $n$ , due to the screening effects of the thickening shell. The PL emission spectra (Fig. 2.9b) revealed a red shifted PL, again consistent with the successful deposition of  $Cd_xZn_{1-x}S$  shells, and a transition to a quasi Type-II system. A difference in the PL emission compared to the  $ZB$ -system (Fig. 2.3b) was the retaining of considerable QY ( $>5\%$ ) after shell growth, which I attribute to a more crystalline product, as discussed below.

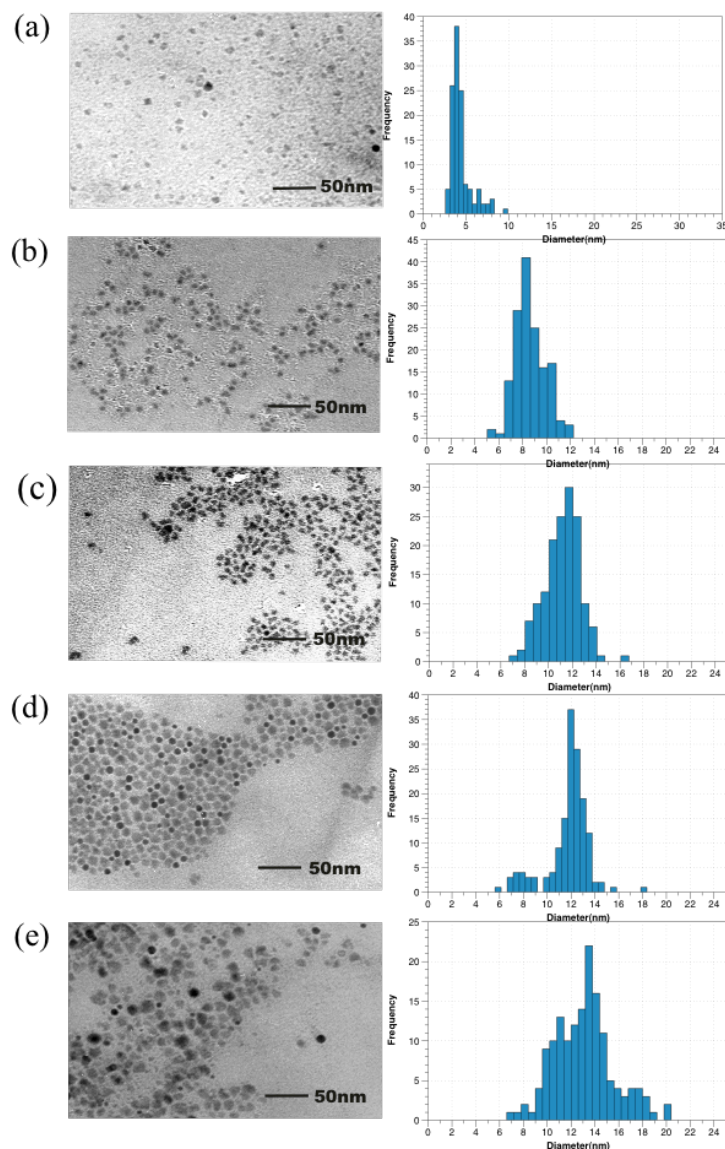


**Figure 2.10:** Representative TEM micrographs and size distribution of the *W*-core ( $d = 4.4 \pm 0.9$  nm) (a), and gQD at shell growth layers of  $n = 4$  ( $d = 8.6 \pm 1.2$  nm) (b), 8 ( $d = 11.3 \pm 1.4$  nm) (c), 12 ( $d = 11.8 \pm 1.8$  nm) (d) and 18 ( $d = 13.1 \pm 2.5$  nm) (e).

Figure 2.10 shows the corresponding TEM micrographs sampled after shell additions. The gQD diameter increased with  $n$ , and the final gQD were also multifaceted, with  $d = 13.1 \pm 2.5$  nm. The size growth and distributions are included in Fig. 2.5a. In general, the polydispersity was much lower than in the *ZB*-core case, along with an observed slower growth rate. The slow growth rate and smaller diameters from the *W* core template might



suggest some degree of independent nucleation, which may be due to insufficient activation of the precursors at the  $W$  interface, due to an inherent disparity in the mechanism and the rate of ion adsorption of shell precursors onto the shell of the gQD with non-identical CdSe cores ( $W$  and  $ZB$ ) as described by recent studies.<sup>18,50</sup>

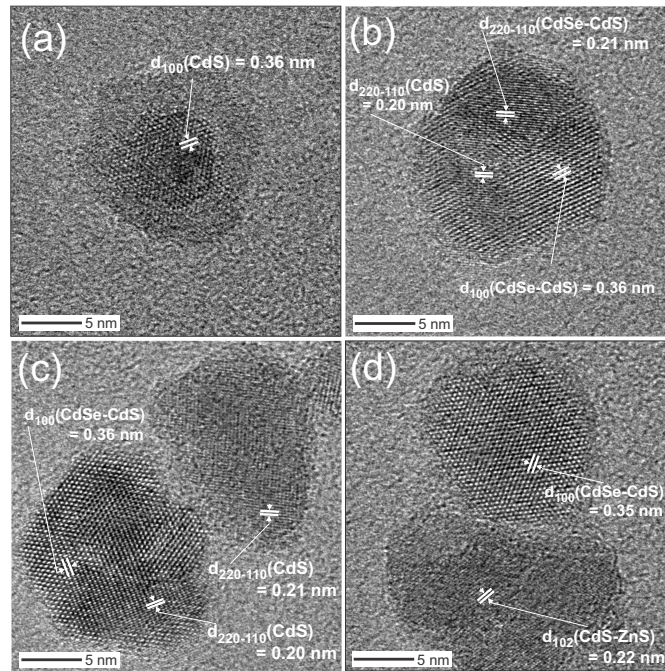


**Figure 2.11:** HRTEM micrographs (a-d) of the gQD products at  $n = 18$  using  $W$ -cores. Inserted arrows highlight crystalline protrusions.

The HRTEM of the gQD products at  $n = 18$  using  $W$ -cores are shown in Figure 2.12. Compared to the gQD from the  $ZB$ -cores (Fig. 2.6), these products have two clear differences. First, the gQD have a much more single-crystalline nature. Second, stacking defects are still evident, and so too is the observation of gQDs that seem to demonstrate twinning. For example, the gQD shown in Fig. 2.11a shows a distinguishable core-shell like morphology, but this was a minority across the sample population. The gQDs like

the one shown in Fig. 2.11b were the most prevalent, which have a faceted/spherical shape, with different crystal facets at the face, with spacings consistent with  $W$   $\langle 100 \rangle$  and  $ZB$   $\langle 220 \rangle$ . Also observed were groups of gQDs that either aggregate together or form dimers, possibly from significant twinning, as shown in Fig. 2.11c-d. A feature of each of these gQDs is one side showing a  $W$   $\langle 100 \rangle$  plane while the other shows a  $ZB$   $\langle 220 \rangle$  one. Interestingly, each of these domains have considerable crystallinity.

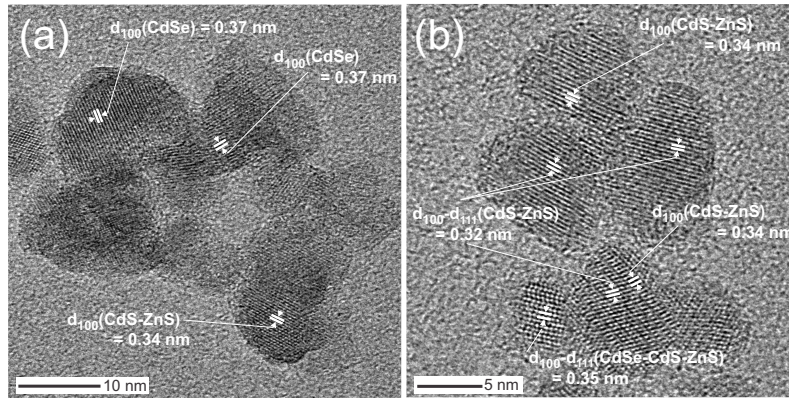


**Figure 2.12:** Additional HRTEM micrographs (a-b) of the gQD products at  $n = 18$  using  $W$ -cores. Inserted arrows highlight crystalline protrusions.

Some additional HRTEM micrographs shown in Fig. 2.12 exhibited aggregates of nanoparticles exhibiting significant stacking faults and twinning along the joining boundaries (a), along with co existence of  $W$  and  $ZB$  domains and varied lattice spacing along the periphery (b) indicating the polytypic nature and existence of alloy gradient on the surface of the gQDs.

Shell growth at the  $W$ -cores was also followed by XRD. Figure 2.13 shows the results at  $n = 4$  (i), 8 (ii), 12 (iii), and 18 (iv). The gQDs exhibited continued  $W$ -type crystal growth at each stage. The shift in  $\langle 110 \rangle$  angle (Fig. 2.5b) was used to estimate the alloy composition of  $\text{Cd}_{96}\text{Zn}_4$  ( $n = 4$ ),  $\text{Cd}_{89}\text{Zn}_{11}$  ( $n = 8$ ),  $\text{Cd}_{85}\text{Zn}_{15}$  ( $n = 12$ ) and  $\text{Cd}_{77}\text{Zn}_{23}$  ( $n = 18$ ), which is consistent with the alloy feed ratio. Interestingly, these values suggest that less Zn was deposited onto the growing gQD compared to the  $ZB$ -cores.



An interesting observation during the multi-shell growth process on *ZB* (Fig. 2.8) and *W*-cores (Fig. 2.13) is that both form predominantly *W*-shells. While it is intuitive that the *W*-core facilitates *W*-shell growth, its growth on the *ZB*-core is less obvious, and is likely due to interfacial coherence of *ZB*  $\langle 111 \rangle$  and *W*  $\langle 002 \rangle$  crystal planes, as described earlier.<sup>18</sup> Moreover, when comparing these two XRD results further, it becomes evident that the  $\langle 110 \rangle$  and  $\langle 112 \rangle$  reflections, using either *ZB*- or *W*-cores, are exceptionally prominent compared to the bulk standards (see insets).

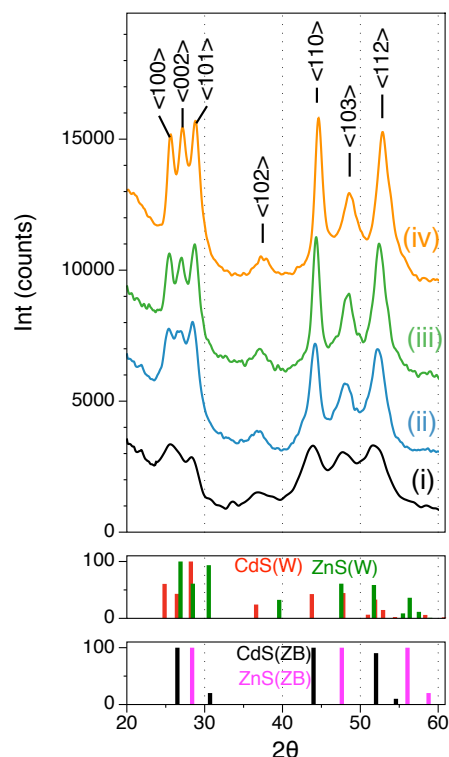


**Figure 2.13:** The powder XRD results for shell growth at *W*-cores at shell layers (*n*) of 4 (i), 8 (ii), 12 (iii), and 18 (iv). The CdS (*W*, *ZB*) and ZnS (*W*, *ZB*) standards are provided for reference. XRD offset vertically for clarity.

This suggests that crystal growth in both cases is not proceeding in a purely crystalline manner (i.e. solely *W*), as suggested by HRTEM, and that *ZB* domains must be forming

within the shell despite *W*-domains being the preferred crystal type.<sup>28</sup> Such polytypism, likely is the result of stacking faults occurring during the course of shell growth and long term annealing. This phenomenon of coexistence of *ZB* and *W* domains in the same crystal has been reported earlier in core/shell QD systems as investigated by HRTEM, where it was shown that the core and shell have different crystal structures.<sup>17, 18, 19</sup> However in this case the polytypism seems to be continuing throughout shell growth and is not limited to the core-shell interface. For example, the  $\langle 002 \rangle$  facets of *W* are atomically identical to the  $\langle 111 \rangle$  of *ZB* (See Fig. 2.2 insets), which can lead to the *W*-shell nucleating at these planes or facets of the QD, as has been observed in the growth of CdSe/CdS tetrapods.<sup>19, 25, 26</sup> In addition, since the ABC stacking direction of  $\langle 111 \rangle$  in *ZB* coincides with the AB stacking direction of  $\langle 002 \rangle$  in *W*,<sup>23</sup> certain complex defects in the stacking sequence (ABABCACA, ABABCBC) may result, especially in the grain boundaries (domain edges). These stacking faults may be the reason, for which, in spite of enforcements from the  $\langle 111 \rangle$  reflection of *ZB* domain, the  $\langle 002 \rangle$  peaks of the gQDs (Fig. 2.8 and 2.13 are not as enhanced as the  $\langle 110 \rangle$  and  $\langle 112 \rangle$  ones, though the relative intensity is still greater compared to that in the standards. The effect seems to be more intense in the case of shell growth on the *W* cores.

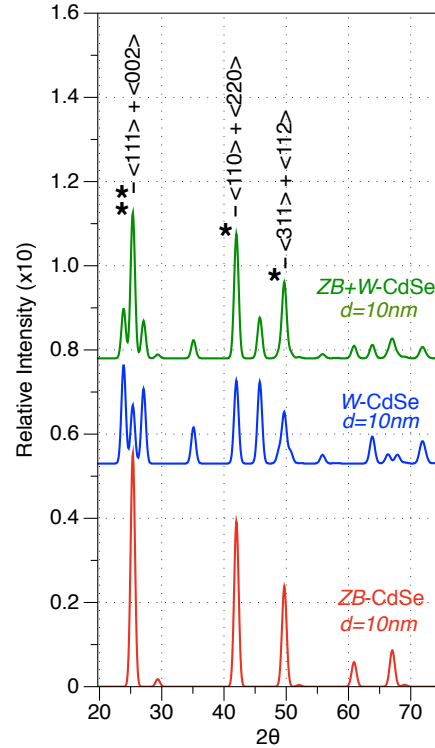


**Figure 2.14:** Powder XRD simulations for a spherical 10 nm CdSe QD with either *ZB* or *W* crystallinity, compared with a 10 nm CdSe QD with equal mixtures of *ZB* + *W*. The reflections corresponding to the sum or  $\langle 110 \rangle + \langle 220 \rangle$ , and  $\langle 311 \rangle + \langle 112 \rangle$  correspond closely with the results shown in Fig. 5 and 7, whereas the sum of  $\langle 111 \rangle + \langle 002 \rangle$  is not observed in the experimental results, suggesting considerable stacking faults along those planes. XRD offset vertically for clarity.

To better illustrate this, Figure 2.14 shows the simulated powder XRD for a 10 nm CdSe QD core with either *ZB*- or *W*-type crystallinity. I chose a 10 nm size and CdSe type for simplicity. Also shown is a 10 nm CdSe core with an equal mixture of *ZB* and *W* crystallinity. As can be observed from this simple model, the XRD pattern shows trends very similar to the experimental XRD in Fig. 2.8 and 2.13. For instance, the model polytypic QD shows high intensities corresponding to the sum or  $\langle 110 \rangle + \langle 220 \rangle$ , and  $\langle 311 \rangle + \langle 112 \rangle$  planes, which closely trend with the results shown in Fig. 2.8 and 2.13. In contrast, the estimated plane corresponding to the sum of  $\langle 111 \rangle + \langle 002 \rangle$  is not

observed in the experimental results, suggesting considerable stacking faults must exist along these planes.<sup>51</sup>

One possible reason for this polytypic growth may be the use of SILAR itself. In contrast to CdSe/CdS rods and tetrapods, both of which are grown rapidly in excess shell materials, and result in *W*-type growth,<sup>26,52</sup> the slow SILAR addition uses a limited amount of shell precursors, which may lead to sub-monolayer, or non-uniform layering, which introduces additional extended defects that can lead to further irregularities and ripening. This effect is further propagated greatly in the current system, since this SILAR addition is repeated many times ( $n = 18$ ) over the course of many hours. Thus, the shell growth is less kinetically driven compared to the rod or tetrapod case, each of which uses shell growth in large excess of that required, and growth occurs largely in one nucleation step. In addition, the temperatures used for shell growth ( $T = 240\text{ }^{\circ}\text{C}$ ) may also be too close to the *ZB*-to-*W* transition, and provides insufficient energy to anneal the *W* crystal completely, leading to a high probability of interconversion.<sup>24</sup> For instance, in the *ZB* core gQD growth process discussed above, the initial stages of  $\text{Cd}_x\text{Zn}_{1-x}\text{S}$  ( $x \approx 1$ ), may resemble the growth of CdSe/CdS tetrapods, where *W*-growth nucleates at *ZB*  $\langle 111 \rangle$  faces, which would result in a stilted tetrapod-like morphology.<sup>18</sup> Evidence for this is shown in the HRTEM of Fig. 2.6 and 2.7a, where small crystalline protrusions can be observed when using *ZB* cores. Another possibility is that the alloy gradient employed, and its deposition mechanism is inducing the polytypism. Since in our system during shell growth, precursors of each cation and anion are available, multiple lattice distances are possible. Fig 2.15 shows the change in UV-vis absorption of *W* (a, b) and *ZB* (c, d)

CdSe cores during the course of annealing in presence of excess OAc acid and DOA (See section 2.2.2.4) respectively. Extensive etching of both *W* and *ZB* CdSe cores is observed during heating in presence of excess OAc ligand in the reaction medium at the initial stages, followed by ripening with the increase of temperature is depicted by the shift of  $\lambda_{\text{Abs}}$  (Fig. 2.15 a, c). Thus it can be expected that low concentrations of  $\text{Se}^{2-}$  ions are present in the first few shell layers, resulting from the ligand induced core etching in either case.

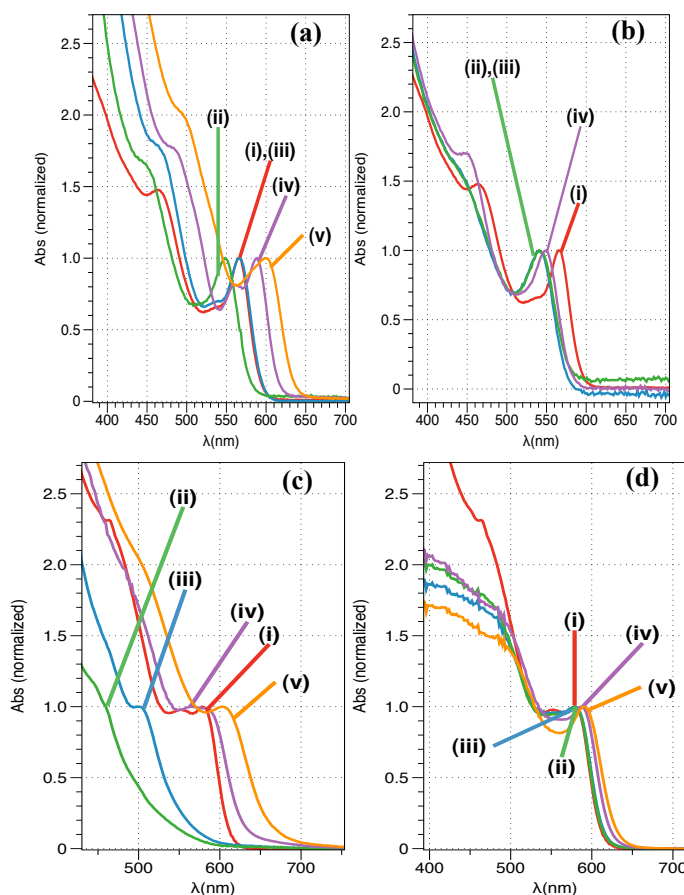


**Figure 2.15:** (a-b) UV-vis spectra monitoring of *W*-CdSe cores during annealing in excess OAc (a) or DOA (b) from room temperatures (i), to 110°C for 1h (ii), to 190°C for 1hr (iii), to 240°C for 0.5h (iv) and 1.5 hr (v). (c-d) Similar UV-vis monitoring for annealing of *ZB*-CdSe core in excess OAc (c) and DOA (d) for similar temperatures and annealing times.

This co-existence of multiple precursor types can lead to multiple lattice strains (up to ~9% between CdSe and ZnS)<sup>37</sup> during growth, which may lead to defect formation. Thus it is reasonable to assume during the course of multiple shell addition onto the CdSe core, defects or dislocations might result in the strained lattice of the shell crystal structure. In addition, thermodynamics work has shown that *ZB*-CdS and *ZB*-ZnS have a slightly higher stability, unlike CdSe in which the *W* is favored.<sup>24,53</sup>

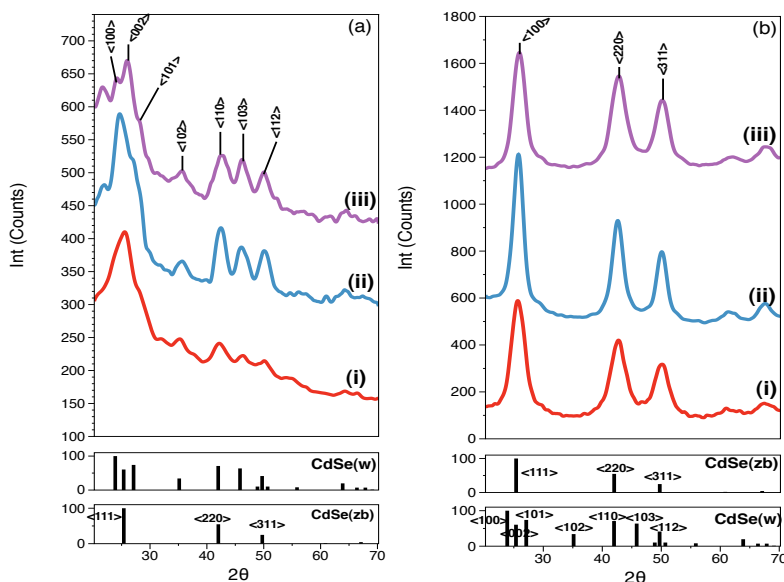


**Figure 2.16:** Powder XRD results characterizing the *W*- (a) and *ZB*- (b) CdSe cores (i) after completing the annealing cycle described in Fig. 2.15 with excess OAc (ii) and excess DOA (iii). CdSe (*W*, *ZB*) standards are provided for reference. XRD offset vertically for clarity.

Control experiments heating the *ZB*- and *W*-cores in both oleic acid and dioctylamine did not lead to a crystal structure change or evidence of polytypism formation, and thus it can be assumed that the cores stay at their original form during shell growth (Fig. 2.16). Finally, the role that the ligands are playing, both at the interface and in stabilizing the precursors, and their purity,<sup>54</sup> should be considered. It has been shown that oleic acid and metal oleates stabilize the *ZB* phase at elevated temperature, where considering the effects

described above, one typically predicts *W*-phases.<sup>17,19,42</sup> To complicate matters further, primary amines and tertiary amines were observed to stabilize / promote shell growth of *W*- and *ZB*-phases respectively<sup>17</sup> which resulted in evidence of polytypism. In our system, dioctylamine is the ligand in highest concentration, however oleates are used in precursor formation. Thus, while the dioctylamine may promote *W*-growth, lower concentrations of oleates may be playing a considerable role or acting as an intermediate during cation deposition. Evidence of this was recently reported for CdSe/CdS<sup>42</sup> QDs and Co nanocrystals,<sup>55</sup> in which each case reported OAc/DOA combinations lead to polytypic growth.

## 2.6 Conclusion

In conclusion, a study on the synthesis of the gQDs starting from either Zinc blende or Wurtzite CdSe cores has been performed. I found that the deposited CdZnS shell preferred a Wurtzite crystal type, but that significant polytypism was observed. Defects and domains of both Zinc Blende and Wurtzite were observed by HRTEM. Comparing the observed XRD with model simulations ruled out that multiple types of gQDs existed in the population, and suggested the polytypism occurs in each gQD due to stacking defects throughout the course of shell growth. The potential causes of the polytypism include; the temperature that the SILAR growth was carried out at, the CdZnS alloyed shells used, as well as the potential role that the dioctylamine plus oleate ligand shell is playing. These results may aid in the better understanding of growth morphology and photophysical properties of multi-shell giant quantum dots.

## 2.7 References

- (1) Weller, H. *Angew. Chem. Int. Ed. Engl.* **1993**, 32 (1), 41–53.
- (2) Alivisatos, A. P. *Science* **1996**, 271, 933–937.
- (3) Nirmal, M.; Brus, L. *Acc. Chem. Res.* **1999**, 32, 407–414.
- (4) Alivisatos, P. *Nat. Biotechnol.* **2003**, 22 (1), 47–52.
- (5) Medintz, I. L.; Uyeda, T. H.; Goldman, E. R.; Mattoussi, H. *Nat. Mater.* **2005**, 4, 435–446.
- (6) Hahn, M. A.; Tabb, J. S.; Krauss, T. D. *Anal. Chem.* **2005**, 77 (15), 4861–4869.
- (7) Ruan, G.; Agrawal, A.; Marcus, A. I.; Nie, S. *J. Am. Chem. Soc.* **2007**, 129 (47), 14759–14766.
- (8) Alam, R.; Fontaine, D. M.; Branchini, B. R.; Maye, M. M. *Nano Lett.* **2012**, 12 (6), 3251–3256.
- (9) Alam, R.; Zylstra, J.; Fontaine, D. M.; Branchini, B. R.; Maye, M. M. *Nanoscale* **2013**, 5 (12), 5303.
- (10) Zhao, J.; Bardecker, J. A.; Munro, A. M.; Liu, M. S.; Niu, Y.; Ding, I.-K.; Luo, J.; Chen, B.; Jen, A. K.-Y.; Ginger, D. S. *Nano Lett.* **2006**, 6 (3), 463–467.
- (11) Anikeeva, P. O.; Halpert, J. E.; Bawendi, M. G.; Bulović, V. *Nano Lett.* **2009**, 9 (7), 2532–2536.
- (12) Klimov, V. I.; Ivanov, S. A.; Nanda, J.; Achermann, M.; Bezel, I.; McGuire, J. A.; Piryatinski, A. *Nature* **2007**, 447 (7143), 441–446.
- (13) Kazes, M.; Lewis, D. Y.; Ebenstein, Y.; Mokari, T.; Banin, U. *Adv. Mater.* **2002**, 14 (4), 317.



- (14) Zavelani-Rossi, M.; Lupo, M. G.; Krahne, R.; Manna, L.; Lanzani, G. *Nanoscale* **2010**, 2 (6), 931.
- (15) García-Santamaría, F.; Chen, Y.; Vela, J.; Schaller, R. D.; Hollingsworth, J. A.; Klimov, V. I. *Nano Lett.* **2009**, 9 (10), 3482–3488.
- (16) Reiss, P.; Protière, M.; Li, L. *small* **2009**, 5 (2), 154–168.
- (17) Mahler, B.; Lequeux, N.; Dubertret, B. *J. Am. Chem. Soc.* **2009**, 132 (3), 953–959.
- (18) Xia, X.; Liu, Z.; Du, G.; Li, Y.; Ma, M. *J. Lumin.* **2010**, 130 (7), 1285–1291.
- (19) Mishra, N.; Lian, J.; Chakraborty, S.; Lin, M.; Chan, Y. *Chem. Mater.* **2012**, 24 (11), 2040–2046.
- (20) Hines, M. A.; Guyot-Sionnest, P. *J. Phys. Chem.* **1996**, 100 (2), 468–471.
- (21) Dabbousi, B. O.; Rodriguez-Viejo, J.; Mikulec, F. V.; Heine, J. R.; Mattoussi, H.; Ober, R.; Jensen, K. F.; Bawendi, M. G. *J Phys Chem B* **1997**, 101, 9463–9475.
- (22) Steckel, J. S.; Zimmer, J. P.; Coe-Sullivan, S.; Stott, N. E.; Bulović, V.; Bawendi, M. G. *Angew. Chem. Int. Ed.* **2004**, 43 (16), 2154–2158.
- (23) Bakke, J. R.; Jung, H. J.; Tanskanen, J. T.; Sinclair, R.; Bent, S. F. *Chem. Mater.* **2010**, 22 (16), 4669–4678.
- (24) Yeh, C.-Y.; Lu, Z. W.; Froyen, S.; Zunger, A. *Phys. Rev. B* **1992**, 46 (16), 10086.
- (25) Fiore, A.; Mastria, R.; Lupo, M. G.; Lanzani, G.; Giannini, C.; Carlino, E.; Morello, G.; De Giorgi, M.; Li, Y.; Cingolani, R.; Manna, L. *J. Am. Chem. Soc.* **2009**, 131 (6), 2274–2282.
- (26) Talapin, D. V.; Nelson, J. H.; Shevchenko, E. V.; Aloni, S.; Sadtler, B.; Alivisatos, A. P. *Nano Lett.* **2007**, 7 (10), 2951–2959.

- (27) Kudera, S.; Carbone, L.; Manna, L.; Parak, W. J. In *Semiconductor Nanocrystal Quantum Dot Synthesis, Assembly, Spectroscopy and Applications*; Rogach, A. L., Ed.; SpringerWienNewYork: New York, 2008; pp 1–34.
- (28) Hughes, S. M.; Alivisatos, A. P. *Nano Lett.* **2013**, *13* (1), 106–110.
- (29) Akiyama, T.; Nakamura, K.; Ito, T. *Phys. Rev. B* **2006**, *73* (23).
- (30) Vasiliev, R. B.; Dirin, D. N.; Sokolikova, M. S.; Roddatis, V. V.; Vasiliev, A. L.; Vitukhnovsky, A. G.; Gaskov, A. M. *J. Mater. Res.* **2011**, *26* (13), 1621–1626.
- (31) Banin, U.; Bruchez, M.; Alivisatos, A. P.; Ha, T.; Weiss, S.; Chemla, D. S. *J. Chem. Phys.* **1999**, *110* (2), 1195.
- (32) Kuno, M.; Fromm, D. P.; Hamann, H. F.; Gallagher, A.; Nesbitt, D. J. *J. Chem. Phys.* **2001**, *115* (2), 1028.
- (33) Green, M. *J. Mater. Chem.* **2010**, *20* (28), 5797.
- (34) Chen, Y.; Vela, J.; Htoon, H.; Casson, J. L.; Werder, D. J.; Bussian, D. A.; Klimov, V. I.; Hollingsworth, J. A. *J. Am. Chem. Soc.* **2008**, *130* (15), 5026–5027.
- (35) Qu, L.; Peng, X. *J. Am. Chem. Soc.* **2002**, *124* (9), 2049–2055.
- (36) Zylstra, J.; Amey, J.; Miska, N. J.; Pang, L.; Hine, C. R.; Langer, J.; Doyle, R. P.; Maye, M. M. *Langmuir* **2011**, *27* (8), 4371–4379.
- (37) Talapin, D. V.; Mekis, I.; Götzinger, S.; Kornowski, A.; Benson, O.; Weller, H. *J. Phys. Chem. B* **2004**, *108* (49), 18826–18831.
- (38) Han, H.; Zylstra, J.; Maye, M. M. *Chem. Mater.* **2011**, *23* (22), 4975–4981.
- (39) Qu, L.; Yu, W. W.; Peng, X. *Nano Lett.* **2004**, *4* (3), 465–469.
- (40) Li, J. J.; Wang, Y. A.; Guo, W.; Keay, J. C.; Mishima, T. D.; Johnson, M. B.; Peng, X. *J. Am. Chem. Soc.* **2003**, *125* (41), 12567–12575.

- (41) Guo, Y.; Marchuk, K.; Sampat, S.; Abraham, R.; Fang, N.; Malko, A. V.; Vela, J. *J. Phys. Chem. C* **2012**, *116* (4), 2791–2800.
- (42) Ghosh, Y.; Mangum, B. D.; Casson, J. L.; Williams, D. J.; Htoon, H.; Hollingsworth, J. A. *J. Am. Chem. Soc.* **2012**, *134* (23), 9634–9643.
- (43) Yu, W. W.; Qu, L.; Guo, W.; Peng, X. *Chem. Mater.* **2003**, *15* (14), 2854–2860.
- (44) Jasieniak, J.; Smith, L.; Embden, J. van; Mulvaney, P.; Califano, M. *J. Phys. Chem. C* **2009**, *113* (45), 19468–19474.
- (45) Demchenko, D.; Wang, L.-W. *Phys. Rev. B* **2006**, *73* (15).
- (46) Mohamed, M. B.; Tonti, D.; Al-Salman, A.; Chemseddine, A.; Chergui, M. *J. Phys. Chem. B* **2005**, *109* (21), 10533–10537.
- (47) Jasieniak, J.; Bullen, C.; van Embden, J.; Mulvaney, P. *J. Phys. Chem. B* **2005**, *109* (44), 20665–20668.
- (48) Borys, N. J.; Walter, M. J.; Huang, J.; Talapin, D. V.; Lupton, J. M. *Science* **2010**, *330* (6009), 1371–1374.
- (49) Ikejiri, K.; Kitauchi, Y.; Tomioka, K.; Motohisa, J.; Fukui, T. *Nano Lett.* **2011**, *11* (10), 4314–4318.
- (50) Erwin, S. C.; Zu, L.; Haftel, M. I.; Efros, A. L.; Kennedy, T. A.; Norris, D. J. *Nature* **2005**, *436* (7047), 91–94.
- (51) Murray, C. B.; Norris, D. J.; Bawendi, M. G. *J. Am. Chem. Soc.* **1993**, *115* (19), 8706–8715.
- (52) Carbone, L.; Nobile, C.; De Giorgi, M.; Sala, F. D.; Morello, G.; Pompa, P.; Hytch, M.; Snoeck, E.; Fiore, A.; Franchini, I. R.; Nadasan, M.; Silvestre, A. F.; Chiodo, L.; Kudera, S.; Cingolani, R.; Krahne, R.; Manna, L. *Nano Lett.* **2007**, *7* (10), 2942–2950.

- (53) Alvarado, S. R.; Guo, Y.; Ruberu, T. P. A.; Tavasoli, E.; Vela, J. *Coord. Chem. Rev.* **2014**, 263-264, 182–196.
- (54) Wang, F.; Tang, R.; Buhro, W. E. *Nano Lett.* **2008**, 8 (10), 3521–3524.
- (55) Bao, Y.; An, W.; Turner, C. H.; Krishnan, K. M. *Langmuir* **2010**, 26 (1), 478–483.

## Chapter 3

### ***Investigating the role of mode of addition and source of 'S' shell precursors during growth of CdSe/CdZnS giant quantum dots***

In this work I investigate the influence of shell precursor monomer concentrations on the synthesis of CdSe/CdZnS giant quantum dots (gQDs). For the study,  $\text{Cd}_x\text{Zn}_{1-x}\text{S}$  gradient multi-shell growth was initiated at Wurtzite (*W*) CdSe cores via two procedures: (a) layer-by-layer SILAR and (b) single step injection (seeded growth). The influence of precursor reactivities on seeded growth of gQDs was further explored by employing three different of 'S' precursor sources (a)  $\text{S}_8$  dissolved in octadecene ( $\text{S}_8/\text{ODE}$ ), (b)  $\text{S}_8$  in trioctylphosphine ( $\text{S}=\text{TOP}$ ) and (c) dodecanethiol (DDT). The optical, crystalline and morphological evolution at each stage of shell growth was studied for each synthesis. Monomer concentration variance induced by altering the mode of addition and the source of 'S' precursors in the syntheses was found to alter the mechanism and kinetics of the gQD growth in each case. Sequential injection of calculated amount of shell precursors (low precursor infusion rate) yielded ligand directed anisotropic *W* novel rod shaped gQDs in SILAR. In the case of seeded growth (high precursor infusion rate) innate crystal structure preference of CdS and ZnS in coupled with the delicate interplay of ligands seemed to play a pivotal role in determining the crystallographic and morphological evolution of the gQDs, yielding tripodal (*ZB*), trigonal (*ZB-W*) and polyhedral (*ZB*) shaped gQDs for  $\text{S}_8/\text{ODE}$ ,  $\text{S}=\text{TOP}$  and DDT mediated syntheses respectively. This work is in progress, and will be submitted to *Chem. Mater.*

### 3.1 Introduction

Nearly three decades of extensive research has established the immense potential of QDs for applications in fundamental research as well as applied sciences ranging from biomimetic energy transfer,<sup>1-3</sup> solar cells and lasers,<sup>4-7</sup> light emitting diodes (LEDs)<sup>8,9</sup> as well as in biolabeling and biotechnology.<sup>10-13</sup> Researches focused on study of shape tunable properties of QDs has established that QDs can be synthesized to possess varied morphologies employing a wide range of ligands.<sup>14-21</sup> The mechanistic pathways of the syntheses often involve the selective adsorption of ligands to specific crystal facets, leads to lowering of surface energies of the binding sites, thereby promoting growth along the activated, uncoordinated facets.<sup>22-26</sup> Though a wealth of knowledge exists for achieving varied morphologies through individually tailored synthetic routes, limited research has been directed towards the development of a general colloidal synthetic scheme, in which, only minor modifications of the same basic technique employing similar set of ligands and synthetic parameters leads to variation in crystal growth morphologies. Precisely, to address these queries, I introduce a model synthetic route for CdSe/CdZnS multishell giant quantum dots (gQDs), where variations in the nature of the ligands, available monomer concentration and source of shell precursors are observed to have a profound effect on the growth of the gQDs.

QDs with thick inorganic shells grown on the core surface have reduced 'blinking' tendencies due to efficient isolation of exciton from the surface interface.<sup>5,27-29</sup> These gQDs resist photobleaching and are robust to chemical and photodegradation making them ideal substrate for applications like single molecular tracking, single photon sources and photothermal probes.<sup>30-35</sup> In my previous work I had investigated the effect

of core crystallinity on the crystallographic evolution of the gQDs, and elucidated how traditional synthetic methodology might lead to the unique occurrence of polytypic (mixed *Wurtzite* – *Zinc blende*) crystallinity.<sup>36</sup>

Here, I investigate the photophysical, crystallographic and morphological changes during growth of  $\text{Cd}_x\text{Zn}_{1-x}\text{S}$  gradient shells by two distinct synthetic methodologies: SILAR and seeded growth starting from *W*-CdSe QD cores. Further, gQD seeded growth employing three types of ‘S’ precursors were investigated. UV-vis and PL spectroscopic techniques were employed to probe the change in photophysical properties, while the Powder X-ray diffraction (XRD) was used to observe crystal structure evolution during shell growth process of gQDs. TEM and HRTEM provided visual input into the morphological evolution and electron diffraction studies provided evidence for the crystallinity and morphology of the gQDs. Though performed on similar cores, the syntheses resulted in gQDs having highly disparate crystal structures and morphology in each case. The kinetic, thermodynamic factors during shell growth process; the critical role played by the ligands, the nature and amount of shell precursor introduced, has been discussed in detail, which resulted in such structures.

## **3.2 Experimental**

### **3.2.1 Chemicals and Materials**

Cadmium oxide (CdO, 99.99%), dioctylamine (DOA, 95%), sulfur (reagent grade, ~ 100 mesh), selenium powder (Se, reagent grade, 99.999), 1- dodecanethiol (DDT, 98%) oleic acid (OAc, 90%), 1-octadecene (ODE 90%), acetonitrile (99.8%) and trioctylphosphine (TOP, 97%) were purchased from Aldrich and used without further purification.

Trioctylphosphine oxide (TOPO, 90%) was purchased from Sigma Aldrich and used after purification (dissolving and recrystallizing from acetonitrile). Zinc oxide (ZnO, 99.0%) was purchased from Fluka Analytical and used without purification. Ethanol (EtOH, 99.5%), were purchased from Sigma Aldrich. Chloroform (Cl, 99.8%), Toluene (Tl, 99.8%) and Rhodamine 6G (R6G, 99%) were acquired from Sigma Aldrich.

### **3.2.2 Synthesis**

#### **3.2.2.1 Synthesis of *Wurtzite (W)* CdSe Cores**

Two sets of similar CdSe cores were employed for the four syntheses, denoted as core – A and core – B. Core – A were utilized to synthesize the gQDs via SILAR, S<sub>8</sub>/ODE and S=TOP mediated seeded processes, while a second set of CdSe cores (core – B) were employed for the DDT mediated seeded synthesis. Both set of cores were synthesized by identical synthetic protocol following traditional methods with minor modifications.<sup>1,15,37</sup> Briefly in a typical synthesis, CdO (0.121 g, 0.84 mmol), TOPO (6.002 g, 15.4 mmol), ODPA (0.561 g, 1.68 mmol) and 4 mL ODE were mixed in a 25 mL three necked flask, and degassed (under vacuum) for 1hr. Following degassing, the reaction mixture was heated to 330°C under Ar atmosphere, to dissolve CdO. The color of the solution was found to change from reddish brown to clear and colorless at that temperature, following which the reaction mixture was heated to 360°C. When the temperature stabilized, Se (1.48 g, 18.74 mmol) dissolved in TOP (3.0 ml, 6.72 mmol) prepared separately in glove box was rapidly injected into the reaction mixture to induce nucleation of CdSe cores. After 1 min of growth of the CdSe QD cores, the heating mantle was removed and the reaction was allowed to cool down to room temperature. To prevent solidification of TOPO, ~ 2 mL toluene was added when the temperature reached



60°C. The QDs were then purified free of excess ligands by multiple acetone precipitation, toluene redissolution cycles (3 times). Final QD product was dried and dispersed in toluene. The approximate QD size and concentration was calculated as described in Sec. 3.4.1 and 3.5.

### 3.2.2.2 Synthesis of Multishelled Giant Quantum Dots (gQDs)

The syntheses of gQDs at *W* CdSe cores were carried out by two separate procedures: first, via the SILAR<sup>38</sup> process following the procedure described by Hollingsworth and co-workers<sup>27,28</sup> and secondly via seeded growth process.<sup>15,37</sup>

#### 3.2.2.2.1 Synthesis of *SILAR* process gQDs

The procedure is a modified version of the successive ionic layer adsorption reaction (SILAR)<sup>38</sup> technique. Briefly, a 0.2 M solution of elemental S<sub>8</sub> dissolved in ODE, 0.2 M Cd-oleate (obtained by dissolving CdO in oleic acid) and 0.2 M Zn-oleate (obtained by dissolving ZnO in oleic acid) solutions were prepared separately. These Zn-oleate and Cd-oleate solutions were then mixed at varied molar ratios to obtain Cd<sub>x</sub>Zn<sub>1-x</sub>-oleate solutions at three feed ratios, which is denoted as Cd<sub>0.87</sub>Zn<sub>0.13</sub>-oleate, Cd<sub>0.51</sub>Zn<sub>0.49</sub>-oleate and Cd<sub>0.22</sub> Zn<sub>0.78</sub>-oleate. These stock solutions were then used to deposit the multiple shells (18) at the CdSe cores, in which the first 6 layers of deposition (*n*) consisted of Cd<sub>0.87</sub>Zn<sub>0.13</sub>-oleate (*n* = 1-6), followed by 6 layers of Cd<sub>0.51</sub>Zn<sub>0.49</sub>-oleate (*n* = 6-12), followed by 6 layers of Cd<sub>0.22</sub> Zn<sub>0.78</sub>-oleate (*n* = 12-18) and finally, the stock solution of 0.2 M Zn oleate was used to deposit 4 layers of Zn-oleate (*n* = 18-22) on the CdSe cores.

To prepare the gQDs from *W*-CdSe cores, first 0.050 moles of DOA (12 g, 15.02 mL) and 0.048 moles of ODE (12 g, 15.21 mL) were added to a 50 mL flask containing

$6.0 \times 10^{-7}$  mol of dried *W*-CdSe cores (Core – A) and degassed at 120°C under vacuum for 1 hr. The secondary amine dioctylamine (DOA) was chosen as a ligand in place of a primary amine, to prevent the reaction between the Cd-oleate and amine ligands as described recently.<sup>32</sup> After the degassing, the reaction temperature was raised and maintained at 240°C under Ar atmosphere. For each layer (*n*) of growth, firstly a calculated volume of S<sub>8</sub> in ODE solution, followed by a calculated volume of Cd<sub>*x*</sub>Zn<sub>1-*x*</sub>-oleate solution is injected into the reaction mixture. The quantity of precursors needed for each *n* was calculated using the volume increment of each layer, considering both the changing QD size, and the residual QD concentration after sampling aliquots for analysis. Growth times were 0.42 h for sulfur and 0.42 h for the cation precursors. In this manner, 22 layers of Cd<sub>*x*</sub>Zn<sub>1-*x*</sub>S were grown using Cd<sub>0.87</sub>Zn<sub>0.13</sub>-oleate for the *n* = 1-6, Cd<sub>0.51</sub> Zn<sub>0.49</sub>-oleate for *n* = 6-12, and Cd<sub>0.22</sub> Zn<sub>0.78</sub>-oleate for *n* = 12-18, followed by final 4 layers of ZnS using Zn-oleate for *n* = 18-22. Thus Cd concentration in the alloy shell decreases from the core to the periphery. These gQDs were precipitated from growth solution by acetone and redissolved in toluene. Further, they were subsequently subjected to multiple acetone precipitation - redissolution in toluene cycle purification steps to get rid of excess ligands and unreacted precursors.

#### 3.2.2.2.2 Synthesis of *Seeded* growth gQDs

The seeded growth<sup>15,37</sup> process of gQDs was inspired by the SILAR process described above in that, the molar concentration of [QD] to shell precursor materials were kept identical in both cases. The thought behind keeping identical molar ratios in SILAR and seeded growth was to compare and see if the difference in the concentration of shell

precursors resulting from the disparate mode of precursor infusion in the two cases result in alteration of gQD growth pattern. Briefly, the seeded growth process involved [CdSe QD core] : [shell precursors]  $\approx$  1 : 9200,  $[\text{Cd}^{+2}] : [\text{Zn}^{+2}] = 24 : 76 (\approx 1 : 3)$  in the total concentration of cationic shell precursors added, and [cationic shell precursor] : [S shell precursor] = 1 : 1. Instead of adding shell precursors in 22 subsequent injections over a period of 9 hr (SILAR), the CdSe core + anionic shell precursor (S precursor) was introduced into the reaction medium containing the cationic shell precursors (Cd/Zn-oleate) at a fixed temperature (240°C) in a rapid single injection step and annealed for 9 hr. The growth of gQDs was monitored by sampling out aliquots at regular time intervals. Further, three types of S precursor sources viz. (a) S<sub>8</sub> dissolved in octadecene (S<sub>8</sub>/ODE), (b) S<sub>8</sub> in trioctylphosphine (S=TOP) and (c) dodecanethiol (DDT) were investigated, with a view of understanding how the source of ‘S’ shell precursors influence the gQD growth process during seeded addition.

The seeded growth syntheses for the three sources of ‘S’ precursors were carried out by the exact same synthetic protocol. In a typical seeded synthesis, Cadmium oxide (CdO) and Zinc oxide (ZnO) were mixed with oleic acid (OA) and ODE in a 50 ml four necked flask and degassed (under vacuum) for 1hr. Following degassing the reaction mixture was heated to 280°C in an inert atmosphere to dissolve CdO and ZnO and form their respective oleates. The color of the reaction mixture was found to change from dark reddish to milky white and finally clear and colorless. At this point, dioctylamine (DOA, kept in glove box), was rapidly injected and temperature of the reaction mixture was decreased to 240 °C. When the temperature stabilized, an injection containing CdSe core and ‘S’ shell precursor (separately prepared in glove box) was rapidly injected into the

reaction mixture, to induce shell growth on the CdSe cores. The temperature was allowed to stabilize 240 °C following the injection, and maintained stationary for 9 hr, during the course of which growth of gQDs occurred. The molar ratios employed for each synthesis is tabulated in table 1.

Seeded gQDs	[CdO]	[ZnO]	[OA]	[ODE]	[DOA]	[CdSe]	'S' precursor	[S]	[c]:[sh]	[M <sup>2+</sup> ]:[S]
S <sub>8</sub> /ODE gQDs	0.085g, (0.67mmol)	0.171g, (2.1mmol)	3.5 ml, (3.118g; 11.04 mmol)	7.6 ml, (6.01g; 24 mmol)	7.5ml, (6g; 24 mmol)	Core-A (0.3 μmol)	S <sub>8</sub> dissolved in ODE (7.5 ml, 6g; 24 mmol)	S <sub>8</sub> (0.088 g (2.76 mmol)	1:9200	1:1
S=TOP gQDs	0.043g, (0.33 mmol)	0.085g, (1.05 mmol)	1.8 ml, (1.559g; 5.52 mmol)	3.8 ml, (3.01g; 12 mmol)	3.8 ml, (3g; 12 mmol)	Core-A (0.15 μmol)	S <sub>8</sub> dissolved in TOP (3 ml, 2.49g; 6.73 mmol)	S <sub>8</sub> (0.044 g (1.38 mmol)	1:9200	1:1
DDT gQDs	0.085g, (0.67mmol)	0.171g, (2.1mmol)	3.5 ml, (3.118g; 11.04 mmol)	7.6 ml, (6.01g; 24 mmol)	7.5ml, (6g; 24 mmol)	Core-B (0.3 μmol)	DDT dissolved in TOP (0.5 ml, 0.416g; 1.12mmol)	DDT (0.7ml, 0.59 g, 2.92 mmol)	1:9200	1:1.05
	*[c]:[sh] = [ CdSe core] : [shell precursor]; [M <sup>2+</sup> ]:[S] =[ cationic precursor] :[ S precursor]									

**Table 3.1:** Molar concentrations of the CdSe core and shell precursors employed in the seeded growth syntheses

For seeded syntheses growth was monitored in each case by sampling aliquots at time  $t = 0.25$  hr i.e. 15 min ( $T_1$ ), 4.5 hr ( $T_2$ ) and 9 hr ( $T_3$ ) respectively, where 'T' denotes time. After annealing for 9 hr the reaction mixture was allowed to cool to room temperature and gQDs purified from excess ligand by multiple chloroform/methanol (1:1) precipitation and toluene redissolution cycles. Finally the purified gQDs were dried and dissolved in toluene.

### 3.2.2.2.3 Control experiments employing Se=TOP as the shell precursor

Control experiment using Se = TOP as the anionic precursor for shell growth on CdSe core –B was performed with a view to investigate if the innate crystal structure of CdSe (W) {as compared to CdS (ZB)} alters the crystallographic evolution of there resulting nanocrystal (CdSe/CdZnSe). For the experiment the molar concentration of [QD] to shell precursors and the ligands were kept exactly identical to S=TOP seeded growth process. Briefly, for the experiment, CdO (0.043 g, 0.33 mmol) and ZnO (0.085 g, 1.05 mmol) was mixed with 11.8 mL (1.559 g, 5.52 mmol) of oleic acid (OA) and 3.8 ml ODE (3.01 g, 12 mmol) in a 50 ml four necked flask and degassed (under vacuum) for 1hr. Following degassing the reaction mixture was heated to 280°C in an inert atmosphere to dissolve CdO and ZnO and form their respective oleates. At this point, 3.8 ml DOA (3 g, 12 mmol kept in glove box), was rapidly injected and temperature of the reaction mixture was decreased to 240 °C. When the temperature stabilized, an injection containing CdSe core (core-B,  $1.5 \times 10^{-7}$  moles) and Se (0.109g, 1.38 mmol) dissolved in 3 ml TOP (2.49 g, 6.73 mmol) (separately prepared in glove box) was rapidly injected to initiate shell growth. The temperature was maintained at 240 °C during annealing for 9 hr. Reaction was sampled at time  $t = 0.25$  hr i.e. 15 min ( $T_1$ ), 4.5 hr ( $T_2$ ) and 9 hr ( $T_3$ ) to probe the reaction progress. The aliquots were subsequently subjected to XRD analysis.

## 3.3 Instrumentation

*UV-Visible Spectrophotometry (UV-Vis):* The UV-Vis measurements were collected on a Varian Cary 100 Bio UV-Vis spectrophotometer between 300-800 nm.

*Photoluminescence Spectroscopy (PL):* The PL emission and excitation measurements were collected on a Fluoromax-4 photon counting spectrofluorometer (Horiba Jobin Yvon). All PL emission and excitation spectra were collected using both wavelength correction of source intensity and detector sensitivity. The excitation wavelength was 400 nm.

*Powder X-ray diffraction (XRD):* XRD was collected using a Bruker AXS D8 ADVANCE powder X-ray diffractometer. To optimize XRD quality and remove artifacts arising from ligand packing and excess ligands, I first precipitated the synthesized gQDs from toluene using a ligand exchange protocol that employs L-histidine.<sup>39</sup> The precipitated gQDs, with L-histidine capping in place of DOA and TOPO, were rinsed gently in ultrapure water, and then vacuum dried on zero diffraction SiO<sub>2</sub> crystal (MTI Corp.).

*Transmission Electron Microscopy (TEM):* TEM measurements were performed on a JEOL 2000EX instrument operated at 100 kV using a tungsten filament at the SUNY-ESF N.C. Brown Center for Ultrastructure Studies.

*High Resolution Transmission Electron Microscopy (TEM) and ED:* The high-resolution TEM (HRTEM) and electron diffraction (ED) analysis was collected on a JEOL JEM2100F field emission TEM operated at 200 kV at the Analytical and Diagnostics Laboratory at State University of New York at Binghamton.

### 3.4 Calculations

#### 3.4.1 Concentration of QDs

The concentration of the QD cores were calculated from UV-Vis optical absorption measurements of the first band edge absorption (1s-1s) intensity using qdot size dependent optical extinction coefficients ( $\epsilon_{\text{qdot}}$ ). First, QD size was correlated to the first absorption wavelength using the calibration methods suggested by Peng and coworkers<sup>40</sup> and Mulvaney and co-workers,<sup>41</sup> and then the QD extinction coefficient ( $\epsilon_{\text{QD}}$ ) was determined. The concentration of qdots was calculated from  $\epsilon_{\text{QD}}$  using the Beer Lamberts law.

#### 3.4.2 Quantum yield (QY) calculations

The QYs were measured by comparing the QD emission with that of a reference Rhodamine 6G (R6G). The R6G was dissolved in EtOH and excited at 488 nm. The PL of the SILAR, was obtained by excitation at 400 nm, in a range of 480 - 750 nm while that for S-TOP, S<sub>8</sub>/ODE and DDT gQDs was obtained by excitation at 500 nm, in a range of 510 - 750 nm.

$$QY_{QD} = QY_R \times \left( \frac{Abs_R}{Abs_{QD}} \right) \left( \frac{PL_{QD}}{PL_R} \right) \left( \frac{\eta_{QD}^2}{\eta_R^2} \right) \dots \dots \dots (1)$$

where, *Abs* is the absorbance measured at the excitation wavelength of the QD and reference (R), *PL* is the integrated area of the fluorescence emission,  $QY_R$  is the QY of the R6G ( $QY = 95\%$ , EtOH),  $\eta_R$  is the refractive index of standard in EtOH ( $\eta = 1.36$ ) and  $\eta_{QD}$  is the refractive index of the QDs in Tl ( $\eta = 1.496$ ). The Abs was kept below 0.1 to limit inner filter effects.

### 3.4.3 Strain calculations along <110> for SILAR gQDs

XRD peak broadening for a sample ( $\beta_{\text{total}}$ ) results from contributions from the finite crystallite size ( $\beta_{\text{Sch}}$ ), strained crystal structure ( $\beta_{\text{Str}}$ ) and broadening due to instrumental error ( $\beta_{\text{Inst}}$ ). Assuming Lorentzian (Cauchy type) function guiding the peak shape, the relation may be stated as,

$$\beta_{\text{total}} = \beta_{\text{Inst}} + \beta_{\text{Sch}} + \beta_{\text{Str}} \dots \dots \dots (1)$$

$$\text{or, } \beta_{\text{total}} - \beta_{\text{Inst}} = \beta_{\text{hkl}} = \beta_{\text{Sch}} + \beta_{\text{Str}} \dots \dots \dots (2)$$

where  $\beta_{\text{hkl}}$  is the peak broadening due to the sample. Assuming the  $\beta_{\text{Inst}}$  remains constant for the samples  $n = 4-22$ , I neglect its contribution for our calculations (as the effective trend would essentially remain the same in either case, even though the actual numeric values would be skewed equally) to compare the peak broadening  $\beta_{\text{hkl}}$  resulting from the crystallite size and strain for the samples  $n = 4-22$ .

Now,  $\beta_{\text{Sch}}$  is calculated (Table 3.2) from the Scherrer equation as,<sup>42,43</sup>

$$\beta_{\text{Sch}} (\text{radians}) = \frac{K\lambda}{D_{\text{eff}} \cos \theta}$$

where,  $K$  = Scherrer constant = 0.9,  $\lambda$  = wavelength of X-ray employed (1.54 Å),  $D_{\text{eff}}$  = volume weighted crystallite size and  $\theta$  is angle of diffraction.

$D_{\text{eff}}$ , the volume weighted average crystallite size, was calculated (Table 3.2) using the equation,

$$D_{\text{eff}} = \sqrt[3]{\frac{6V_P}{\pi}}$$

where  $V_P$  = volume of the particle calculated from the TEM sizes for  $n = 4 - 22$ .

From Eqn. (2)  $\beta_{\text{Str}}$  calculated (Table 1) as  $\beta_{\text{Str}} = \beta_{\text{hkl}} - \beta_{\text{Sch}}$

From Williamson Hall equation,<sup>43,44</sup>  $\beta_{\text{Str}} = 4\epsilon \tan \theta$ , where  $\epsilon$  is the average strain,



Thus,  $\varepsilon = \frac{\beta_{Str}}{4\tan\theta}$ , using this equation, values were calculated for Table 3.2.

gQD	Peak location (2 $\theta$ , degrees)	D <sub>eff</sub> (nm)	$\beta_{Sch}$ (rad)	$\beta_{hkl}$ (rad)	$\beta_{Str}$ (rad)	Strain $\varepsilon$
$n = 4$	43.3	6.41	0.0233	0.0387	0.0154	0.0097
$n = 8$	43.5	8.79	0.0170	0.0286	0.0116	0.0073
$n = 12$	43.9	9.94	0.0150	0.0321	0.0171	0.0106
$n = 18$	44.9	11.11	0.0135	0.0654	0.0520	0.0315
$n = 22$	45.2	14.56	0.0103	0.0743	0.0640	0.0384

**Table 3.2:** showing the calculation of  $\beta_{Sch}$ ,  $\beta_{hkl}$ ,  $\beta_{Str}$  and strain for the gQDs along <110> facet

### 3.5 Results

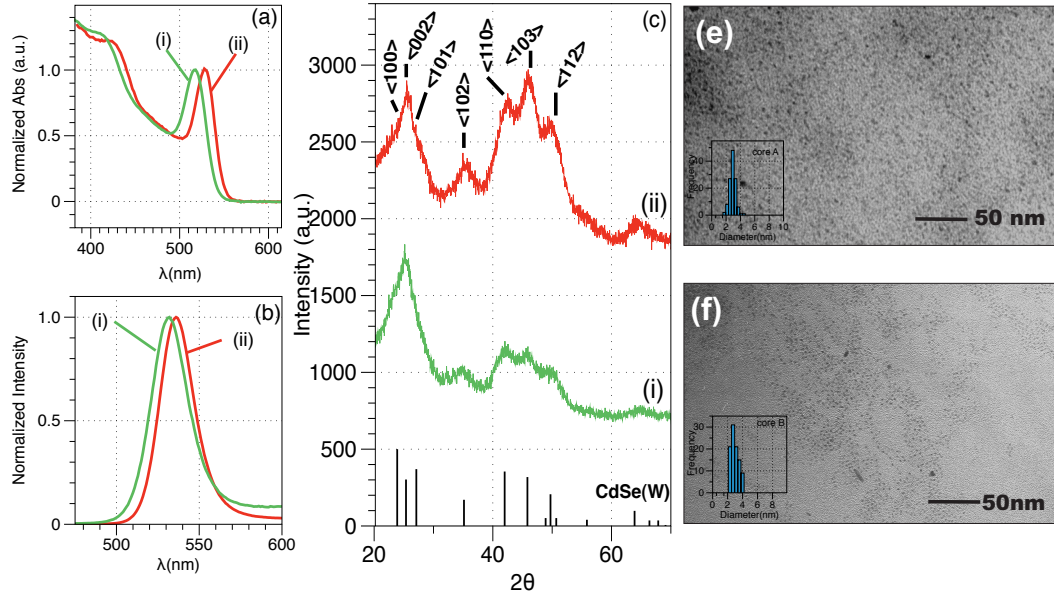


**Figure 3.1:** Representative UV-Vis absorption (a) and the normalized PL emission spectra (b), XRD pattern (c), and TEM micrographs (e) and (f) shown for *W* core-A (i) and core-B (ii) respectively. Corresponding size distribution histograms provided as insets. The CdSe *W* standards are shown as reference.

Fig. 3.1 shows the UV-Vis (a) and normalized PL emission spectra (b) for the *W*-CdSe core – A and core – B. The diameter for core - A was estimated to be  $\sim 2.5$  nm from the Figure 3.1c shows the XRD pattern for the cores. As expected from the synthesis parameters (see methods), both of the synthesized cores are observed to possess *W*-crystal structure, exhibiting peaks resulting from  $\langle 110 \rangle$ ,  $\langle 103 \rangle$ ,  $\langle 112 \rangle$  planes respectively and a broad diffraction in the  $23.0^\circ$ - $27.0^\circ$  region. Importantly, a prominent diffraction at  $\sim 35.0^\circ$  was observed, owing to reflection from  $\langle 102 \rangle$  planes which is typical to a *W* crystal structure and is lacking in ZB. In general, the XRD peaks are broad, due in large part to small grain size of the qdots employed ( $d = 2.5$  nm and  $2.6$  nm), which is probably results in a broad peak is obtained in the  $23$ - $27^\circ$  region, formed by the coalescence of the  $\langle 100 \rangle$ ,  $\langle 002 \rangle$  and  $\langle 101 \rangle$  reflections instead of a well segregated trio of peaks expected in a typical *W* structure. Fig. 3.1e and 3.1f show the TEM micrographs and size distribution histograms (insets) for core- A and core – B respectively. The TEM calculated size was  $2.9 \pm 0.7$  nm (core- A) and  $3.0 \pm 0.5$  nm (core – B) respectively.

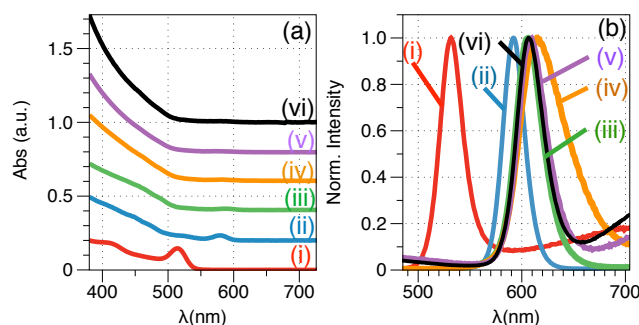


**Figure 3.2:** (a) showing the UV-Vis absorption for *W* core (i),  $n = 4$  (ii), 8 (iii), 12 (iv) and 18 (v) (b) showing the PL emission for core (i),  $n = 4$  (ii), 8 (iii), 12 (iv), 18 (v) and 22 (vi) during shell growth. PL excitation wavelength is 400 nm.

*SILAR gQDs*: UV-Vis (Fig. 3.2a) and PL emission (Fig. 3.2b) monitored shell addition by sampling the synthesis solution after deposition of layers ( $n$ ) at  $n = 4$  - 22 respectively, starting from the core. A rise in absorbance at  $< 500$  nm and decreasing core signature in

the absorption spectra indicates CdZnS deposition. Interestingly, the core signature in the absorption spectra at  $n = 4$  stage is observed to be redshifted ( $\sim 65$  nm) due to ripening of the core and extensive delocalization of the exciton resulting from band gap alteration from CdS shell deposition the CdSe core interface.<sup>45–47</sup> A monotonous red-shift in  $\lambda_{PL}$  with increasing  $n$  was observed (Fig 3.3a), supporting CdZnS shell deposition; while QY% was observed to increase initially ( $n = 4$ ) and then decrease with increasing shell layers probably resulting from defect states introduced inside the strained thick shell by the alloy gradient employed (Fig. 3.3b).

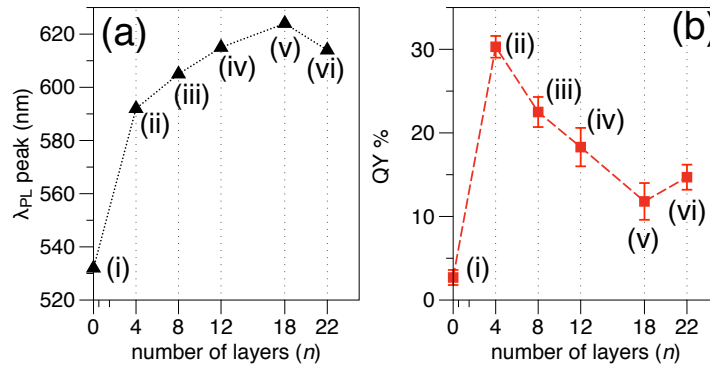


**Figure 3.3:** (a) showing the redshift in PL emission peak  $\lambda_{PL}$  and (b) the variation in QY% with increasing in shell layers ( $n$ ) starting from the core (i) ( $\lambda_{PL} = 532$  nm; QY% =  $2.7 \pm 0.9\%$ ), to  $n = 4$  (ii) ( $\lambda_{PL} = 592$  nm; QY% =  $30.3 \pm 1.3\%$ ), 8 (iii) ( $\lambda_{PL} = 605$  nm; QY% =  $22.5 \pm 1.8\%$ ), 12 (iv) ( $\lambda_{PL} = 615$  nm; QY% =  $18.3 \pm 2.3\%$ ), 18 (v) ( $\lambda_{PL} = 624$  nm; QY% =  $11.8 \pm 2.2\%$ ) and 22 (vi) ( $\lambda_{PL} = 614$  nm; QY% =  $14.7 \pm 1.5\%$ ) during growth of gQDs. PL excitation wavelength is 400 nm.

Powder XRD analysis provided insight into the nature and extent of crystallographic changes. Figure 3.4a shows the XRD patterns at  $n = 4$  (ii), 8 (iii), 12 (iv), 18 (v) and 22 (vi). Starting from the core-A (Fig 3.4a - i), the gQDs exhibit a continued  $W$  type growth pattern at each stage, showing the characteristic reflections typical to  $W$ -type crystal (see insets). This structure more closely resembles the  $W$ -CdS compared to  $W$ -ZnS structure, which can be explained considering the fact the shell growth was initialised using the  $Cd_{0.87}Zn_{0.13}$  precursor feed ratio. The  $\langle 002 \rangle$  reflection intensity was

observed to be most intense throughout the synthesis, indicating extended crystalline domain in that direction (anisotropic growth).<sup>48</sup>

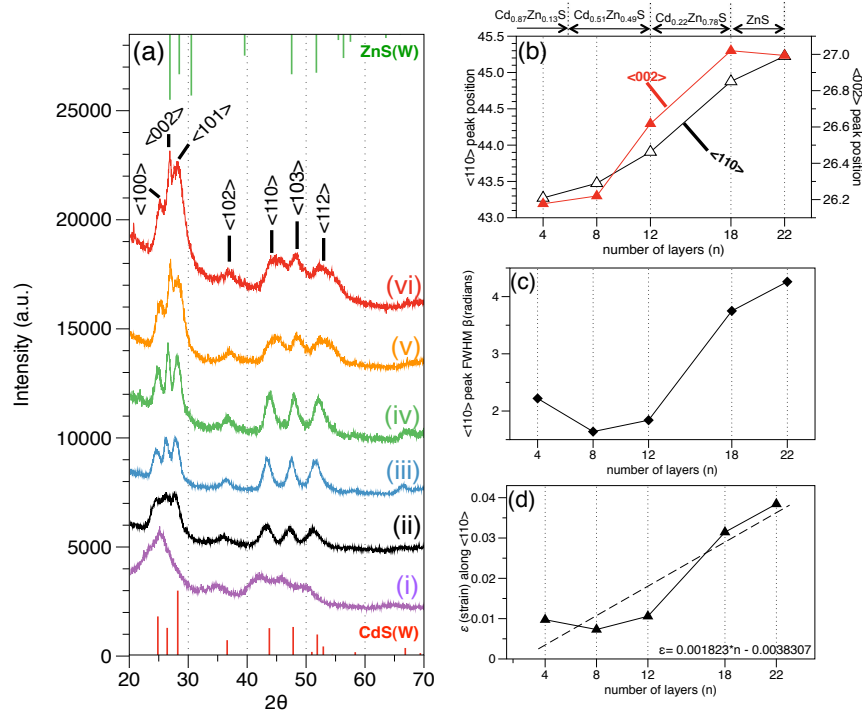


**Figure 3.4:** (a) The powder XRD patterns for shell growth at *W*-cores at shell layers (*n*) of 4 (ii), 8 (iii), 12 (iv), 18 (v) and 22 (vi), (b) <110> and <002> peak shift during gQD growth, (c) FWHM variation of <110> peak and (d) increasing lattice strain ( $\epsilon$ ) calculated along <110> with increasing shell layers are shown. The XRD pattern for CdS (*W*) and ZnS (*W*) standards are provided for reference.

Fig. 3.4b shows the systematic shift of <110> and <002> peak reflections to higher 2θ with increasing *n* confirming Zn-rich alloy deposition at later layers. Fig 3.4(b) further elucidates that the rate of change of alloy composition varies across the lateral (<110>) and vertical (<002>) facets of the growing gQD nanorods, suggesting the existence of composition gradient across the shell.

Interestingly, though TEM depicts continual nanocrystal growth with *n*, the FWHM ( $\beta$ ) of <110> peak is observed to increase from *n* = 8 – 22 (Fig 3.4c), in a somewhat counterintuitive manner to Scherrer predicted peak narrowing due to increasing grain size. The observed increase in FWHM results from the increased

contribution ( $\beta_{\text{Str}}$ ) of the average lattice strain  $\epsilon$  towards peak broadening ( $\beta$ ) as a result of the alloy gradient employed for shell growth (See Sec. 3.4.3). Fig 3.4(d) exhibits that the average lattice strain calculated along  $\langle 110 \rangle$  by William - Hall equation,<sup>43,44,49,50</sup> increases with progression of shell deposition. A closer look at the crystalline evolution shows that the  $\langle 100 \rangle$ ,  $\langle 101 \rangle$ ,  $\langle 110 \rangle$  and  $\langle 112 \rangle$  peak broadening becomes clearly apparent at  $n = 18$  and  $22$ . This broadening most probably results from the increasing non-uniform residual strain (Fig 3.4d) in individual gQDs, arising from deposition of isolated domains of ZnS rich alloy shell at specific facets at higher  $n$  (see TEM discussion). The facet selective deposition of ZnS rich alloy islands results in composition difference amongst the individual grains constituting a single gQD and also amongst small domains belonging to the same grain. This leads to non-uniform residual microstress to develop along the grain boundaries leading to strained nanocrystals. Coalescence of the closely spaced X-ray diffraction peaks resulting from compositionally disparate domains in a single gQD appears as a single peak reflection with increased fwhm in the XRD, previously reported in case of strained bulk metallic crystals.<sup>51</sup>

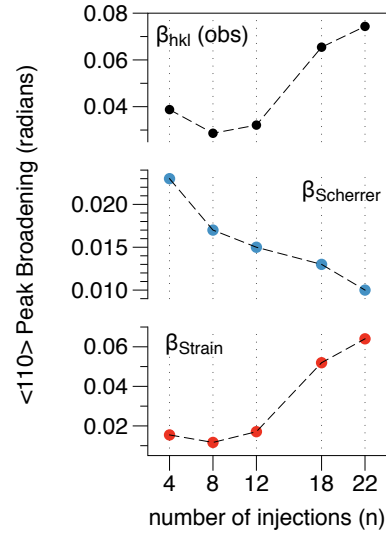


**Figure 3.5:** showing the trend in variation of  $\beta_{hkl}$ ,  $\beta_{Sch}$  and  $\beta_{Str}$  with increasing size of gQDs.

Fig 3.5 shows the trends in variation of  $\beta_{hkl}$ ,  $\beta_{Sch}$  and  $\beta_{Str}$  with progression in shell growth. It is observed, from  $n = 4 - 8$ ,  $\beta_{hkl}$  and  $\beta_{Sch}$  decrease, indicating  $\beta_{Sch}$  is the dominating factor at this stage. Further, from  $n = 4 - 8$ ,  $\beta_{Str}$  is found to decrease which might be related to the change of shape of the gQD from a spheroidal to an ovoid, also the alloy composition employed for shell growth ( $\text{Cd}_{0.87}\text{Zn}_{0.13}\text{S}$ ) is biased towards CdS, which has little (3.9%) mismatch with the core resulting in lesser strain. From  $n = 8 - 22$   $\beta_{hkl}$  and  $\beta_{Str}$  are found to increase monotonically with gQD growth even though  $\beta_{Sch}$  keeps on decreasing. This indicates,  $\beta_{Str}$  is the dominating factor in peak broadening from  $n = 8 - 22$  as the alloy gradient (progressively getting biased towards ZnS) employed leads to a strained crystal.

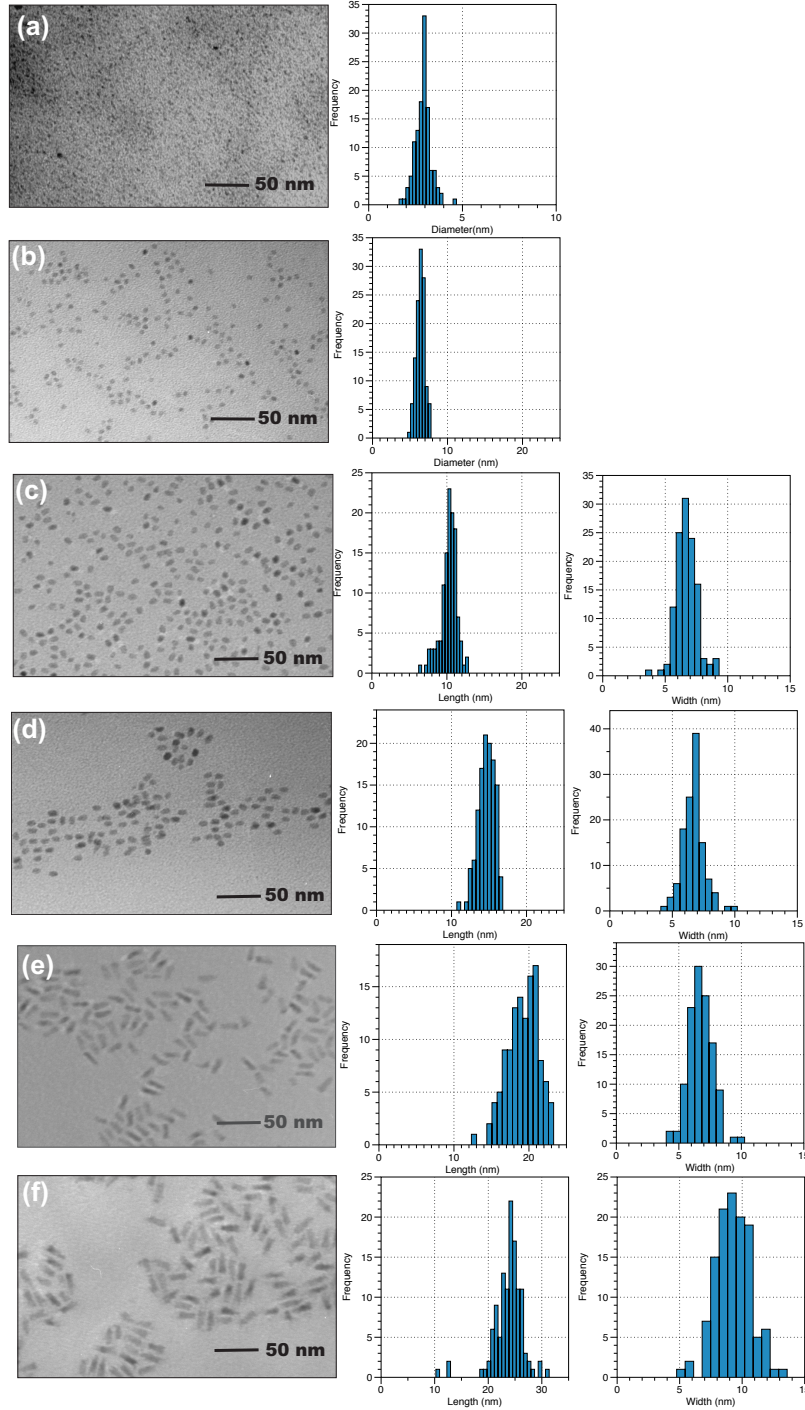


**Figure 3.6:** Representative TEM micrographs of the  $W$ -core ( $d = 2.9 \pm 0.4$  nm) (a), and gQD at shell growth layers of  $n = 4$  ( $d = 6.4 \pm 0.6$  nm) (b), 8 ( $l = 10.1 \pm 1.1$  nm,  $w = 6.7 \pm 0.8$  nm,  $l/w = 1.5 \pm 1.4$ ) (c), 12 ( $l = 14.6 \pm 1.1$  nm,  $w = 6.7 \pm 0.9$  nm,  $l/w = 2.2 \pm 1.2$ ) (d), 18 ( $l = 19.2 \pm 2.1$  nm,  $w = 6.9 \pm 0.9$  nm,  $l/w = 2.8 \pm 1.3$ ) (e) and 22 ( $l = 23.8 \pm 2.8$  nm,  $w = 9.3 \pm 1.4$  nm,  $l/w = 2.59$ ) (f). Corresponding size distribution histograms are provided.

The morphological evolution of SILAR gQDs was monitored by TEM (Fig. 3.6).

It was observed that the size increased in an anisotropic manner with  $n$ , resulting in rod

morphology. For example, compared to core - A, at  $n = 4$  the gQDs were spheroidal, the evolution of the ellipsoidal shape becoming evident at  $n = 8$  and  $n = 12$ . Finally at  $n = 18$  the gQDs is observed to possess rod morphology, a trend which continues for  $n = 22$ . From the growth pattern of the gQDs as seen from the TEM it is imperative that the preferred growth direction was along the  $\langle 002 \rangle$  direction (c axis) which constitutes the long axis of the rod.<sup>48</sup> Marginal increase in polydispersity of the sample is observed with the progression of shell growth, though size distribution histograms retain a simple Gaussian distribution character. A closer look at the TEM micrographs at  $n = 18, 22$  (Fig. 3.6 e and f) reveal growth of irregular minute lumps at certain facets towards the ends of the rods, and the overall surface of the rod looks rough, imparting a ‘dog bone’ shape. Such irregular growth regions is predicted to result from two factors. First, since the amount of precursor addition was continued at this stage with a spherical model in calculation, inadequate amount of precursors resulted in non-uniform layering on the surface gQDs. Further annealing of the sub monolayers, at the shell growth temperature leads to ripening and coalescence into small isolated islands at certain high-energy facets towards the end of the rod, observed in the TEM. Secondly, the shell precursor alloy feed ratio employed at higher  $n$  ( $\text{Cd}_{0.22}\text{Zn}_{0.78}$ -oleate for  $n = 12$ -18 and Zn – oleate for  $n = 18 - 22$ ) are predominantly rich in Zn, requiring epitaxial layering with ZnS which has considerable lattice mismatch with prior deposited shell layers primarily consisting of CdS ( $\sim 7\%$ ).<sup>52</sup> This results in the development of considerable amount of residual localized microstress amongst the constituent grains of gQDs shell interface. Non-uniform layering of the shell interface results from growth of isolated pockets of Zn –



rich domains at selected facets.<sup>48</sup> Hence, TEM findings were found to correlate well with the peak broadening observed in the XRD at these stages, suggesting a strained structure.

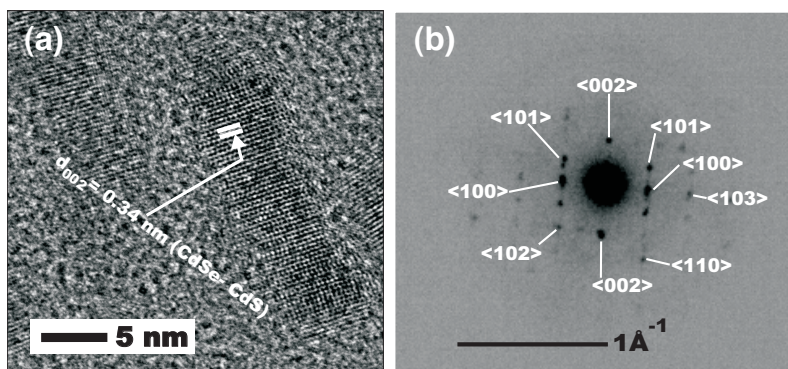


**Figure 3.7:** HRTEM micrograph of SILAR gQDs at  $n = 22$  (a) The corresponding ED pattern is provided (b). The diffraction spots resulting from lattice planes typical of a  $W$  crystal are shown.

HRTEM and ED techniques were used to investigate the morphology and crystallinity of the SILAR gQDs. Fig. 3.7a shows HRTEM micrograph of the SILAR gQDs at  $n = 22$  stage, which reveals high degree of crystallinity in its structure. The lattice spacing intermediate to  $\langle 002 \rangle$  of  $W$ -CdSe and  $\langle 002 \rangle$  of  $W$ -CdS is shown in Fig. 3.4a, which corroborates the XRD conclusion that the SILAR gQDs shell composition was biased towards  $W$ -CdS. The extended  $\langle 002 \rangle$  domain along the length of the rod confirms  $\langle 002 \rangle$  to be the preferred direction of anisotropic growth. The corresponding ED pattern provided in Fig. 3.4b shows the single crystalline structure of the SILAR gQDs. Analysis identified the diffraction spots resulting from the  $\langle 100 \rangle$ ,  $\langle 002 \rangle$ ,  $\langle 101 \rangle$ ,  $\langle 102 \rangle$ ,  $\langle 110 \rangle$  and  $\langle 103 \rangle$  lattice planes. Sharp diffraction spots also indicated a high degree of crystallinity.

Following the growth of gQDs by SILAR method, I wished to investigate how does available concentration of shell precursor monomers affect gQD growth. To achieve that, I introduced the entire concentration of S shell precursor ( $S_8/ODE$ ) used in the SILAR process + CdSe core, into the reaction medium containing the entire

concentration of cationic shell precursors (Cd/Zn-oleate) maintained at 240°C in a swift single injection step (seeded growth) and annealed for 9 hr. By employing identical set of ligands, shell growth temperature (240°C), and annealing time frame (9 hr) as well as maintaining identical molar concentration ratios of CdSe core, shell precursors and ligands, the essential difference between the two synthetic procedures SILAR (low rate of precursor infusion) and *seeded* (high rate of precursor infusion) was the available concentration of shell precursor monomers in the reaction medium. Further, I wished to investigate if alteration of the source of ‘S’ shell precursors during seeded growth influences the gQD growth pattern in a significant manner. For this study, two different sources of ‘S’ shell precursors i.e. S<sub>8</sub> in trioctylphosphine (S=TOP) and dodecanethiol (DDT) were employed in place of S<sub>8</sub>/ODE during seeded growth keeping rest of the reaction variables identical. The growth of gQDs by the seeded growth process, starting from *W*-cores ( $T_0$ , at  $t = 0$  hr), was monitored by sampling the synthesis solution at time intervals of  $t = 0.25$  hr i.e. 15 min ( $T_1$ ), 4.5 hr ( $T_2$ ) and 9 hr ( $T_3$ ) respectively, where ‘ $T$ ’ denotes time.

*Seeded gQDs*: Fig 3.8 (See supporting info) shows the UV-vis spectra for seeded shell growth using S<sub>8</sub>/ODE (a), S=TOP (c) and DDT (e) as sulfur precursors respectively. Analogous to the SILAR shell growth process described above, a steep rise in absorption in the high-energy regime (<500 nm), and a decreasing core signature in the absorption spectra indicating a CdZnS shell deposition is observed in each case. Fig. 3.8 also shows the photoluminescence (PL) spectral change during the shell growth procedure using

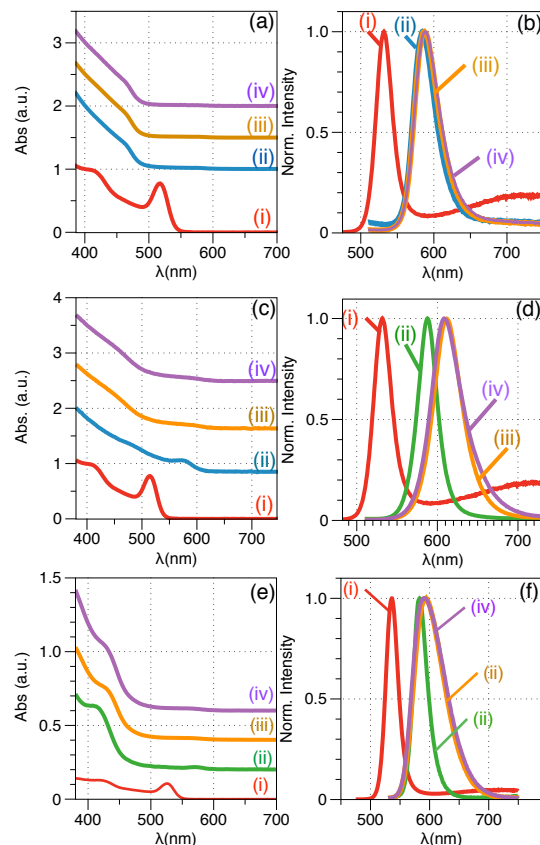


**Figure 3.8:** UV-vis and PL spectra shown for S<sub>8</sub>/ODE (a, b) S-TOP (c, d) and DDT (e, f) gQDs at core (i), T<sub>1</sub> (ii), T<sub>2</sub> (iii) and T<sub>3</sub> (iv).

S<sub>8</sub>/ODE (b), S=TOP (d) and DDT (f) respectively. Gradual redshift in the  $\lambda_{\text{PL}}$  with increasing growth time (shell thickness) is observed, for each of the seeded growth process consistent with a CdZnS shell deposition in each case. Fig 3.9 shows the trend of the  $\lambda_{\text{PL}}$  shift (a), QY% (b) and diameter change (c) with increasing growth time in case of S<sub>8</sub>/ODE, S=TOP and DDT mediated seeded growth process. As observed from Fig. 3.9(a) for S<sub>8</sub>/ODE mediated shell growth,  $\lambda_{\text{PL}}$  shifts from 532 nm ( $T_0$ , core), to 587 nm ( $T_1$ ) and remains stationary at that value for  $T_2$  and  $T_3$ , till the conclusion of reaction.  $\lambda_{\text{PL}}$  is observed to shift from 532 nm ( $T_0$ ), to 588 nm ( $T_1$ ), 612 nm ( $T_2$ ) and finally 608 nm ( $T_3$ ) for S=TOP gQDs. The minute blueshift observed at  $t = 4.5$  hr to  $t = 9$  hr, is predicted

to result from the increased incorporation of ZnS onto the shell, which results in lattice contraction, and in turn alters the band gap alignment of the shell. For DDT gQD (Fig. 3.9a),  $\lambda_{PL}$  shifts from 536 nm ( $T_0$ , core), to 584 nm ( $T_1$ ), to 594 nm ( $T_2$ ) and finally marginally to 591 nm ( $T_3$ ), till the conclusion of reaction. From Fig. 3.9b, the QY % for S<sub>8</sub>/ODE gQDs was found to stagnate at  $20 \pm 1.8$  % for  $T_1$ ,  $T_2$  and  $T_3$ . The QY % for S=TOP gQDs was observed to be  $26.5 \pm 0.4$  % ( $T_1$ ),  $52.4 \pm 2.1$  % ( $T_2$ ) and  $53.8 \pm 2.4$

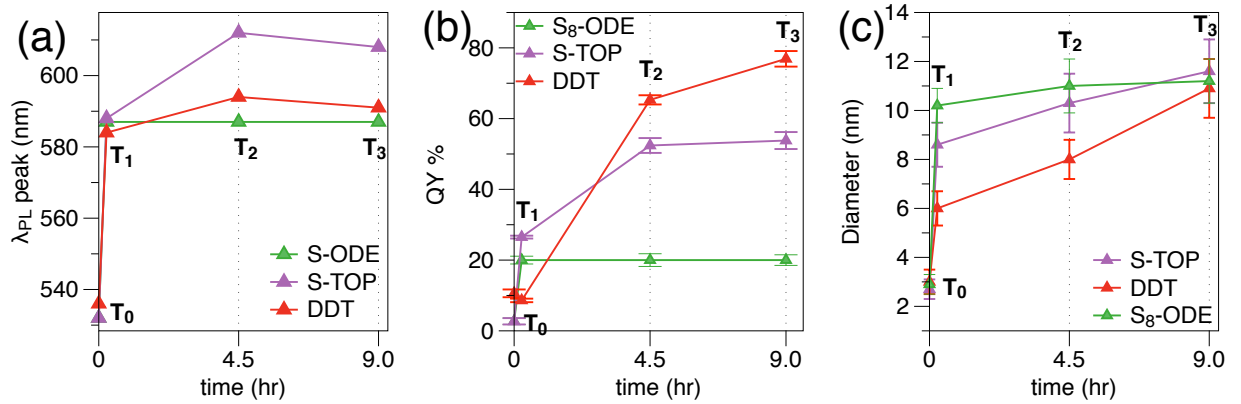
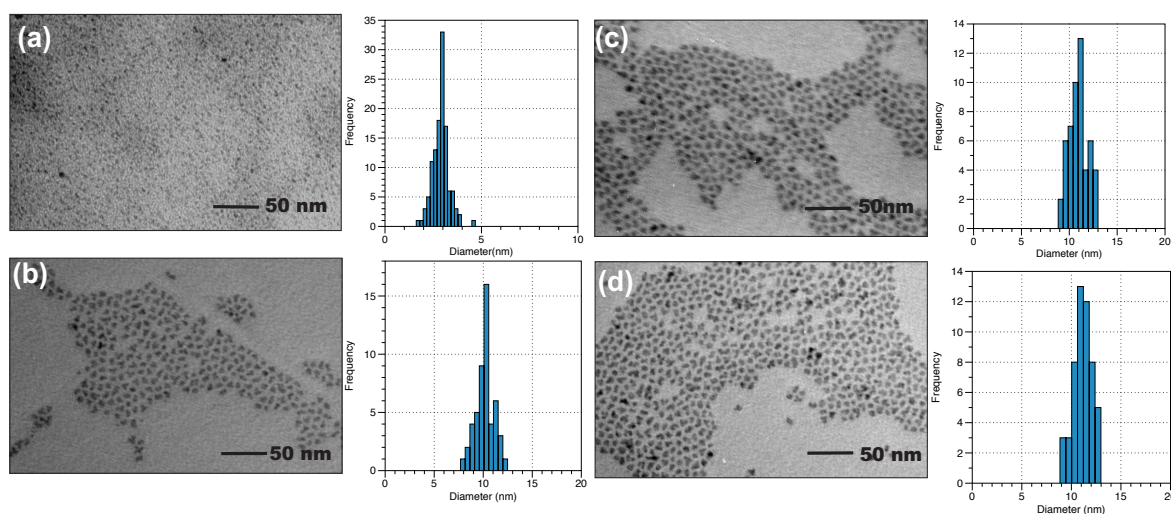


**Figure 3.9:** Figure showing temporal evolution of  $\lambda_{PL}$  shift (a), QY% variation (b), and diameter change (c) at  $T_1$ ,  $T_2$ , and  $T_3$  for gQD growth at  $W$ -core ( $T_0$ ) employing S<sub>8</sub>/ODE, S=TOP and DDT shell precursors. PL excitation carried out at 500 nm.

( $T_3$ ). DDT gQDs were observed to possess, QY % of  $8.6 \pm 0.5$  % ( $T_1$ )  $65.3 \pm 1.3$  % ( $T_2$ ) and  $76.9 \pm 2.2$  % ( $T_3$ ). Fig. 3.9 (c) summarizes the variation in gQD diameter with time as calculated from the TEM micrographs of S<sub>8</sub>/ODE (Fig 3.10), S=TOP (Fig. 3.11) and DDT (Fig. 3.12) gQDs. In general, a monotonous increase in diameter ‘ $d$ ’ with increasing growth time, is observed. Interestingly, the growth trends exhibited on Fig. 3.9c show that though the seeded growth gQDs using disparate precursors resulted in comparable final sizes ( $\sim 10$  nm),  $\lambda_{PL}$  shift associated in each case is quite different, despite identical molar concentration of precursors. I believe the cause of such disparity is two fold. Firstly, the shapes of the final seeded gQDs are different, which alters band gap

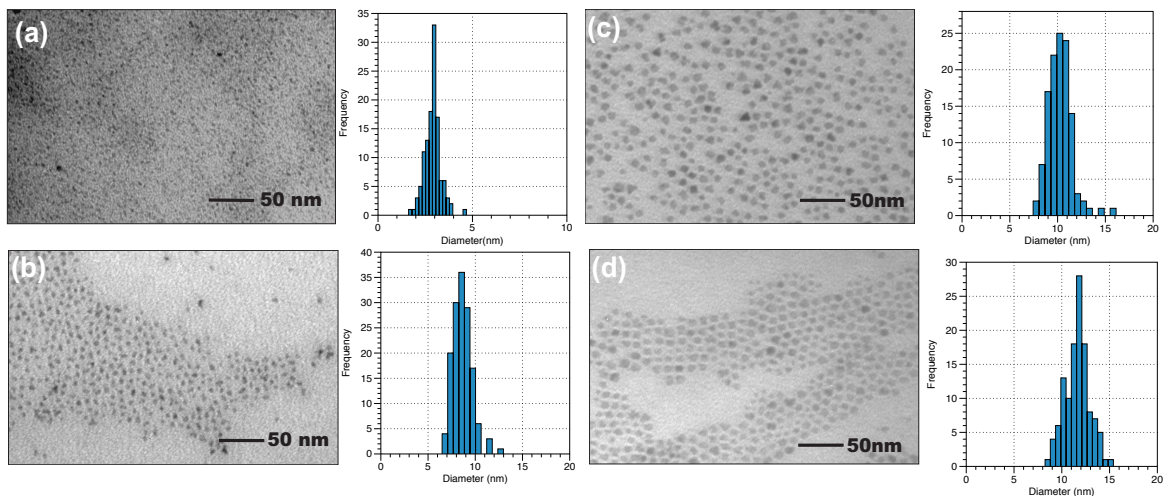
orientation, resulting in differential confinement of the exciton in each case.<sup>53,54</sup> Secondly relative reactivities of the cationic oleates vary with the different ‘S’ shell precursors, resulting in altered alloy composition in the sequential layering process during CdZnS seeded shell growth. This again affects the band gap structure, leading to disparity in the extent of exciton delocalization in the shell.

Fig. 3.10 shows the TEM micrographs for the S<sub>8</sub>/ODE gQDs. Interestingly, each of the samples  $T_1$  (a),  $T_2$  (b) and  $T_3$  (c) exhibit multipodal morphology of the gQDs, tripodal being a majority.



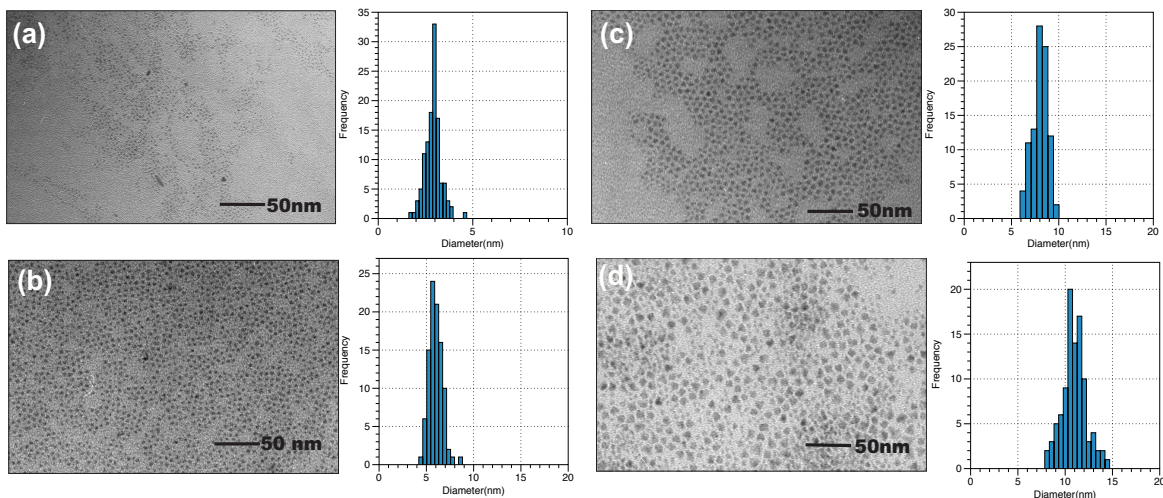
**Figure 3.10:** Representative TEM micrographs and size distribution of the  $W$ -core  $T_0$  ( $d = 2.9 \pm 0.4$  nm) (a), and S<sub>8</sub>/ODE gQD at  $T_1$  ( $d = 10.2 \pm 0.9$  nm) (b),  $T_2$  ( $d = 11 \pm 0.9$  nm) (c), and  $T_3$  ( $d = 11.2 \pm 0.9$  nm) (d). Corresponding size distribution histograms are provided.

Fig. 3.11 exhibits the morphological evolution of the S=TOP gQDs. Increasing size of gQD with elapsed time is observed with marginal increase in polydispersity.



**Figure 3.11:** Representative TEM micrographs and size distribution of the  $W$ -core  $T_0$  ( $d = 2.9 \pm 0.4$  nm) (i), and S=TOP gQD at  $T_1$  ( $d = 8.6 \pm 0.9$  nm) (ii),  $T_2$  ( $d = 10.3 \pm 1.2$  nm) (iii), and  $T_3$  ( $d = 11.6 \pm 1.3$  nm) (iv). Corresponding size distribution histograms are provided.

Interesting morphology evolution is revealed on a closer look at the TEM micrographs: symmetrical core shell structures with irregular faceted periphery (no distinct shapes) is observed for  $T_1$  (a), a symmetrical multifaceted structure, roughly triangular shape is observed for  $T_2$  (b) while prominent trigonal morphology is observed at  $T_3$  (d) (Fig. 3.11).



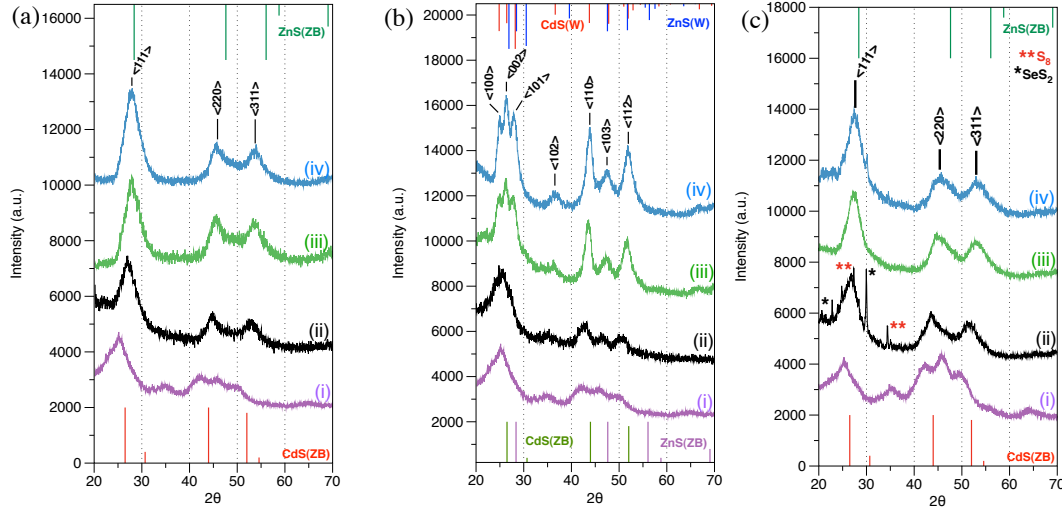
**Figure 3.12:** Representative TEM micrographs and size distribution of the  $W$ -core  $T_0$  ( $d = 3.0 \pm 0.5$  nm) (a), and DDT gQDs at  $T_1$  ( $d = 6.0 \pm 0.7$  nm) (b),  $T_2$  ( $d = 8.0 \pm 0.8$  nm) (c), and  $T_3$  ( $d = 10.9 \pm 1.2$  nm) (d). Corresponding size distribution histograms are provided.

Fig. 3.12 shows the TEM micrographs for DDT gQDs. The diameter of the gQDs is seen to monotonously increase with increasing growth time. TEM micrographs (Fig. 3.12-b, c and d) reveal multifaceted polyhedral morphology for each of the  $T_2$ ,  $T_3$  and  $T_4$  samples.

Crystalline evolution of the gQDs synthesized by seeded procedure is shown in Fig. 3.13. The crystallographic evolution of S<sub>8</sub>/ODE gQDs at  $T_0$  (core) (i),  $T_1$  (ii),  $T_2$  (iii) and  $T_3$  (iv) is shown in Fig 3.13a. Interestingly, it is observed that starting from a *W* core – A (Fig. 3.13a-i), unlike the SILAR gQD case, the shell growth proceeds in a pure *ZB* type growth pattern at each stage (Fig. 3.13a-ii, iii and iv) exhibiting the characteristic  $\langle 111 \rangle$ ,  $\langle 220 \rangle$ , and  $\langle 311 \rangle$  reflections typical of *ZB* - type crystal. A systematic shift towards higher  $2\theta$  values with elapsing time indicates increasing incorporation of Zn-rich alloy shell material at later stages. The diffraction pattern for the S=TOP gQDs (Fig. 3.13b) is shown for  $T_0$  (core) (i),  $T_1$  (ii),  $T_2$  (iii) and  $T_3$  (iv). Starting from the *W* core -A (Fig 3.13b - i), a continued *W* type growth pattern at each stage is indicated showing the characteristic  $\langle 100 \rangle$ ,  $\langle 002 \rangle$ ,  $\langle 101 \rangle$ ,  $\langle 102 \rangle$ ,  $\langle 110 \rangle$ ,  $\langle 103 \rangle$  and  $\langle 112 \rangle$  reflections typical to *W* - type crystal, more closely resembling the *W*-CdS,(See insets). A systematic shift towards higher  $2\theta$  values with elapsing time indicates increasing incorporation of Zn-rich alloy shell material at later stages, as the growth of gQDs progresses. Such a trend of gradual shift might appear counterintuitive at first, considering the fact that not only both Cd, Zn cationic shell precursors are present in the system from the initial stages of shell growth, but also [Zn]: [Cd] molar ratio is of the order of 3:1. It can be postulated that in spite of the higher concentration of [Zn] precursor in the solution, the system exhibits propensity towards the incorporation of a CdS interim ‘wetting layer’ between the CdSe core and a ZnS shell owing to lattice parameter compatibility (CdSe-CdS). Such a



phenomenon termed ‘spontaneous interfacial segregation’ for coherent epitaxial growth in the case of colloidal core/shell nanocrystal has been reported earlier.<sup>48</sup>



**Figure 3.13:** The powder XRD results for shell growth at *W*-cores at  $T_1$  (ii),  $T_2$  (iii), and  $T_3$  (iv). The XRD pattern for the *W* CdSe core  $T_0$  (i), CdS (*W*) and ZnS (*W*) standards are provided for reference.

The increased narrowing of peak reflections at each subsequent stage indicates the increasing grain size, or in other words growth of the gQDs.

A careful inspection of the XRD patterns of samples reveals that the  $\langle 002 \rangle$ ,  $\langle 110 \rangle$  and  $\langle 112 \rangle$  reflections are exceptionally prominent comparing with the standards (see insets, Fig. 3.13b). Furthermore, the TEM observations (Fig. 3.11) show an isotropic manner of growth in case of S=TOP gQDs. These XRD observations can thus be interpreted to depict the growth of polytypic nanocrystals, as discussed in our previous work.<sup>36</sup> In such polytypic biphasic nanocrystals, *ZB* crystal domains are found to grow in an otherwise preferred *W*- type crystal shell growth, arising a result of stacking faults and long term annealing, in which the *W*  $\langle 002 \rangle$ ,  $\langle 110 \rangle$  and  $\langle 112 \rangle$  peak reflections are reinforced by the  $\langle 111 \rangle$ ,  $\langle 220 \rangle$  and  $\langle 311 \rangle$  peak reflections from the coexisting *ZB* domains resulting in unnaturally prominent peaks. Fig 3.13c depicts the crystallographic evolution of DDT gQDs at  $T_0$  (core) (i),  $T_1$  (ii),  $T_2$  (iii) and  $T_3$  (iv). It is observed that



starting from a *W* core (Fig. Fig 3.13c-i), analogous to S<sub>8</sub>/ODE gQDs, the shell growth proceeds in a pure *ZB* type growth pattern at each stage (Fig. Fig 3.13c-ii, iii and iv). Additional four sharp peaks, which matches up well with SeS<sub>2</sub> (black asterisk), and elemental sulfur (red asterisk) are observed in *T*<sub>1</sub>. This can be attributed to submicron-sized particles probably resulting from the side reaction of DDT with etched CdSe core prior to shell deposition, which were not fully removed during postsynthetic purification. These products in the reaction medium, arising briefly after DDT+ core rapid injection, evidenced by an increased opacity of the growth solution, probably get incorporated into the shell in the later stages of growth, since the reaction solution turns back to being clear, transparent at time  $\sim t = 1$  hr and remains so for rest of the synthesis. Also, the peak reflections are observed to disappear at *T*<sub>2</sub> (Fig 3.13c-iii) and *T*<sub>3</sub> (Fig 3.13c-iv).

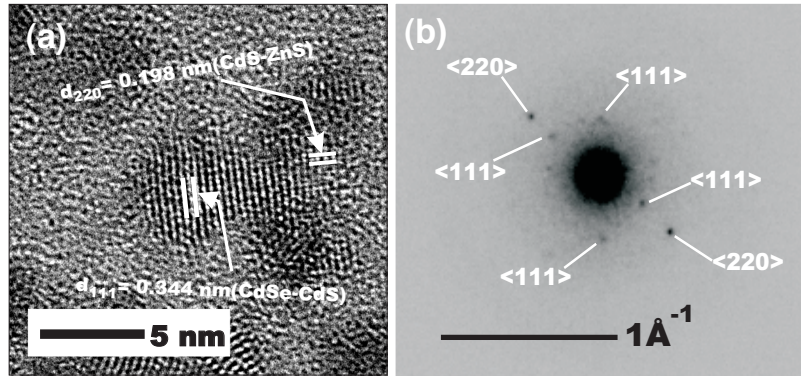
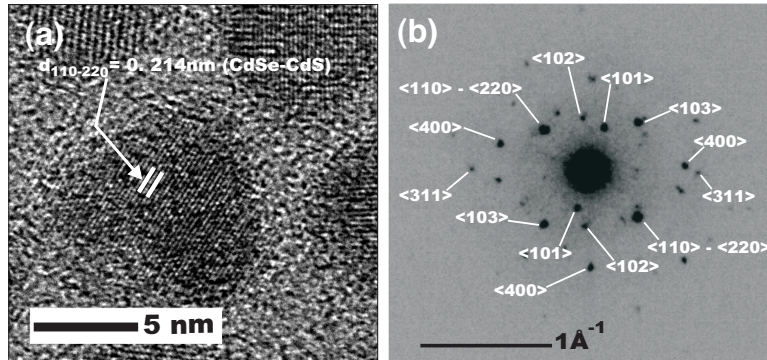


**Figure 3.14:** (a) HRTEM micrograph of S<sub>8</sub>/ODE gQDs at *T*<sub>3</sub> (9 hr) stage and (b) The corresponding ED pattern is provided. Diffraction spots resulting from lattice planes typical to *ZB* crystal structure are observed.

HRTEM and ED techniques were used to investigate the morphology and crystallinity of the S<sub>8</sub>/ODE, S=TOP and DDT gQDs. Fig. 3.14(a) shows the HRTEM micrograph for S<sub>8</sub>/ODE gQDs at *T*<sub>3</sub>. Majorities of the gQDs possess tripodal morphology. The calculated lattice spacings shown in Fig. Fig. 3.14(a) are consistent with  $\langle 111 \rangle$

lattice planes of *ZB*-CdS-ZnS and  $\langle 220 \rangle$  lattice planes of *ZB*-CdS-ZnS supporting the XRD conclusions of the pure *ZB* nature of the gQDs. The corresponding ED pattern shown in Fig. 3.14(b) exhibits diffraction spots arising from  $\langle 111 \rangle$  and  $\langle 220 \rangle$  lattice planes typical for a pure *ZB* crystal pattern, thereby underlining the monophasic single crystalline nature for the gQDs.

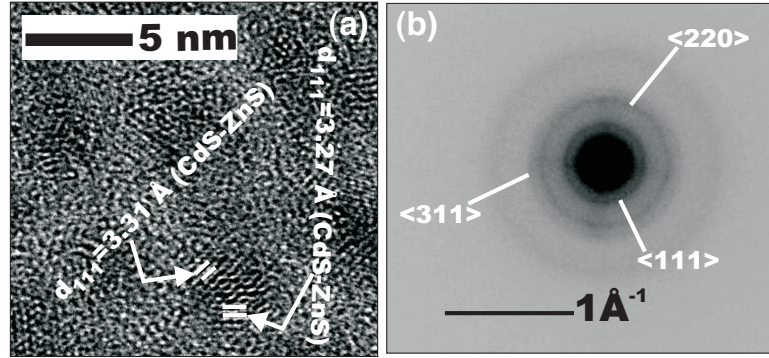
Fig. 3.15(a) shows the HRTEM micrograph of the S=TOP gQDs at  $T_3$  (9 hr) stage. The corresponding ED pattern is provided in Fig. 3.15(b). The high degree of crystallinity of the sample is observed from the HRTEM micrographs where, the stacking of the planes in the gQD is visible devoid of any diffuse amorphous regions. The morphology of the S=TOP gQDs are revealed to be symmetric trigonal planar as concluded from XRD, low resolution TEM investigations. The lattice spacing consistent with either  $\langle 110 \rangle$  *W*-CdSe-CdS or  $\langle 110 \rangle$  *W*-CdSe and  $\langle 220 \rangle$  *ZB*-CdS are observed (Fig. 3.15a), which are difficult to differentiate owing to identical lattice spacings.



**Figure 3.15:** (a) HRTEM micrograph of S=TOP gQDs at  $T_3$  (9 hr) stage. (b) The corresponding ED pattern is provided. Diffraction spots resulting from lattice planes typical to both *W* and *ZB* crystal structure are observed.

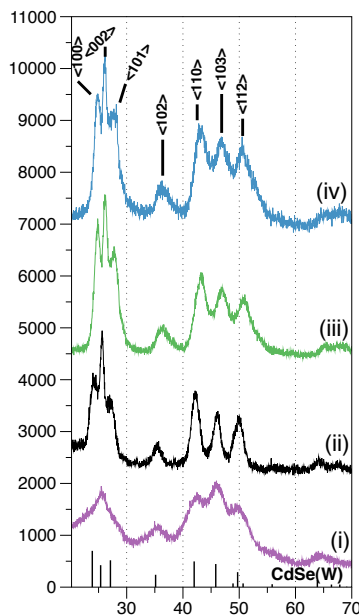
The XRD findings suggest the S=TOP gQDs possess a polytypic crystalline character resulting from the co-existence of both *W* and *ZB* domains in a single nanocrystal. Evidence of polytypic character is obtained from the corresponding ED pattern provided

in Fig. 3.15(b), where diffraction spots resulting from the  $\langle 102 \rangle$ ,  $\langle 110 \rangle$  and  $\langle 103 \rangle$  lattice planes (consistent with *W*- CdS-ZnS) and  $\langle 220 \rangle$ ,  $\langle 311 \rangle$  and  $\langle 400 \rangle$  lattice planes (consistent with *ZB* - CdS -ZnS) are observed.



**Figure 3.16:** (a) HRTEM micrograph of DDT gQDs at  $T_3$  (9 hr) stage, (b) the corresponding ED pattern is provided. Debye rings due to diffraction spots from identical lattice planes typical to *ZB* crystal structure are observed.

Fig. 3.16 (a) shows the HRTEM micrograph for DDT gQDs at  $T_3$ . Majorities of the gQDs possess polyhedral morphology. The calculated lattice spacings shown in Fig. 3.16 (a) are consistent with  $\langle 111 \rangle$  lattice planes of *ZB*-CdS-ZnS supporting the XRD conclusions of the pure *ZB* nature of the gQDs. The corresponding ED pattern shown in Fig. 3.16 (b) exhibits the Debye rings resulting from diffraction spots resulting from  $\langle 111 \rangle$ ,  $\langle 220 \rangle$  and  $\langle 311 \rangle$  lattice planes typical for a pure *ZB* crystal pattern are seen thereby underlining the monophasic single crystalline nature for the gQDs.



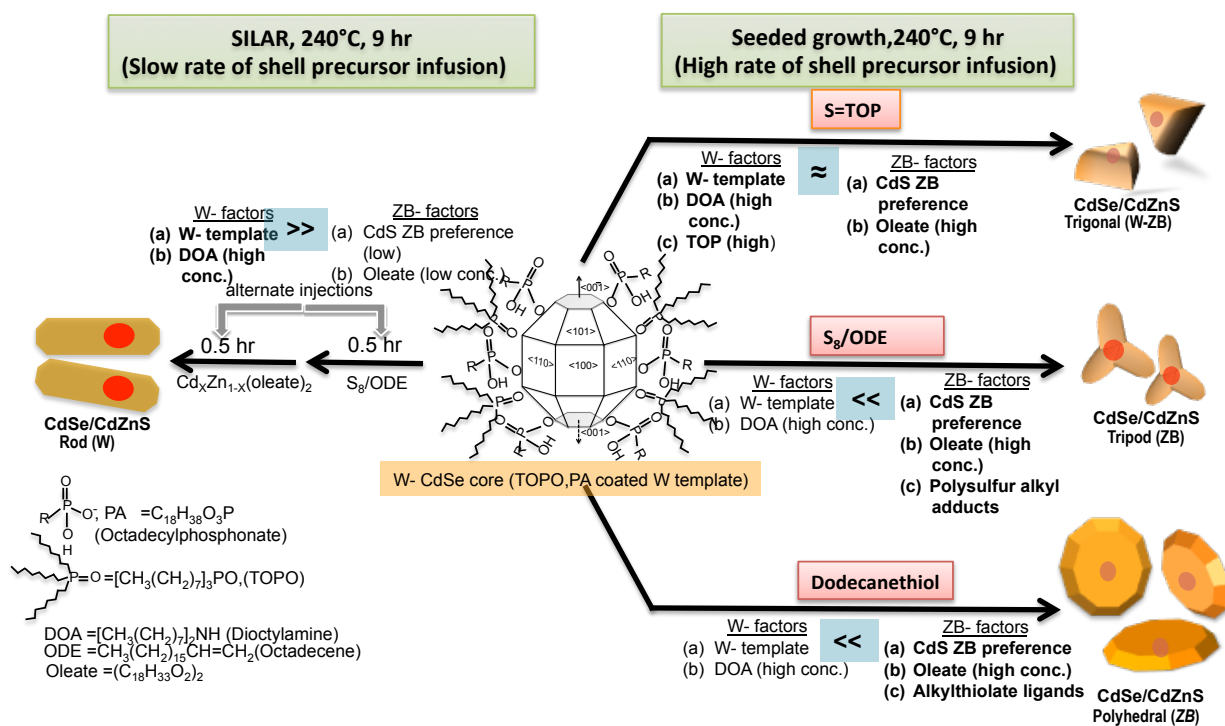
**Figure 3.17:** shows the XRD pattern for CdSe/CdZnSe gQDs starting from the core (i), at  $T_1$  (ii),  $T_2$  (iii) and  $T_3$  (iv). The CdSe  $W$  standards are shown as reference.

Fig. 3.17 shows the XRD pattern for control experiment performed using Se=TOP as the shell precursor to form CdSe/CdZnSe gQDs. As seen from Fig. 3.17, gQD growth was observed to proceed in a purely wurtzite manner from  $T_1$  (ii) till the completion of the reaction, ( $T_3$ , iv). The Se=TOP and S=TOP seeded synthesis being exactly identical in terms of synthetic procedure and molar concentration ratios, only differed in terms of the anionic shell precursor employed. The experimental evidence clearly depicts that in case of CdSe/CdZnSe gQDs, the crystal structure preference of CdSe ( $W$ )<sup>45</sup> results in pure  $W$ -type growth as compared to polytypic growth observed in case CdSe/CdZnS gQDs, in which the crystal structure preference of CdS and ZnS (both preferring ZB structure)<sup>55–57</sup> plays a critical part.

### 3.6 Discussion

Experimental observations indicate disparate crystal growth pattern of the gQDs in case of SILAR synthesis ( $W$ , anisotropic growth) compared to seeded syntheses ( $ZB$  or  $W$ - $ZB$

symmetric, isotropic growth). A closer inspection of the underlying crystal structure morphology of hexagonal *W*-CdSe provides insight into the growth mechanism. A hexagonal *W*-CdSe crystal possesses an inherent tendency to promote anisotropic growth in presence of ionic shell precursor monomers along the  $\langle 002 \rangle$  direction, owing to a difference in polarity amongst the polar basal planes ( $\langle 001 \rangle$ ,  $\langle 00\bar{1} \rangle$ ) and the apolar lateral  $\langle 100 \rangle$ ,  $\langle 110 \rangle$  facets.<sup>25,26,58</sup> The differential reactivity of crystal facets is further reinforced by the facet selective coordination of octadecylphosphonate and trioctylphosphine oxide ligands residing on crystal interface of the synthesized *W* CdSe cores.<sup>16,26,59–62</sup> Thus the presence of phosphonate ligands on CdSe surface and the high concentration of dioctylamine (which has been reported to promote a wurtzite growth<sup>36</sup>) in the reaction medium during SILAR synthesis, creates a template for anisotropic *W* growth along the  $\langle 002 \rangle$ . Sequential injection of small amounts of shell precursors in SILAR addition thus results in monomer addition to occur along  $\langle 002 \rangle$ , leading to the formation of rods.



**Figure 3.18:** Schematic outline summarizing the disparate growth morphology of gQDs starting from *W* – CdSe core, under diverse synthetic conditions.

In spite of presence of anisotropic *W* growth template (as discussed above) the seeded growth process result in symmetric (*ZB*, *W-ZB*) growth of gQDs, suggesting that some other contributing factors compete to dictate the crystallographic evolution. Shape evolution in a quantum dot essentially depends on both kinetic and thermodynamic parameters. In the case of seeded growth processes, the single injection of shell precursors in the reaction medium results in rapid kinetic growth initially, followed by a prolonged annealing (9hr) time period in absence of monomers (thermodynamic regime). I believe the crystal structure preference of the interim CdS wetting layer and ZnS (in later stages) during shell growth plays a pivotal part in determining the crystal growth pattern. Synthesis of CdS and ZnS nanoparticles at high monomer concentrations and high temperatures (kinetic regime) has been reported to prefer the *ZB* cubic phase over the hexagonal *W*.<sup>55–57</sup> The kinetic growth regime in the seeded growth is expected to

prefer the zinc blende phase (ABCABC stacking) over the wurtzite phase (ABAB stacking). Control experiments (See supporting information) performed on CdSe cores employing Se=TOP as the anionic precursor for CdZnSe shell growth, showed formation of pure *W* gQDs, with no polytypic character. The evidence from the experiment indicates, though the ligand concentration and type were kept identical in both cases (viz. S=TOP, Se=TOP) the pattern of shell growth (*W-ZB* polytypic and *W* respectively) were different due to the disparity in the innate crystal structure preference of CdS (*ZB*) and CdSe (*W*) during kinetic growth. Secondly, in the case of seeded process, the depletion of the shell precursor monomers during the prolonged annealing leads to symmetric growth of gQDs as dictated by a thermodynamic regime.<sup>22</sup> Further, *ZB* CdS and ZnS have been shown to have a higher thermodynamic stability than their wurtzite counterparts, unlike CdSe in which the wurtzite structure is favored.<sup>45,63–65</sup> Thus growth of symmetric *ZB* phase is expected to be favored over *W* phase, suggesting the kinetic and thermodynamic parameters supplement each other. Thirdly, taking into consideration the ligand effects: in the case of seeded processes, substantial concentrations of both the *ZB* favoring oleate and *W* favoring dioctylamine compete for coordinating to the gQD surface from the initial stages. Oleate ligand being less bulky than dioctylamine, preferentially coordinates to the gQD surface (in spite of the higher concentration of the latter) and contributes significantly to crystal structure evolution resulting in polytypic nanocrystals.<sup>36</sup> Further, synthesis of S=TOP gQDs involved the injection of TOP ligand, into the reaction medium, which is known to favor *W* phase<sup>66,67</sup> thus effecting the formation of polytypic gQDs. The crystal structure influence of TOP becomes apparent, in the case of S<sub>8</sub>/ODE gQDs, which possessed pure *ZB* structure in the absence of TOP

under identical reaction conditions. In the case of DDT gQDs, dodecanethiol preferentially co-ordinates to the gQDs surface due to lesser steric bulk (than TOP) and higher affinity of thiolate ion (deprotonated by high DOA concentration) for surface  $\text{Cd}^{+2}$  atoms.<sup>68</sup> In addition, recent investigations on synthesis of PbS quantum dots have shown that the polysulfur alkyl adducts generated in  $\text{S}_8/\text{ODE}$  sulfur precursor bind to the quantum dot facets in a manner similar to alkylthiols.<sup>69</sup> I believe, in our system, analogous organosulfur species present in  $\text{S}_8/\text{ODE}$  influence the crystal structure growth pattern. Alkyl thiols, employed as anionic precursors (S precursors) in synthetic procedures has been observed to promote *ZB* growth.<sup>70,71</sup> Thus in case of  $\text{S}_8/\text{ODE}$  and DDT gQDs, following the initial nucleation of  $\langle 111 \rangle$  facet of *ZB* preferring CdZnS shell on the  $\langle 002 \rangle$  facets of *W* core, organosulfur adducts selectively coordinate to the  $\langle 111 \rangle$  planes<sup>69</sup> and further propagate the *ZB* growth.

### 3.7 Conclusion

In conclusion, the work investigates the growth of gQDs involving the SILAR and seeded growth procedures. Disparate morphology and crystallography of gQDs resulted from each syntheses and the plausible growth mechanism involved therein has been described in detail. HRTEM and electron diffraction studies showed the novel formation of *W*- rods by the SILAR process, while  $\text{S}_8/\text{ODE}$ ,  $\text{S}=\text{TOP}$  and DDT mediated seeded synthesis yielded *ZB* tripodal, mixed *ZB-W* trigonal and *ZB* polyhedral morphologies for gQDs. Thus mode of addition and source of ‘S’ shell precursors coupled with the delicate interplay between competing ligands during growth was seen to have a pronounced effect on the crystal structure and photophysical properties of the formed gQDs. In summary, the work shows the novel rational control over the growth morphology and crystal pattern



of the gQDs is achievable without the introduction of strongly shape directing ligands like phosphonic acids, oleylamine etc. The knowledge is believed to aid in tailoring the gQDs for solid state processing in future applications.

### 3.8 References

- (1) Alam, R.; Fontaine, D. M.; Branchini, B. R.; Maye, M. M. *Nano Lett.* **2012**, *12* (6), 3251–3256.
- (2) Alam, R.; Zylstra, J.; Fontaine, D. M.; Branchini, B. R.; Maye, M. M. *Nanoscale* **2013**, *5* (12), 5303–5306.
- (3) Alam, R.; Karam, L. M.; Doane, T. L.; Zylstra, J.; Fontaine, D. M.; Branchini, B. R.; Maye, M. M. *Nanotechnology* **2014**, *25* (49), 495606.
- (4) Klimov, V. I.; Ivanov, S. A.; Nanda, J.; Achermann, M.; Bezel, I.; McGuire, J. A.; Piryatinski, A. *Nature* **2007**, *447* (7143), 441–446.
- (5) García-Santamaría, F.; Chen, Y.; Vela, J.; Schaller, R. D.; Hollingsworth, J. A.; Klimov, V. I. *Nano Lett.* **2009**, *9* (10), 3482–3488.
- (6) Zavelani-Rossi, M.; Lupo, M. G.; Krahne, R.; Manna, L.; Lanzani, G. *Nanoscale* **2010**, *2* (6), 931–935.
- (7) Kazes, M.; Lewis, D. y.; Ebenstein, Y.; Mokari, T.; Banin, U. *Adv. Mater.* **2002**, *14* (4), 317–321.
- (8) Anikeeva, P. O.; Halpert, J. E.; Bawendi, M. G.; Bulović, V. *Nano Lett.* **2009**, *9* (7), 2532–2536.
- (9) Zhao, J.; Bardecker, J. A.; Munro, A. M.; Liu, M. S.; Niu, Y.; Ding, I.-K.; Luo, J.; Chen, B.; Jen, A. K.-Y.; Ginger, D. S. *Nano Lett.* **2006**, *6* (3), 463–467.
- (10) Alivisatos, P. *Nat. Biotechnol.* **2004**, *22* (1), 47–52.

- (11) Medintz, I. L.; Uyeda, H. T.; Goldman, E. R.; Mattoussi, H. *Nat. Mater.* **2005**, *4* (6), 435–446.
- (12) Hahn, M. A.; Tabb, J. S.; Krauss, T. D. *Anal. Chem.* **2005**, *77* (15), 4861–4869.
- (13) Ruan, G.; Agrawal, A.; Marcus, A. I.; Nie, S. *J. Am. Chem. Soc.* **2007**, *129* (47), 14759–14766.
- (14) Rice, K. P.; Saunders, A. E.; Stoykovich, M. P. *J. Am. Chem. Soc.* **2013**, *135* (17), 6669–6676.
- (15) Talapin, D. V.; Nelson, J. H.; Shevchenko, E. V.; Aloni, S.; Sadtler, B.; Alivisatos, A. P. *Nano Lett.* **2007**, *7* (10), 2951–2959.
- (16) Milliron, D. J.; Hughes, S. M.; Cui, Y.; Manna, L.; Li, J.; Wang, L.-W.; Paul Alivisatos, A. *Nature* **2004**, *430* (6996), 190–195.
- (17) Manna, L.; Scher, E. C.; Alivisatos, A. P. *J. Am. Chem. Soc.* **2000**, *122* (51), 12700–12706.
- (18) Liu, L.; Zhuang, Z.; Xie, T.; Wang, Y.-G.; Li, J.; Peng, Q.; Li, Y. *J. Am. Chem. Soc.* **2009**, *131* (45), 16423–16429.
- (19) Ithurria, S.; Dubertret, B. *J. Am. Chem. Soc.* **2008**, *130* (49), 16504–16505.
- (20) Deka, S.; Miszta, K.; Dorfs, D.; Genovese, A.; Bertoni, G.; Manna, L. *Nano Lett.* **2010**, *10* (9), 3770–3776.
- (21) Miszta, K.; de Graaf, J.; Bertoni, G.; Dorfs, D.; Brescia, R.; Marras, S.; Ceseracciu, L.; Cingolani, R.; van Roij, R.; Dijkstra, M.; Manna, L. *Nat. Mater.* **2011**, *10* (11), 872–876.
- (22) Nair, P. S.; Fritz, K. P.; Scholes, G. D. *Small* **2007**, *3* (3), 481–487.
- (23) Chauhan, H.; Kumar, Y.; Deka, S. *Nanoscale* **2014**, *6* (17), 10347–10354.

- (24) Yong, K.-T.; Sahoo, Y.; Swihart, M. T.; Prasad, P. N. *J. Phys. Chem. C* **2007**, *111* (6), 2447–2458.
- (25) Peng, X.; Manna, L.; Yang, W.; Wickham, J.; Scher, E.; Kadavanich, A.; Alivisatos, A. P. *Nature* **2000**, *404* (6773), 59–61.
- (26) Manna, L.; Scher, E. C.; Alivisatos, A. P. *J. Clust. Sci.* **2002**, *13* (4), 521–532.
- (27) Chen, Y.; Vela, J.; Htoon, H.; Casson, J. L.; Werder, D. J.; Bussian, D. A.; Klimov, V. I.; Hollingsworth, J. A. *J. Am. Chem. Soc.* **2008**, *130* (15), 5026–5027.
- (28) Ghosh, Y.; Mangum, B. D.; Casson, J. L.; Williams, D. J.; Htoon, H.; Hollingsworth, J. A. *J. Am. Chem. Soc.* **2012**, *134* (23), 9634–9643.
- (29) Vela, J.; Htoon, H.; Chen, Y.; Park, Y.-S.; Ghosh, Y.; Goodwin, P. M.; Werner, J. H.; Wells, N. P.; Casson, J. L.; Hollingsworth, J. A. *J. Biophotonics* **2010**, *3* (10-11), 706–717.
- (30) Pal, B. N.; Ghosh, Y.; Brovelli, S.; Laocharoensuk, R.; Klimov, V. I.; Hollingsworth, J. A.; Htoon, H. *Nano Lett.* **2012**, *12* (1), 331–336.
- (31) Htoon, H.; Malko, A. V.; Bussian, D.; Vela, J.; Chen, Y.; Hollingsworth, J. A.; Klimov, V. I. *Nano Lett.* **2010**, *10* (7), 2401–2407.
- (32) Galland, C.; Ghosh, Y.; Steinbrück, A.; Hollingsworth, J. A.; Htoon, H.; Klimov, V. I. *Nat. Commun.* **2012**, *3*, 908.
- (33) Galland, C.; Ghosh, Y.; Steinbrück, A.; Sykora, M.; Hollingsworth, J. A.; Klimov, V. I.; Htoon, H. *Nature* **2011**, *479* (7372), 203–207.
- (34) Kundu, J.; Ghosh, Y.; Dennis, A. M.; Htoon, H.; Hollingsworth, J. A. *Nano Lett.* **2012**, *12* (6), 3031–3037.

- (35) Karan, N. S.; Keller, A. M.; Sampat, S.; Roslyak, O.; Arefin, A.; Hanson, C. J.; Casson, J. L.; Desiredy, A.; Ghosh, Y.; Piryatinski, A.; Iyer, R.; Htoon, H.; Malko, A. V.; Hollingsworth, J. A. *Chem. Sci.* **2015**, 6 (4), 2224–2236.
- (36) Majumder, S.; Bae, I.-T.; Maye, M. M. *J. Mater. Chem. C* **2014**, 2 (23), 4659–4666.
- (37) Carbone, L.; Nobile, C.; De Giorgi, M.; Sala, F. D.; Morello, G.; Pompa, P.; Hytch, M.; Snoeck, E.; Fiore, A.; Franchini, I. R.; Nadasan, M.; Silvestre, A. F.; Chiodo, L.; Kudera, S.; Cingolani, R.; Krahne, R.; Manna, L. *Nano Lett.* **2007**, 7 (10), 2942–2950.
- (38) Li, J. J.; Wang, Y. A.; Guo, W.; Keay, J. C.; Mishima, T. D.; Johnson, M. B.; Peng, X. *J. Am. Chem. Soc.* **2003**, 125 (41), 12567–12575.
- (39) Zylstra, J.; Amey, J.; Miska, N. J.; Pang, L.; Hine, C. R.; Langer, J.; Doyle, R. P.; Maye, M. M. *Langmuir* **2011**, 27 (8), 4371–4379.
- (40) Yu, W. W.; Qu, L.; Guo, W.; Peng, X. *Chem. Mater.* **2003**, 15 (14), 2854–2860.
- (41) Jasieniak, J.; Smith, L.; Embden, J. van; Mulvaney, P.; Califano, M. *J. Phys. Chem. C* **2009**, 113 (45), 19468–19474.
- (42) Patterson, A. L. *Phys. Rev.* **1939**, 56 (10), 978–982.
- (43) Llordés, A.; Palau, A.; Gázquez, J.; Coll, M.; Vlad, R.; Pomar, A.; Arbiol, J.; Guzmán, R.; Ye, S.; Rouco, V.; Sandiumenge, F.; Ricart, S.; Puig, T.; Varela, M.; Chateigner, D.; Vanacken, J.; Gutiérrez, J.; Moshchalkov, V.; Deutscher, G.; Magen, C.; Obradors, X. *Nat. Mater.* **2012**, 11 (4), 329–336.
- (44) Williamson, G. K.; Hall, W. H. *Acta Metall.* **1953**, 1 (1), 22–31.
- (45) Guo, Y.; Marchuk, K.; Sampat, S.; Abraham, R.; Fang, N.; Malko, A. V.; Vela, J. *J. Phys. Chem. C* **2012**, 116 (4), 2791–2800.

- (46) Chen, O.; Zhao, J.; Chauhan, V. P.; Cui, J.; Wong, C.; Harris, D. K.; Wei, H.; Han, H.-S.; Fukumura, D.; Jain, R. K.; Bawendi, M. G. *Nat. Mater.* **2013**, *12* (5), 445–451.
- (47) Park, Y.-S.; Bae, W. K.; Padilha, L. A.; Pietryga, J. M.; Klimov, V. I. *Nano Lett.* **2014**, *14* (2), 396–402.
- (48) Manna, L.; Scher, E. C.; Li, L.-S.; Alivisatos, A. P. *J. Am. Chem. Soc.* **2002**, *124* (24), 7136–7145.
- (49) Scardi, P.; Leoni, M.; Delhez, R. *J. Appl. Crystallogr.* **2004**, *37* (3), 381–390.
- (50) Mote, V. D.; Purushotham, Y.; Dole, B. N. *J. Theor. Appl. Phys.* **2012**, *6* (1), 1–8.
- (51) Cullity, B. D. *Elements of X-ray diffraction*, 1. print.; Addison-Wesley series in metallurgy and materials; Addison-Wesley: Reading, Mass, 1956; pp 263-264.
- (52) Talapin, D. V.; Mekis, I.; Götzinger, S.; Kornowski, A.; Benson, O.; Weller, H. *J. Phys. Chem. B* **2004**, *108* (49), 18826–18831.
- (53) Buhro, W. E.; Colvin, V. L. *Nat. Mater.* **2003**, *2* (3), 138–139.
- (54) Kim, J.; Nair, P. S.; Wong, C. Y.; Scholes, G. D. *Nano Lett.* **2007**, *7* (12), 3884–3890.
- (55) Christian, P.; O'Brien, P. *Chem. Commun.* **2005**, No. 22, 2817–2819.
- (56) Christian, P.; O'Brien, P. *J. Mater. Chem.* **2008**, *18* (14), 1689–1693.
- (57) Zhang, H.; Chen, B.; Gilbert, B.; Banfield, J. F. *J. Mater. Chem.* **2006**, *16* (3), 249–254.
- (58) Rosenthal, S. J.; McBride, J.; Pennycook, S. J.; Feldman, L. C. *Surf. Sci. Rep.* **2007**, *62* (4), 111–157.
- (59) Peng, Z. A.; Peng, X. *J. Am. Chem. Soc.* **2002**, *124* (13), 3343–3353.

- (60) Manna, L.; Wang; Cingolani, R.; Alivisatos, A. P. *J. Phys. Chem. B* **2005**, *109* (13), 6183–6192.
- (61) Puzder, A.; Williamson, A. J.; Zaitseva, N.; Galli, G.; Manna, L.; Alivisatos, A. P. *Nano Lett.* **2004**, *4* (12), 2361–2365.
- (62) Manna, L.; Milliron, D. J.; Meisel, A.; Scher, E. C.; Alivisatos, A. P. *Nat. Mater.* **2003**, *2* (6), 382–385.
- (63) Scott, S. D.; Barnes, H. L. *Geochim. Cosmochim. Acta* **1972**, *36* (11), 1275–1295.
- (64) Yeh, C.-Y.; Lu, Z. W.; Froyen, S.; Zunger, A. *Phys. Rev. B* **1992**, *46* (16), 10086–10097.
- (65) Lin, Q.; Makarov, N. S.; Koh, W.; Velizhanin, K. A.; Cirloganu, C. M.; Luo, H.; Klimov, V. I.; Pietryga, J. M. *ACS Nano* **2015**, *9* (1), 539–547.
- (66) Sapra, S.; Rogach, A. L.; Feldmann, J. *J. Mater. Chem.* **2006**, *16* (33), 3391–3395.
- (67) Al-Salim, N.; Young, A. G.; Tilley, R. D.; McQuillan, A. J.; Xia, J. *Chem. Mater.* **2007**, *19* (21), 5185–5193.
- (68) Schapotschnikow, P.; Hommersom, B.; Vlugt, T. J. H. *J. Phys. Chem. C* **2009**, *113* (29), 12690–12698.
- (69) McPhail, M. R.; Weiss, E. A. *Chem. Mater.* **2014**, *26* (11), 3377–3384.
- (70) Jun, S.; Jang, E.; Chung, Y. *Nanotechnology* **2006**, *17* (19), 4806–4810.
- (71) Bose, R.; Manna, G.; Pradhan, N. *J. Phys. Chem. C* **2013**, *117* (36), 18762–18767.

## Chapter 4

### Conclusions and outlook

In this dissertation, I described work involving the synthesis of giant quantum dots (gQDs), and investigate how does the variation in the different synthetic parameters alter the crystallography, morphology and photophysical properties.

First, in order to investigate the role that the core crystallinity plays in determining the crystal structure and morphology of the gQDs, I performed alloy ( $\text{Cd}_x\text{Zn}_{1-x}\text{S}$ ) shell deposition on CdSe cores having *W* and *ZB* crystal structure (Chapter 2). The cores were synthesized using the ‘hot injection’ technique and for shell growth layer-by-layer SILAR was used. Further, for the deposition of the alloy shell in both syntheses I used three feed ratios for cationic shell precursors, in order to minimize the lattice strain at the core shell interface to improve epitaxial growth of the shell on the core. I demonstrated that the shell growth in gQDs synthesized from both type of cores transition to *W* type under the synthetic conditions employed. In addition to that, I observed the unique occurrence of polytypism in the alloy shell of the gQDs in both cases, an aspect that has been scarcely reported in scientific literature on gQDs. X-ray diffraction (XRD) and High-resolution transmission electron microscopic (HRTEM) analysis of the gQDs provided strong scientific evidence showing the co existence of *W*-*ZB* domains in the same nanocrystal. This polytypic nature of the gQDs resulted in polycrystalline domains, twinning and stacking defects, localized *W*-*ZB*-*W* layering and crystalline protrusions at the gQD interface, leading to a defect rich shell. This in turn was observed to have far reaching effects on the morphology and photophysical

properties of the gQDs. I discussed the probable factors which have induced the polytypic nature of the shell in detail, amongst which the disparate crystal structure preference of the mixed (dioctylamine-oleate) ligand shell, alloy gradient of the shell deposited and the proximity of shell growth temperature to *W-ZB* transition temperature were believed to be the most significant ones.

Next, I investigated the influence of anion shell precursor concentrations on the shell growth, (Chapter 3) by altering the mode of addition and three different sources of sulfur. For the study I carried out growth on identical *W*- cores, involving both SILAR and ‘seeded’ growth. Further, for the seeded growth process, I have employed three sources of sulfur precursors;  $S_8$  in ODE ( $S_8$ /ODE),  $S_8$  in TOP ( $S$ =TOP) and dodecanethiol (DDT). My investigations revealed that available concentrations of shell precursors radically alter the shell growth in gQDs. Using  $S_8$ /ODE as the sulfur precursor, unique anisotropic rod shaped gQDs with *W* crystallinity resulted from SILAR addition (low precursor concentration); while tripodal gQDs with *ZB* crystallinity resulted from seeded growth (high precursor concentration) on identical *W*- cores. Further,  $S$ =TOP and DDT gQDs were observed to have trigonal (*W-ZB*, polytypic) and polyhedral (*ZB*) morphologies. The seeded growth gQDs showed considerable QYs. A detailed discussion on the factors that led to such disparate morphologies and crystal structures of gQDs was provided. Experimental evidence suggested that the delicate equilibrium between inherent crystal structure preference of the CdZnS shell and the ligands involved plays an important role in morphology and crystallinity.

In conclusion systematic insight into the crystallographic and morphological evolution of gQDs is provided. The scientific knowledge gained from my research will



aid in the synthesis of high quality defect free gQDs in the future. Further, controlled polytypism by twinning engineering for generation of polymorphic nanocrystals will benefit from the ligand studies investigated in this work. Band gap engineering and charge separation studies by directing the extent of polycrystallinity in a single nanocrystal is expected to be an interesting area of research for use in optical and photovoltaic devices. Finally, the dissertation shows that novel rational control over the growth morphology, and crystal growth is achievable by minor alterations in the synthetic procedure of gQD synthesis. Knowledge of such unique shape, crystallographic and photophysical behavior control can be exploited for tailoring the gQDs to suit the requirements for solid state processing in future applications.

# CURRICULUM VITAE

## SOMAK MAJUMDER

---

Department of Chemistry, Syracuse University,  
1-014 Centre for Science and Technology, Syracuse, NY-13244  
Email: [smajumde@syr.edu](mailto:smajumde@syr.edu), Ph.: (480)-335-9643

## EDUCATION

---

**Doctor of Philosophy in Chemistry**, (2010 – expected June 2015)

Syracuse University, Chemistry Department,  
Syracuse, NY

Advisor: Dr. Mathew M. Maye, Department of Chemistry, [Syracuse University](http://www.syr.edu)

Thesis title: “Investigating the unique occurrence of polytypism and the role of available shell precursors in the growth of giant shell quantum dots”

**Master of Science in Wood Science and Technology**, (2007-2009)

Forest Research Institute University (FRI),  
Dehradun, India

Thesis Advisors: Dr. Arunava Goswami, Associate Professor, [ISI, Kolkata, India](http://www.isi.ac.in) / Dr. D.P. Khali, Scientist E, [FRI, Dehradun, India](http://www.fri.ac.in).

M.Sc. dissertation title: “Synthesis, Characterization of Silver nanoparticles and their application in the Forest Products Division”

**Bachelor of Science in Chemistry**, (2003 – 2007)

Chemistry Department, Presidency College, University of Calcutta,  
Kolkata, India

## PUBLICATIONS

---

- **S. Majumder**, I. Bae, M. M. Maye, ‘Investigating the role of polytypism in the growth of multishell CdSe/CdZnS quantum dots’, *Journal of Materials Chemistry C*, **2014**, 2, 4659-4666
- **S. Majumder**, I. Bae, M. M. Maye, ‘Rational control of crystal structure and morphology in the growth of CdSe/CdZnS giant quantum dots by alteration of monomer concentration and source of shell precursors’, **2015**, (Manuscript In Preparation)

## PRESENTATIONS

---

- Presentation titled, ‘Observing polytypism in multishell CdSe/Cd<sub>x</sub>Zn<sub>1-x</sub>S giant quantum dots’ at oral sessions, [ACS CERM Regional Meeting](http://www.acs.org), Pittsburgh, PA (Oct 31, 2014)
- Presented poster titled, ‘Investigating the role of polytypism in the growth of multishell CdSe/CdZnS quantum dots’ at [246<sup>th</sup> ACS National Meeting and Exposition](http://www.acs.org), Indianapolis, Indiana, September 10, 2013
- Successfully defended M.Sc. dissertation performed at Indian Statistical Institute (ISI), Kolkata in front of panelists comprised of eminent scientists from Forest Research Institute University, India (July, 2009)

## TECHNICAL SKILLS

---

- Instrumentation experience (Operation and Data processing): Ultraviolet-Visible Spectroscopy (UV-Vis), Photoluminescence Spectroscopy (PL), Infrared Spectroscopy (FTIR), Transmission Electron Microscopy

(TEM), Thermogravimetric Analysis (TGA), Powder X-Ray diffraction (XRD), High Resolution Transmission Electron Microscopy (HRTEM), Electron Diffraction Analysis (ED). Familiarity with AFM.

- Software: Data Graph, Corel Draw (Graphics Suite X3-X7), Image J, Igor Pro, Adobe Photoshop, Adobe Illustrator, MS Office Suite, Chem Draw, Bruker D8 tools, Bruker XRD commander,

## RESEARCH EXPERIENCE

---

As a PhD candidate at the [Maye Research group](#), I possess a high degree of expertise in synthesis of inorganic semiconductive nanocrystalline materials under moisture and air-free reaction conditions. I am adept at the handling of potentially dangerous, pyrophoric chemicals and radiation safety required equipment. I have gained considerable experience in different synthetic protocols for colloidal nanocrystals (such as SILAR, hot injection and seeded growth techniques) along with an in depth knowledge about the reactivities of different precursor materials, facet selectivity of ligands and implementing them into novel synthetic protocols. I am especially well versed in the characterization of quantum dots by photophysical (UV-vis, PL), diffraction (XRD, ED) and electron microscopic (TEM, HRTEM) techniques. During the course of my graduate study, I have had the opportunity to work and interact with researchers in multidisciplinary facilities in my department as well as external collaborations (SUNY-ESF, SUNY-Binghamton, Brookhaven National Labs).

### Accomplishments

- I led the research experiments of our group in the synthesis and characterization of multishell CdSe/CdZnS giant core/shell quantum dots by the layer-by-layer shell addition approach
- Performed and published an in depth analysis of the crystallographic evolution of the shell growth process in multishelled CdSe/CdZnS quantum dots and the role of ligands in affecting the nature of shell growth (Published 2014)
- Observed and studied the unique polytypic nature of epitaxially grown shells in gQDs, correlating the role of surface defects on the photophysical properties of the gQDs (Published 2014).
- Devised a novel single step shell addition synthetic technique for the synthesis of multishelled CdSe/CdZnS quantum dots with varied photophysical, crystallographic and morphological characteristics (Manuscript in preparation)
- Performed M.Sc. dissertation work aimed at the synthesis of silver nanoparticles using biologically friendly capping agents like BSA, PVP, palmitic acid etc. with a view to reduce the biological toxicity. In addition to that, core-shell Ag@SiO<sub>2</sub> was synthesized by a novel technique in which, the biotoxic effects of silver is greatly reduced by the silica shell shielding the inner silver core thereby enabling the use of the antimicrobial nano Ag in the biological samples. FTIR, UV, TEM, SEM, DLS techniques had been used for characterization of silver nanoparticles.

## AWARDS AND HONORS

---

- **University Graduate Fellowship:** Awarded University Fellowship from 2010 - 2014.
- **Chemistry Summer Fellowship award:** Merit based award from the Chemistry Department, Syracuse University (June 2014, June 2012)
- **Research Assistantship:** Supported as fellow on AFOSR, NSF and ACS supported grants (Summer 2011, Summer 2012, Summer 2013 and Summer 2014)
- Invited by ACS to upload the poster entitled, 'Investigating the role of polytypism in the growth of multishell CdSe/CdZnS quantum dots' as part of **Presentations on Demand** online collection of few selected works from 246<sup>th</sup> ACS National Meeting and Exposition, Indianapolis, IN (October 2013)
- Certificate of honor from Indian Statistical Institute (ISI), Kolkata, India for Summer Research Training, (2009)

- Qualified national level entrance exam conducted by Forest Research Institute, Dehradun, India for M.Sc., (all India rank 15<sup>th</sup> among ~2000 students appearing), (2007)
- Qualified national level entrance exam conducted by University of Delhi, India for M. Sc. in Chemistry (all India rank 3<sup>rd</sup> among ~1500 students appearing)(2007)
- Awarded National Scholarship Certificate of Merit, India for outstanding result in Madhyamik examination (10<sup>th</sup> grade State Board exam), (2001)

## **TEACHING AND MENTORING EXPERIENCE**

---

I have mentored junior lab members, in particular areas of their research projects, demonstrating the synthesis, characterization techniques for semiconductive nanoparticles and interpretation of the analytical data.

Undergraduate teaching assistant experience at Syracuse University:

- Designed and performed experiments now part of CHE117 General Chemistry II Lab curriculum for Spring 2015 (Fall 2014)
- Recitation TA for General Chemistry I CHE 116 (Spring 2015)
- Lab TA for General Chemistry Lab course I CHE 107 (Fall 2014)
- Lab TA for Forensic Sciences Lab course CHE 113 (Spring 2014)
- Lab TA for General Chemistry for Engineers Lab course CHE 151 (Fall 2013)
- Lab TA for General Chemistry II Lab course CHE 117 (Spring 2012)
- Recitation TA for General Chemistry I CHE 106 (Fall, 2011)